

AN ABSTRACT OF THE THESIS OF

Jin Koo Rhee for the degree of Doctor of Philosophy in Electrical and Computer Engineering presented on April 12, 1982.

Title: Electrical and Optical Properties of Semi-Insulating and Ion-Implanted GaAs and InP

Abstract approved:

Redacted for privacy

Dr. P.K. Bhattacharya

Redacted for privacy

Dr. S.J.T. Owen

The electrical and optical properties of semi-insulating, epitaxial and ion-implanted GaAs and InP have been characterized and analyzed. Electron and hole traps in semi-insulating GaAs and InP, with activation energies  $\Delta E_T$  ranging from  $0.16 \pm 0.01$  to  $0.98 \pm 0.01$  eV, have been detected and characterized by Photo-Induced Current Transient measurements. The thermal capture cross section and density of the traps have been estimated and some of the centers have been related to native defects. In particular, the activation energy of the compensating Cr, Fe and "O" levels in semi-insulating GaAs and InP were accurately measured. The transient measurements were complemented by Hall measurements at  $T > 300K$  and photocurrent spectra measurements. The transition energies for the deep compensating levels obtained by the analyses of data from these measurements, when compared with those from the transient measurements, indicate negligible lattice-coupling of these centers. Analysis of the transport data also indicates that neutral impurity scattering plays a significant role in semi-insulating materials at high temperatures.

Semi-insulating GaAs and InP, vapor phase epitaxial GaAs, and liquid phase epitaxial InP were implanted with  $^{28}\text{Si}^+$  to evaluate the changes in transport properties and deep-level spectra. The dominant 0.83 eV electron trap in VPE GaAs and 0.38 eV electron trap and 0.22 eV hole trap in LPE InP were removed and new traps were created. Electron traps with  $\Delta E_{\text{T}} = 0.52 \pm 0.01$  eV and hole traps with  $\Delta E_{\text{T}} = 0.15 \pm 0.01$  eV were consistently detected in implanted and annealed GaAs, irrespective of the type of starting material. These centers are characteristic of the implant and anneal processing in GaAs. Similarly, an electron trap with  $\Delta E_{\text{T}} = 0.17 \pm 0.01$  eV was consistently detected in implanted LPE InP. A significant reduction in electron mobility for  $T < 300\text{K}$  was observed in epitaxial GaAs and InP after implant and anneal. The mobility data were analyzed in detail and it is apparent that the reduction in mobility is due to increased impurity scattering and not due to implant damage.

© Copyright by Jin Koo Rhee

April 12, 1982

All Rights Reserved

Electrical and Optical Properties of Semi-Insulating and  
Ion-Implanted GaAs and InP

by

Jin Koo Rhee

A THESIS

submitted to

Oregon State University

in partial fulfillment of  
the requirements for the  
degree of

Doctor of Philosophy

Completed April 12, 1982

Commencement June 1982

APPROVED:

Redacted for privacy

Assistant Professor of Electrical & Computer Engineering in  
charge of major

Redacted for privacy

Head of Department of Electrical & Computer Engineering

Redacted for privacy

Dean of Graduate School

Date thesis is presented April 12, 1982

Typed by Laurie Campbell for Jin Koo Rhee

## ACKNOWLEDGEMENTS

I wish to express my deep gratitude to my advisors, Professors P.K. Bhattacharya and S.J.T. Owen, for their guidance and encouragement during the course of this work. I would like to express my sincere appreciation to Dr. R.Y. Koyama of Tektronix Laboratories for his interest in the work and for doing all the implantation and annealing needed for this study. Partial support by the National Science Foundation under Grant No. ECS-8011917 is gratefully acknowledged.

Finally, I would like to thank my wife, Myung Ock, for her patience and support, and my mother for her encouragement.

## TABLE OF CONTENTS

I.	INTRODUCTION	1
II.	THEORETICAL CONSIDERATIONS	7
	2.1 Defects and Deep Levels in a Semiconductor	7
	2.2 Theory of Capacitance Transient and Photo-Induced Current Transient Measurements	8
	2.3 Theory of Transport Measurements	15
	2.4 Theory of Photoconductivity and Photocurrent Spectra	22
III.	LIQUID PHASE EPITAXIAL GROWTH OF InP	24
	3.1 Growth System and Techniques	24
	3.2 Materials Preparation for Epitaxial Growth	26
	3.3 Growth Procedure	27
	3.4 Layer Characterization	29
	3.4.1 Layer Thickness	29
	3.4.2 Surface Morphology	30
	3.5 Discussion	35
IV.	PROPERTIES OF SEMI-INSULATING AND ION-IMPLANTED GaAs	37
	4.1 Device Fabrication	37
	4.1.1 Devices for Photo-Induced Current Transient Measurements	38
	4.1.2 Schottky Diodes on Epitaxial and Ion-Implanted Semiconductors	38
	4.1.3 GaAs Field Effect Transistors on Ion-Implanted Layers	39
	4.1.4 Devices for Hall Effect Measurements	39
	4.2 Photo-Induced Current Transient Measurements on Semi-Insulating GaAs	39
	4.3 Transient Capacitance Measurements on Ion-Implanted Semi-Insulating GaAs:Cr	42
	4.4 Transient Measurements on GaAs Field Effect Transistors	47
	4.5 Transient Capacitance Measurements on Vapor Phase Epitaxial GaAs	50
	4.6 Transient Capacitance Measurements on Ion-Implanted Vapor Phase Epitaxial GaAs	53
	4.7 Transport Measurements	53
	4.7.1 Semi-Insulating GaAs	53
	4.7.2 Ion-Implanted GaAs	61
	4.8 Analysis of Transport Data	68
	4.8.1 Semi-Insulating GaAs	68
	4.8.2 Ion-Implanted GaAs	69
	4.9 Photocurrent Spectra in Semi-Insulating GaAs	73
	4.10 Discussion	75

V. PROPERTIES OF SEMI-INSULATING AND ION-IMPLANTED InP	79
5.1 Fabrication of Devices	79
5.2 Photo-Induced Current Transient Measurements on Semi-Insulating InP	80
5.3 Transient Capacitance Measurements on Liquid Phase Epitaxial InP	83
5.4 Transient Capacitance Measurements on Ion- Implanted Liquid Phase Epitaxial InP	85
5.5 Ion-Implanted and Annealed Semi-Insulating InP.	90
5.6 Transport Measurements	92
5.6.1 Semi-Insulating InP	92
5.6.2 Ion-Implanted InP	92
5.7 Analysis of Transport Data	104
5.7.1 Semi-Insulating InP	104
5.7.2 Ion-Implanted InP	108
5.8 Photocurrent Spectra in Semi-Insulating InP	111
5.9 Photoconductivity Spectra in Ion-Implanted Semi-Insulating InP	115
5.10 Discussion	117
VI. CONCLUSIONS	120
REFERENCES	123
APPENDICES	
Appendix I	129
Appendix II	132
Appendix III	133

## LIST OF FIGURES

<u>Figure</u>		<u>Page</u>
2.1	Variation of experimentation parameters related to electron trap emission from the depletion region of a metal-n-semiconductor junction	10
2.2	Variation of experimentation parameters related to hole trap emission from the depletion region of a metal-n-semiconductor junction	12
2.3	Energy level models used to analyze transport data in semi-insulating semiconductors	18
3.1	Schematic of LPE growth system and graphite boat with slider	25
3.2	Time-temperature cycle for a typical epitaxial growth run	28
3.3	Photomicrographs of (a) the cleaved cross section of an LPE layer and (b) mirror-like surface morphology	31
3.4	Photomicrographs of surface morphologies depicting: (a) Indium inclusions, (b) poor wetting	32
3.5	Photomicrographs depicting remains of polycrystalline InP on the grown epitaxial layer	33
3.6	Photomicrographs of surface morphologies showing (a) ripples, (b) etch patterns created during <i>in situ</i> etching	34
4.1	(a) A typical GaAs FET structure and (b) typical $I_{DS} - V_{DS}$ characteristics	40
4.2	Schematic for Photo-Induced Current Transient measurements	41
4.3	Arrhenius plots for electron and hole trap levels in SI GaAs:Cr	43
4.4	Arrhenius plots for electron and hole trap levels for SI undoped GaAs	44
4.5	Pulse sequence and channel depletion-region behavior during direct trap measurements on GaAs FETs	49

<u>Figure</u>		<u>Page</u>
4.6	Arrhenius plots for electron and hole trap levels in as-grown VPE GaAs	52
4.7	Arrhenius plots for electron and hole trap levels in Si-implanted and annealed VPE GaAs	55
4.8	Variation of Hall electron mobility with temperature in (a) SI GaAs:Cr and (b) SI undoped GaAs	57
4.9	Plots of $R_H T^{3/2}$ versus inverse temperature in (a) SI GaAs:Cr and (b) SI undoped GaAs	58
4.10	Plots of $(qR_H)^{-1}$ versus inverse temperature in (a) SI GaAs:Cr and (b) SI undoped GaAs	59
4.11	Plots of dark conductivity, $\sigma$ , versus inverse temperature in (a) SI GaAs:Cr and (b) SI undoped GaAs	60
4.12	Variation of Hall electron mobility with temperature in as-grown and implanted VPE GaAs	64
4.13	Variation of electron mobility with temperature in as-grown samples E and CS107	65
4.14	Electron mobility variation with temperature in implanted and annealed sample 9	66
4.15	Temperature dependence of (a) Hall electron concentration in as-grown VPE GaAs and (b) activated surface carrier concentration in implanted and annealed VPE GaAs	67
4.16	Photocurrent spectra obtained at $T = 203$ and $100K$ for (a) SI GaAs:Cr and (b) SI undoped GaAs	74
5.1	Arrhenius plots for electron and hole trap levels in SI InP:Fe	81
5.2	Arrhenius plots for hole trap levels in SI InP:Cr	82
5.3	Arrhenius plots for electron and hole trap levels in as-grown LPE InP	86
5.4	Arrhenius plots for electron trap levels in Si-implanted and annealed LPE InP	88

<u>Figure</u>		<u>Page</u>
5.5	Photomicrographs depicting damages in (a) 2000 Å SiO <sub>2</sub> encapsulating layer and (b) 3000 Å SiO <sub>2</sub> with a piece of InP placed on top during post-implant anneal	91
5.6	Variation of Hall mobility with temperature in (a) SI InP:Fe and (b) SI InP:Cr	93
5.7	Plots of $R_H T^{3/2}$ versus inverse temperature in (a) SI InP:Fe and (b) SI InP:Cr	94
5.8	Plots of $(qR_H)^{-1}$ versus inverse temperature in (a) SI InP:Fe and (b) SI InP:Cr	95
5.9	Plots of dark conductivity, $\sigma$ , versus inverse temperature in (a) SI InP:Fe and (b) SI InP:Cr	96
5.10	Variation of Hall electron mobility with temperature in as-grown LPE InP	98
5.11	Variation of Hall electron mobility with temperature in Si-implanted and annealed LPE InP	99
5.12	Variation of Hall electron mobility with temperature in Si-Implanted and annealed SI InP	105
5.13	Calculated variation of the concentration of shallow and deep levels with the Fermi energy position in (a) SI InP:Fe and (b) SI InP:Cr	107
5.14	Calculated variations of the ratio $\mu_H/\mu_{Hm}$ with compensation ratio in (a) SI InP:Fe and (b) SI InP:Cr	109
5.15	Calculated variation of the ratio $p/n$ with compensation ratio in SI InP:Fe	110
5.16	Photocurrent spectra obtained at T = 100 and 223K for (a) SI InP:Fe and (b) SI InP:Cr	112
5.17	Plots of $(h\nu\Delta I_{ph})^{2/3}$ versus photon energy for (a) SI InP:Fe and (b) SI InP:Cr	114
5.18	Photoconductivity spectra obtained for Si-implanted and annealed SI InP	116

LIST OF SYMBOLS

A	Diode area ( $\text{cm}^2$ )
B	Magnetic flux density (Gauss)
C(t)	Time-dependent high frequency diode capacitance (F)
$C_0, C_\infty$	Diode capacitance at $t = 0, \infty$ (F)
$c_n, c_p$	Capture rates for electrons, holes ( $\text{sec}^{-1}$ )
$E_A, E_D$	Shallow acceptor and donor ionization energy (eV)
$E_{AA}, E_{DD}$	Deep acceptor and donor ionization energy (eV)
$E_F, E_{FM}$	Fermi energy in semiconductor, metal (eV)
$E_G$	Forbidden energy gap of a semiconductor (eV)
$E_i$	Photoionization energy of deep levels (eV)
$E_l$	Acoustic deformation potential (eV)
$\Delta E_B$	Energy barrier associated with deep-level trap (eV)
$\Delta E_T^0, \Delta E_T$	Activation energy of a trap at $T = 0, T$ (eV)
$e_n, e_p$	Thermal emission rate of electrons and holes from traps ( $\text{sec}^{-1}$ )
$e_{14}$	Piezoelectric constant ( $\text{coul./m}^2$ )
G	Photogeneration rate ( $\text{cm}^3 \cdot \text{sec}^{-1}$ )
$g_{AA}, g_{DD}$	Degeneracy factor for deep-level acceptors and donors
$g_n, g_p$	Degeneracy factor for electrons, holes
k	Boltzmann's constant ( $1.38 \times 10^{-23}$ J/K)
$L_D$	Debye length (cm)
$m^*$	Effective mass (kg)
$m_0, m_c, m_d$	Free electron mass, conductivity effective mass and density of states effective mass of electron (kg)
$N_A, N_D$	Shallow acceptor and donor density ( $\text{cm}^{-3}$ )

$N_c, N_v$	Effective density of states in the conduction band and in the valence band ( $\text{cm}^{-3}$ )
$N_{AA}, N_{DD}$	Concentration for deep acceptors and deep donors ( $\text{cm}^{-3}$ )
$N_{NI}$	Concentration of neutral impurities ( $\text{cm}^{-3}$ )
$N_T, N_T^+, N_T^-$	Total trap density, ionized electron density, and ionized hole density ( $\text{cm}^{-3}$ )
$n, p$	Free electron and hole concentrations in semiconductors ( $\text{cm}^{-3}$ )
$n_i$	Intrinsic carrier concentration ( $\text{cm}^{-3}$ )
$n_T$	Concentration of trapped electrons ( $\text{cm}^{-3}$ )
$\Delta n, \Delta p$	Excess concentration of electrons and holes ( $\text{cm}^{-3}$ )
$p_T(o)$	Equilibrium hole concentration in a hole trap ( $\text{cm}^{-3}$ )
$q$	Electric charge ( $1.6 \times 10^{-19}$ coul.)
$R_H$	Hall coefficient ( $\text{cm}^3/\text{coul.}$ )
$r$	Scattering factor
$v_n, v_p$	Thermal velocity for electrons, holes (cm/sec)
$W$	Depletion-region width in a diode (cm)
$\alpha$	Temperature coefficient of activation energy of a trap (eV/K)
$h\nu$	Photon energy (eV)
$\theta$	Optical phonon temperature (K)
$\epsilon_o$	Absolute permittivity of free space ( $8.85 \times 10^{-14}$ F/cm)
$\epsilon_r$	Relative permittivity
$\sigma, \Delta\sigma$	Dark- and Photo-conductivity ( $\text{ohm-cm}^{-1}$ )
$\sigma_i$	Photoionization cross section of traps ( $\text{cm}^2$ )

$\sigma_n, \sigma_p$	Thermal capture cross section of traps for electrons and holes ( $\text{cm}^2$ )
$\sigma_\infty$	Thermal capture cross section of traps at $T = \infty$ ( $\text{cm}^2$ )
$\tau_n$	Excess electron lifetime (sec)
$\mu_H$	Hall mobility ( $\text{cm}^2/\text{V.s}$ )
$\mu_n, \mu_p$	Mobility for electrons, holes ( $\text{cm}^2/\text{V.s}$ )
$\Delta\mu_n, \Delta\mu_p$	Change in electron and hole mobilities due to photo-excitation ( $\text{cm}^2/\text{V.s}$ )
$\rho_d$	Material density ( $\text{g}/\text{cm}^3$ )

## LIST OF TABLES

<u>Table</u>		<u>Page</u>
4.1	Characteristics of deep levels in SI GaAs:Cr	45
4.2	Characteristics of deep levels in SI undoped GaAs	46
4.3	Characteristics of deep levels in Si-implanted and annealed SI GaAs:Cr	48
4.4	Characteristics of deep levels in GaAs FETs fabricated by ion-implantation technology	51
4.5	Electrical characteristics of as-grown VPE GaAs	54
4.6	Electrical characteristics of implanted and annealed VPE GaAs	56
4.7	Transport data in SI GaAs:Cr obtained from Hall measurements	62
4.8	Transport data in SI undoped GaAs obtained from Hall measurements	63
4.9	Shallow and deep level concentrations and compensation ratios in SI GaAs:Cr determined from analysis of Hall-effect data	70
4.10	Shallow and deep level concentrations and compensation ratios in SI undoped GaAs determined from analysis of Hall-effect data	71
5.1	Characteristics of deep levels in SI InP:Fe and InP:Cr	84
5.2	Characteristics of deep levels in as-grown LPE InP	87
5.3	Characteristics of deep levels in Si-implanted and annealed LPE InP	89
5.4	Transport data in SI InP:Fe and InP:Cr obtained from Hall measurements	97
5.5	Electrical characteristics of as-grown LPE InP	100
5.6	Electrical characteristics of implanted and annealed LPE InP	101

<u>Table</u>		<u>Page</u>
5.7	Transport data in ion-implanted and annealed SI InP. The samples were thermally annealed with a 2000 Å silox encapsulating layer at 750 to 800°C for 20 min. in forming gas.	102
5.8	Transport data in ion-implanted and annealed SI InP. The samples were thermally annealed at 670°C for 20 min. with a 3000 Å silox encapsulating layer and a piece of InP placed on top	103
5.9	Shallow and deep level concentrations and compensation ratios in SI InP:Fe and InP:Cr determined from analysis of Hall-effect data	106

ELECTRICAL AND OPTICAL PROPERTIES OF SEMI-INSULATING AND  
ION-IMPLANTED GaAs AND InP

CHAPTER I

INTRODUCTION

The III-V semiconducting compounds GaAs and InP are technologically important materials for the fabrication of microwave and optoelectronic devices. This arises from the higher carrier mobilities in these compounds, compared to Si, and their band structure. Other material properties of these compounds and mixed crystals grown on them are being effectively used for the fabrication of novel devices.

The fabrication of reliable GaAs and InP Field Effect Transistors (FETs) and other microwave devices requires the availability of high-quality semi-insulating (SI) substrate materials. Most of the recent investigations<sup>(1,2,3)</sup> on SI GaAs and InP have been directly related to the electrical and optical properties of the Cr and Fe compensating levels, which act as deep acceptors, in these materials. The techniques which have been predominantly used are photoluminescence, d.c. and a.c. photoconductivity, and electron paramagnetic resonance (EPR) spectroscopy. Some transport properties in SI GaAs have been determined by Martin et al.<sup>(4)</sup> and in SI InP by Iseler<sup>(5)</sup>, respectively. In addition to the known properties of the Cr and Fe levels in SI materials<sup>(6)</sup>, it is important to determine the thermal emission properties of these levels, viz., their activation energies and capture cross sections for electrons and holes. There is also

no report on the thermal emission properties of other defect or impurity levels which might be present in SI InP. Furthermore, it is of interest to compare the traps in SI InP with those in bulk n-InP<sup>(7)</sup>, both types of material being grown by the liquid encapsulation Czochralski technique. Such information would aid in a better understanding of the electrical properties and compensation mechanisms in semi-insulating materials and the active layers subsequently grown on them.

Deep level defects in SI GaAs and InP, including the compensating Cr and Fe related levels, were detected and characterized in this study by the Photo-Induced Current Transient (PICT) measurement technique, first reported by Hurtes et al.<sup>(8)</sup>. This technique has to be employed since it is not possible to perform conventional capacitance transient or deep level transient spectroscopy (DLTS) measurements with Schottky barriers fabricated on materials exhibiting high resistivity. The nature of the traps were inferred by performing the PICT experiments with intrinsic and extrinsic monochromatic excitation. The energy position of some of the more dominant defect levels were also obtained from the variation of the photocurrent with incident photoexcitation energy and from analyses of these spectra. The physico-chemical origin of some of the traps have been inferred from the results of heat-treatment experiments.

The transport parameters in the semi-insulating materials were measured at high temperatures using the van der Pauw technique<sup>(9)</sup>. The variation of resistivity, Hall mobility and Hall coefficient

with temperature, for  $T > 350\text{K}$ , were determined. The mobility data were analyzed taking into account the relevant scattering mechanisms. The compensation in the materials and other important transport parameters were determined from a solution of the charge neutrality equations. These equations were appropriately derived for the materials under consideration. A detailed study of the transport properties, in conjunction with the investigation of deep levels in semi-insulating III-V compounds, is of prime importance to the user of these materials.

Recent progress in ion-implantation as a means of controlled doping of elemental and compound semiconductors have led to significant advances in the technology and fabrication of integrated circuits (IC). Implantation of high-energy donor ions into SI GaAs or InP and subsequent thermal or laser annealing produce n-type active layers whose thickness and carrier concentration can be controlled by the implant dose and energy. Deep level defects induced by the implant-and-anneal procedure can produce deleterious effects in the performance of FETs and similar devices<sup>(10,11,12)</sup>. Hence, it is imperative to detect, characterize, and reveal the origin of deep level defects in ion-implanted and annealed semiconductors. Data on deep levels will provide an additional measure of the quality of implanted materials. Some results on deep levels in Si-implanted and annealed GaAs:Cr<sup>(13,14)</sup> have recently been reported, but no detailed studies have yet been made.

Transient capacitance and photo-capacitance measurements were performed on implanted and annealed SI GaAs:Cr. Transient measure-

ments were also made directly on GaAs FETs fabricated by ion-implantation technology. In addition to thermal emission from the deep compensating Cr centers in GaAs, emission from several electron and hole traps with thermal activation energies ranging from  $0.15 \pm 0.01$  to  $0.90 \pm 0.01$  eV have also been detected and characterized<sup>(15)</sup>. Some properties of implanted InP have already been reported<sup>(16-18)</sup>. Silox encapsulation used to protect implanted InP during subsequent thermal annealing is known to decompose if the annealing temperature is too high and thickness of the encapsulating layer is below  $2000 \text{ \AA}$ <sup>(16-18)</sup>. This problem was investigated by observing the effects of the decomposition, if any, on the morphological and electrical properties of the implanted layers. At the same time the effects of  $\text{Si}_3\text{N}_4$  encapsulation, as an alternate protective layer, was also studied. The experimental techniques used to investigate the electrical properties and defects in implanted and annealed InP were Hall and photoconductivity spectra measurements. The Hall effect data were analyzed to determine the density of shallow and deep levels, compensation, and activation in the implanted layers. A dominant defect level at 0.56 eV from the conduction band was detected from photoconductivity spectra in implanted InP and the Cr and Fe levels were found to be present in implanted InP:Cr and InP:Fe, respectively.

Although the technological suitability of epitaxial semiconductors for directly implanted planar IC applications is yet to be demonstrated, an investigation was initiated in the course of this work to characterize vapor phase epitaxial (VPE) GaAs layers

before and after implantation. Deep levels in Be-implanted VPE GaAs have been characterized by Wilsey et al.<sup>(19)</sup>. The effect of ion-implantation and annealing on deep levels in liquid phase epitaxial (LPE) GaAs has been reported by Jervis et al.<sup>(20)</sup>. In the present investigation a detailed comparative study of the electrical and optical properties of VPE GaAs before and after Si-implantation and annealing has been made<sup>(21)</sup>. Several electron and hole traps have been detected and characterized. It is observed that traps which are dominant in the as-grown VPE layers are characteristically absent in the implanted and annealed material. Instead, new levels are observed. The  $0.52 \pm 0.01$  and  $0.15 \pm 0.01$  eV electron and hole trap levels consistently present in implanted VPE GaAs have also been identified in implanted GaAs:Cr and are thought to be characteristic of the implant-and-anneal process. A significant change has been observed in the temperature variation of the Hall mobility in VPE GaAs after implant and annealing, and this change has been interpreted. The electron mobilities over a wide range of temperature have been analyzed to determine the responsible scattering mechanisms.

Finally, InP was grown by liquid phase epitaxy as an alternate material for donor implantation. Preliminary investigations, using the techniques mentioned above, have been made on these epitaxial layers and the changes in their properties after implantation and annealing. LPE InP was found to contain a smaller concentration of deep levels both before and after implantation. Only one electron trap, with an activation energy of  $0.17 \pm 0.01$  eV, was

predominantly detected after implantation and annealing. The mobilities measured in LPE InP layers are slightly lower than the best values reported<sup>(22,23)</sup>. The temperature variation of mobility was similar to that in epitaxial and implanted GaAs.

Theoretical considerations are reviewed in Chapter II. Liquid phase epitaxy of InP is described in Chapter III. Properties of semi-insulating and ion-implanted GaAs and InP are presented and discussed in Chapters IV and V, respectively. Concluding remarks and suggestions for future work have been made in Chapter VI.

## CHAPTER II

THEORETICAL CONSIDERATIONS

The theoretical considerations underlying the measurement techniques used in the course of this study to characterize the electrical and optical properties of semiconductors are briefly reviewed in this chapter.

2.1 Defects and Deep Levels in a Semiconductor

Defects or imperfections can be described as disruptions in a crystal lattice. The absence of an atom from a normally occupied lattice site is called a vacancy. A foreign atom occupying the site of a matrix atom gives rise to a substitutional impurity. An interstitial impurity results when the foreign atom is located in the interstice between matrix atoms. A host atom may leave its site, creating a vacancy, and be located interstitially in the crystal structure. The associated vacancy-interstitial pair is called a Frenkel defect. When a cation vacancy is associated with an anion vacancy rather than an interstitial cation, the pair is called a Schottky defect. Chemical interaction between two or more of the above-mentioned defects results in complex defects.

The defects described above can produce localized energy states located deep in the forbidden energy gap of a semiconductor. Such deep levels are not significantly thermally ionized at room temperature. The large ionization energy of these levels implies a strong potential which acts to localize the carrier wave functions near the

site of the defect. Consequently deep-level centers are delocalized in k-space. Deep levels can act as donors, acceptors, traps or recombination centers.

The charge state of a deep-level center positioned below the equilibrium Fermi level is neutral when acting as an electron trap and is negative when acting as a hole trap. A deep level positioned above the equilibrium Fermi level is neutral when acting as a hole trap and is positively charged when acting as an electron trap. The relative importance of trapping and recombination depends on the location of the deep level relative to the Fermi level and on the asymmetry of the carrier capture cross sections<sup>(24)</sup>. Normally, an electron trap has a large electron capture cross section in contrast to a small hole capture cross section, and *vice versa* for a hole trap.

## 2.2 Theory of Capacitance Transient and Photo-Induced Current Transient Measurements

The thermal emission rates of carriers in the depletion region of a Schottky diode can be determined by using Shockley-Read-Hall statistics<sup>(25,26)</sup> and the detailed balance relationship<sup>(27)</sup>;

$$e_{n(p)} = E_{n(p)} T^2 \exp[-(\Delta E_T^O + \Delta E_B)/kT] \quad (2-1)$$

where

$$E_{n(p)} = 3.26 \times 10^{21} g_{n(p)} \sigma_{\infty} \frac{(m_d/m_o)^{3/2}}{(m_c/m_o)^{1/2}} \exp(\alpha/k) \quad (2-2)$$

Here,  $\Delta E_T = \Delta E_T^O - \alpha T$  is the activation energy of the trap and  $\alpha$  its temperature coefficient,  $g_{n(p)}$  is the spin degeneracy factor and  $m_d$

and  $m_c$  are, respectively, the density of states mass and the conductivity mass of carriers.  $\sigma_{n(p)} = \sigma_\infty \exp(-\Delta E_B/kT)$  is the thermally activated capture cross section with energy barrier  $\Delta E_B$ . The subscripts n and p represent, respectively, electrons and holes.

With reference to Fig. 2.1, the electron traps can be filled with electrons when a small forward bias is applied to a Schottky diode. Upon changing the bias from a small forward value to a large reverse value at  $t = 0$ , the filled traps in the region  $0 < x < \lambda$  of the depletion region are thermally ionized in accordance to the relation:

$$N_T^+ = N_T [1 - \exp(-e_n t)] \quad (2-3)$$

where  $N_T$  is the total concentration of the traps. The electrons emitted to the conduction band are swept out of the depletion region by the electric field. Under conditions of small trap density and large reverse bias, the resulting capacitance transient can be approximately described by<sup>(28)</sup>

$$C(t) = C_\infty + (C_0 - C_\infty) \exp(-e_n t) \quad (2-4)$$

where  $C_0$  and  $C_\infty$ , respectively, are the values of capacitance at  $t = 0^+$  and  $t = \infty$ . The thermal activation energy and capture cross section of the electron trap can be determined using Eqs. (2-1), (2-2) and (2-4). The concentration of the trap can be obtained directly from the capacitance change by using the approximate relationship<sup>(29)</sup>:

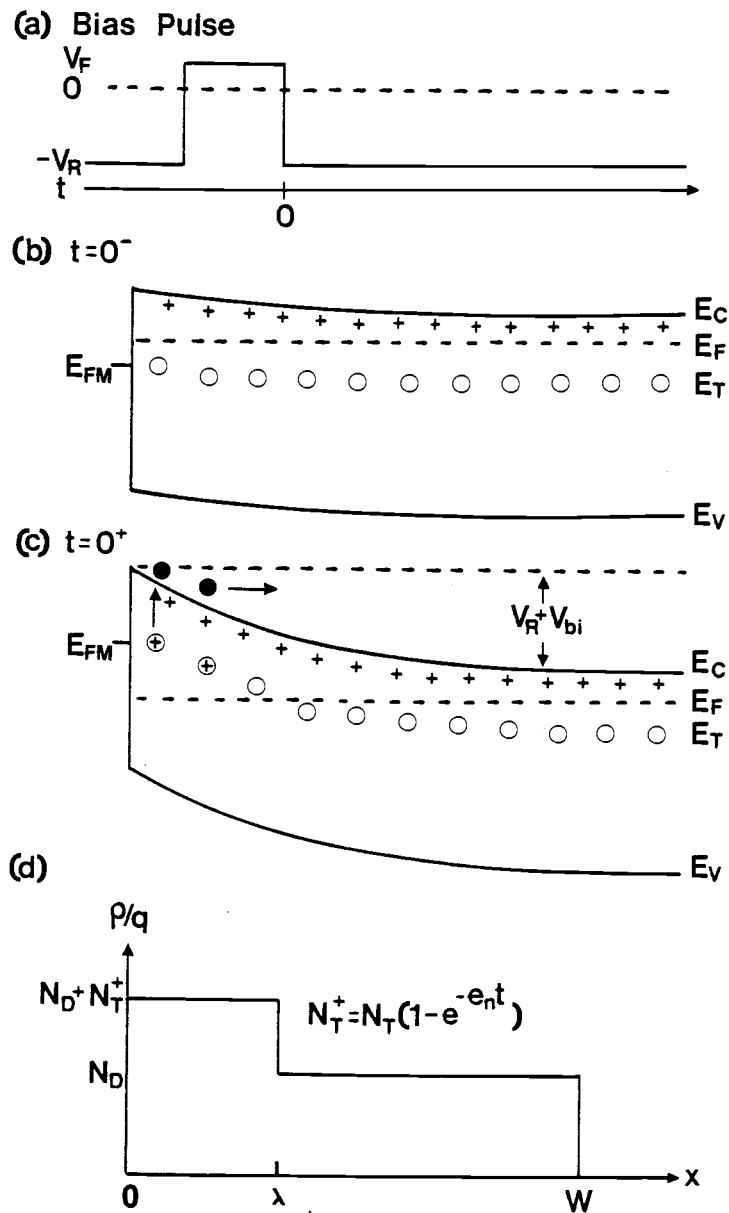


Figure 2.1. Variation of experimentation parameters related to electron trap emission from the depletion region of a metal-n-semiconductor junction: (a) Filling bias pulse, (b) filling of electron trap levels in the depletion region by a forward bias pulse, (c) thermal re-emission of electrons after bias switched back to the quiescent reverse value, (d) instantaneous charge-density profile in depletion region with electron traps empty.

$$N_T \approx \frac{2\Delta C}{C_\infty} (N_D - N_A) \quad (2-5)$$

where  $\Delta C = C_\infty - C_0$  is the capacitance change due to trapping at the instant when the bias is switched to the quiescent reverse value.

Hole traps in the depletion region can be filled with holes generated by an optical pulse. During illumination the trap is located above the hole quasi-Fermi level, as shown in Fig. 2.2. After the illumination is removed, the hole traps thermally re-emit captured holes to the valence band in accordance with <sup>(21)</sup>

$$N_T^- = N_T [1 - \exp(-e_p t)] \quad (2-6)$$

Under an exponential approximation of the emission process the variation of the diode capacitance is approximately described by <sup>(30)</sup>

$$C(t) \approx C_\infty \left[ 1 + \frac{p_T(o)}{2n} \exp(-e_p t) \right] \quad (2-7)$$

where  $p_T(o)$  is the equilibrium hole concentration in the trap just before the illumination is switched on.

The exponential approximation of the capacitance transients are no longer valid when trap densities are large, i.e., they become comparable to the free-carrier concentration in the material. This has to be taken into account in the analysis of the data in order to derive the true emission rates <sup>(31,32)</sup>. The capacitance transients due to hole emission from hole traps are always found to be non-exponential, irrespective of the trap density. It may be remembered

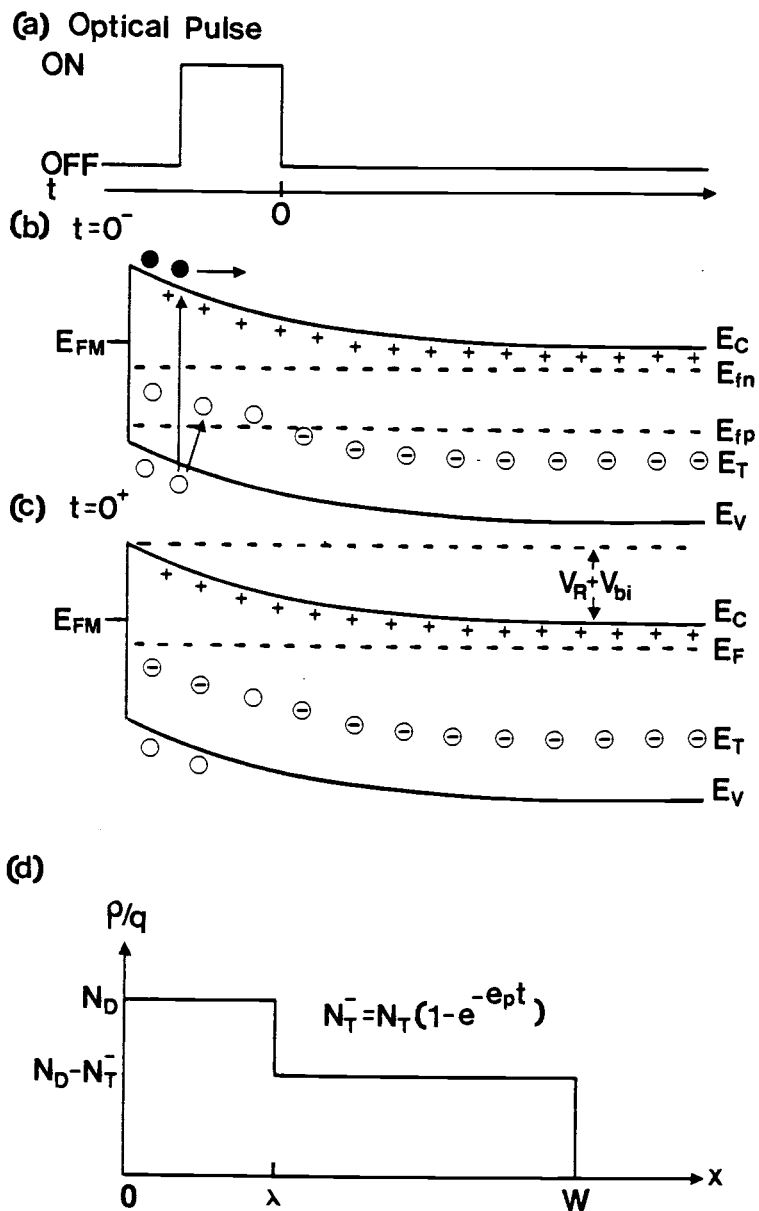


Figure 2.2. Variation of experimentation parameters related to hole trap emission from the depletion region of a metal-n-semiconductor junction: (a) optical pulse, (b) filling of hole trap levels in the depletion region by photoexcitation, (c) thermal re-emission of holes after cessation of the photoexcitation, (d) instantaneous charge-density profile in depletion region with hole traps empty.

that the occupancy of hole traps is determined by the hole quasi-Fermi level in the depletion region. The edge of the depletion region is not abrupt; the free-carrier density  $n(x)$  at a distance  $x$  from the edge falls off according to<sup>(21)</sup>

$$n(x) \approx n \exp[-(x^2/2L_D^2)] \quad (2-8a)$$

with 
$$L_D = (\epsilon_r \epsilon_o kT/q^2 n)^{1/2} \quad (2-8b)$$

where  $L_D$  is the Debye length and  $x$  is the distance from the outer edge. This tail of free carriers, which can even penetrate the space charge region of the depletion layer depending on the free carrier density and the position of the quasi-Fermi level for holes, would affect trapping and detrapping from the centers. The electric field profile would consequently be affected, leading to nonexponential capacitance transients.

Transient capacitance and photocapacitance measurements, as described above, cannot be used with semi-insulating materials due to the lack of carriers therein. Excess carriers can, however, be generated by optical excitations and some of them may be trapped at the deep centers. Subsequent thermal emission of the trapped carriers in the dark is then monitored as a function of temperature by Photo-Induced Current Transient (PICT) measurements.

The current change after the photoexcitation is switched off can be expressed by<sup>(8,33)</sup>

$$i(t) = K\{e_n n_T(t) + e_p [N_T - n_T(t)]\} \quad (2-9)$$

where the constant  $K$  includes the geometrical parameters of the device and the penetration depth of the light pulse, and  $n_T$  is the concentration of trapped electrons. Assuming an exponential emission, the measured transient current is then given by

$$\Delta i(t) = K(e_n - e_p) [n_T(0) - n_T(\infty)] \exp[-(e_n + e_p)t] \quad (2-10)$$

where  $n_T(0)$  and  $n_T(\infty)$  are expressed, respectively, by

$$n_T(0) = N_T \left[ 1 + \frac{e_n + c_p \Delta p}{e_p + c_n \Delta n} \right]^{-1} \quad (2-11a)$$

and

$$n_T(\infty) = N_T \left[ 1 + \frac{e_n}{e_p} \right]^{-1} \quad (2-11b)$$

Here,  $\Delta n$  and  $\Delta p$  are, respectively, excess carriers generated by the photoexcitation, and  $c_n$  and  $c_p$  are, respectively, capture rates for electrons and holes. The emission rates, in general, are much slower than capture rates at high-level excitations. Under this condition and the assumption  $e_n \gg e_p$  for electron traps, Eq. (2-10) can be rewritten as

$$\delta i(t) = K N_T e_n \exp(-e_n t) \quad (2-12a)$$

and

$$e_n = \sigma_n v_n g_n N_c \exp(-\Delta E_T/kT) \quad (2-12b)$$

Therefore, the trap parameters can be obtained from Eq. (2-12) by recording the transient current at several fixed temperatures. Similar expressions describe dominant hole emission from hole traps.

For experiments with intrinsic photoexcitation, the distinction between electron- and hole-trap emission can be made by observing the direction of the transient current variation. A decay transient with the current decreasing to the quiescent dark current results from hole emission. An undershoot at the cessation of photoexcitation, followed by a current increasing to the quiescent current results from electron trap emission. This can be explained by assuming the presence of large-cross-section centers containing captured photo-excited holes and a rapid recombination of these holes with free and very shallow trapped electrons. The deep compensating centers in semi-insulating materials are usually characterized by large cross sections. The above mechanism has been analyzed by Bube<sup>(34)</sup>. The distinction between electron and hole emission can also be made by extrinsic photoexcitation, which directly alters the population of the trap levels.

### 2.3 Theory of Transport Measurements

The van der Pauw technique<sup>(9)</sup> was used to measure the resistivity, Hall coefficient and Hall mobility of carriers in implanted and semi-insulating materials. These parameters in the implanted semiconductors were measured and calculated by the well known equations<sup>(9)</sup>.

Hall measurements on semi-insulating semiconductors become

difficult due to surface leakage problems. In addition, due to the high resistivity, the measurements have to be performed at  $T > 300\text{K}$ . Since mixed-carrier conduction is operative, the conductivity, Hall coefficient and Hall mobility are given by the expressions:

$$\sigma = q\mu_n n(1 + 1/bc) \quad (2-13)$$

$$R_H = r \frac{(1 - b^2 c) \sqrt{c}}{qn_i (1 + bc)^2} \quad (2-14)$$

and

$$\mu_H = r \frac{\mu_n (1 - b^2 c)}{b(1 + bc)} \quad (2-15)$$

where  $b = \mu_n / \mu_p$ .  $r$  is the scattering factor and can be taken as unity unless it is strongly temperature dependent,  $c = n/p$ , and  $n_i$  is the intrinsic carrier concentration. The electron and hole mobilities were also calculated theoretically for the entire temperature range of measurement by considering the different carrier-scattering mechanisms and using Matthiesen's rule<sup>(35)</sup>. Neutral impurity scattering needs to be included because of the proximity of deep compensating levels to the Fermi level in semi-insulating materials. The mobility due to scattering by neutral impurities, including the short-range attractive potential of the neutral centers,  $N_{NI}$ , is<sup>(36)</sup>

$$\mu_{NI} = \frac{1.17 \times 10^{22} (m^*/m_0)}{\epsilon_r \epsilon_0 N_{NI}} (7.34 \times 10^{-3} \delta + 30.2/\delta) (\text{cm}^2/\text{V.s}) \quad (2-16a)$$

where 
$$\delta = \epsilon_r \epsilon_o \sqrt{T/(m^*/m_o)} \quad (2-16b)$$

The Fermi energy,  $E_F$ , is determined from an accurate solution of the charge neutrality equation by Newton's iterative method.

With reference to Fig. 2.3(a) the equations for a material with a single deep compensating acceptor level are developed below. Additional levels can be readily incorporated. The charge neutrality condition for shallow donor and acceptor levels and a deep acceptor level, in the mid-band gap region, can be written as

$$n = p + N_D^+ - N_A^- - N_{AA}^- \quad (2-17)$$

where  $N_{AA}^-$  denotes the ionized densities of the deep acceptors. If full ionization is assumed for the shallow levels, then Eq. (2-17) may be written as

$$n + p + (N_D - N_A) - \frac{N_{AA}}{1 + g_{AA} \exp[(E_{AA} - E_F)/kT]} \quad (2-18)$$

where  $g_{AA}$  is the degeneracy factor of the deep acceptor level.

Eq. (2-18) can also be rewritten as

$$n^2 + n \left[ \frac{N_{AA}}{1 + F_{AA}/n} - (N_D - N_A) \right] - n_i^2 = 0 \quad (2-19)$$

where

$$F_{AA} = g_{AA} N_c \exp[(E_{AA} - E_G)/kT] \quad (2-20)$$

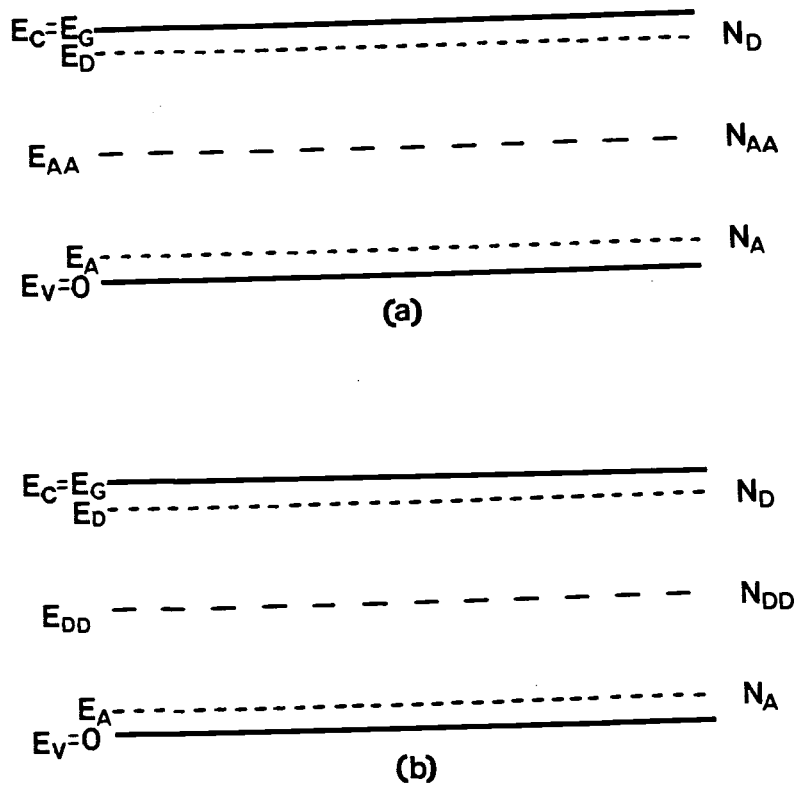


Figure 2.3. Energy level models used to analyze transport data in semi-insulating semiconductors with (a) a single deep compensating acceptor level, (b) a single deep compensating donor level.

and  $N_{AA}$  is the total concentration of deep-level acceptors. Here, the temperature dependence of the forbidden energy gap,  $E_G(T)$ , is given by

$$E_G(T) = 1.519 - \frac{5.4 \times 10^{-4} T^2}{T+204} \quad \text{for GaAs} \quad (37) \quad (2-21a)$$

and

$$E_G(T) = 1.4206 - \frac{4.906 \times 10^{-4} T^2}{T+327} \quad \text{for InP} \quad (38) \quad (2-21b)$$

The Fermi function can alternately be written as

$$f(E_{AA}) = \frac{1}{1 + g_{AA} \frac{N_C}{n} \exp[(E_{AA} - E_G)/kT]} \quad (2-22)$$

The quantity  $N_{AA}/(N_D - N_A)$  is the degree of compensation. When its value is less than unity,  $n \approx N_D - N_A$ . When its value is greater than or equal to unity,  $n$  decreases drastically with increase in the value of the compensation ratio and its value approaches that of  $n_i$ . Therefore, for the deep acceptors to control the resistivity in the semi-insulating semiconductor, the following conditions must hold:

$$N_D > N_A \quad \text{and} \quad N_{AA} > N_D - N_A$$

For such cases, the solution to Eq. (2-19) may be approximately written as

$$n \approx F_{AA} / \left( \frac{N_{AA}}{N_D - N_A} - 1 \right) \quad (2-23)$$

which, by virtue of Eq. (2-20), can be expressed as

$$n \approx \frac{g_{AA} N_c}{\frac{N_{AA}}{N_D - N_A} - 1} \exp[-(E_G - E_{AA})/kT] \quad (2-24)$$

This equation is true when  $n$  has a low value and is nearly equal to  $p$ . Substitutions of Eq. (2-24) into Eqs. (2-13) and (2-14) lead to

$$\sigma(T) = \frac{q\mu_n N_v}{g_{AA} b} [CR-1] \left\{ \exp\left(-\frac{E_{AA}}{kT}\right) + \frac{g_{AA}^2 b N_c}{N_v (CR-1)^2} \exp\left(-\frac{E_G - E_{AA}}{kT}\right) \right\} \quad (2-25)$$

and

$$R_H(T) = r \frac{g_{AA}}{qN_v (CR-1)} \frac{\exp\left(\frac{E_{AA}}{kT}\right) - g_{AA}^2 b^2 N_c \exp[(3E_{AA} - E_G)/kT]/N_v (CR-1)^2}{\left\{1 + g_{AA}^2 b N_c \exp[(2E_{AA} - E_G)/kT]/N_v (CR-1)^2\right\}^2} \quad (2-26)$$

where  $CR = N_{AA}/(N_D - N_A)$ . Equations (2-24), (2-25) and (2-26) can be suitably modified if additional deep levels are used in the compensation model. For larger values of  $n$ , such that  $F_{AA}/n \ll 1$ , one can write from Eq. (2-19),

$$n \approx [(N_D - N_A) g_{AA} N_c]^{1/2} \exp\left(-\frac{E_G - E_{AA}}{2kT}\right) \quad (2-27)$$

where it has been assumed that the compensation ratio is approximately equal to unity.

Similarly, with reference to Fig. 2.3(b), the charge neutrality condition in a material with a single deep donor level can be expressed by

$$n^2 + n[(N_A - N_D) - \frac{N_{DD}}{1+nF_{DD}}] - n_i^2 = 0 \quad (2-28)$$

where  $N_{DD}$  is the total concentration of deep donors, and

$$F_{DD} = \frac{\exp[(E_G - E_{DD})/kT]}{g_{DD} N_C} \quad (2-29)$$

Here,  $g_{DD}$  is the degeneracy factor of the deep donor level. Assuming the material is nearly fully compensated, the solution to Eq. (2-28) may be approximately expressed as

$$n \approx \left[ \frac{N_{DD}}{N_A - N_D} - 1 \right] g_{DD} N_C \exp[-(E_G - E_{DD})/kT] \quad (2-30)$$

Substitution of this equation into Eqs. (2-13) and (2-14) results in

$$\sigma(T) = q\mu_n [CRU - 1] g_{DD} N_C \left\{ \exp[-(E_G - E_{DD})/kT] + \frac{N_v \exp(-\frac{E_{DD}}{kT})}{g_{DD} [CRU - 1]^2 N_C} \right\} \quad (2-31)$$

and

$$R_H(T) = r [CRU - 1] \frac{g_{DD}}{qN_v} \frac{\{\exp(E_{DD}/kT) - b^2 [CRU - 1]^2 g_{DD}^2 N_C \exp[(-E_G + 3E_{DD})/kT]/N_v\}}{\{1 + b [CRU - 1]^2 g_{DD}^2 N_C \exp[(-E_G + 2E_{DD})/kT]/N_v\}^2} \quad (2-32)$$

where  $CRU = N_{DD}/(N_A - N_D)$ .

Analyses of the temperature dependence of low-field Hall data yield the charge-carrier transport parameters such as the carrier concentration, mobility, impurity doping concentration and impurity ionization energy. The Fermi level and the compensation ratio can also be accurately estimated.

## 2.4 Theory of Photoconductivity and Photocurrent Spectra

Photoconductivity in a semiconducting material results from the change in its resistance due to optical generation of extra carriers either from a deep level or from the valence band.

The dark conductivity, at low magnetic fields, is given by

$$\sigma = q(\mu_n n + \mu_p p) \quad (2-33)$$

Under photoexcitation, the photoconductivity can be expressed as

$$\Delta\sigma = q(\mu_n \Delta n + n\Delta\mu_n + \mu_p \Delta p + p\Delta\mu_p) \quad (2-34)$$

where  $\Delta\mu_n$  and  $\Delta\mu_p$  are, respectively, the changes in electron and hole mobilities due to photoexcitation. Assuming that electron emission from deep levels due to extrinsic photoexcitation is dominant, Eq. (2-34) can be approximately expressed as

$$\Delta\sigma = q(\mu_n \Delta n + n\Delta\mu_n) \quad (2-35)$$

The resulting photocurrent in the steady state is given by

$$\Delta I_{ph} = q(\mu_n \Delta n + n\Delta\mu_n)VA/L \quad (2-36)$$

where  $V$  and  $L$  are, respectively, the applied voltage and distance between contacts, and  $A$  is the area of the top contact. The excess carrier density,  $\Delta n$ , is related to the photogeneration rate  $G$  and

the excess carrier lifetime  $\tau_n$  by

$$\Delta n = G\Delta\tau_n + \tau_n\Delta G \quad (2-37)$$

where  $\Delta\tau_n$  and  $\Delta G$  are, respectively, a change in the excess carrier lifetime and in the photogeneration rate. A variation of the excess carrier lifetime may result from either a change in the effective capture cross section or in the distribution of recombination centers. The changes in mobility,  $\Delta\mu$ , are mainly due to variation of the effective charge of the impurity centers, intervalley transitions and lowering of effective barrier heights in an inhomogeneous photoconductor.

Since an onset or a rise of photosensitivity observed in a typical photoconductivity spectra are indicative of photoionization processes, it is possible to determine the ionization energy of deep levels responsible for such changes by suitable interpretation of the data. For a small effective mass of electrons, the photoionization cross section  $\sigma_i(h\nu)$  may be expressed as <sup>(39)</sup>

$$[\sigma_i(h\nu) \times h\nu]^{2/3} \propto h\nu - E_i \quad (2-38)$$

where  $E_i$  is the ionization energy of deep levels. From plots of  $(\Delta I_{ph} h\nu)^{2/3}$  or  $(\Delta\sigma h\nu)^{2/3}$  versus photon energies,  $h\nu$ , the intercepts of the linear regions on the energy axis give the different transition or ionization energies.

## CHAPTER III

LIQUID PHASE EPITAXIAL GROWTH OF InP

Epitaxy is the regularly oriented growth of a single crystal on a similar crystal called the substrate. Liquid phase epitaxy (LPE) is the process by which a thin single crystal film grows by the precipitation of a crystalline phase from a super saturated solution of the constituents. Epitaxial InP was grown in the course of this study to determine their electrical properties and to establish the changes in these properties after Si-implantation and thermal annealing. The following sections describe the LPE growth technique and growth conditions affecting the surface morphology and electrical properties of epitaxial InP.

### 3.1 Growth System and Techniques

The schematic of the liquid phase epitaxial (LPE) growth system is shown in Fig. 3.1(a). The semitransparent furnace tube, gold-coated on the inside, has a constant temperature profile within 1°C over 75% of the length of the heating coil. The furnace temperature is controlled by a EURO THERM Model 917 controller along with a EURO THERM Model 931 SCR power supply. The reactor tube is made of fused quartz and housed inside the furnace. The temperature of the growth cell is monitored by a chromel-alumel thermocouple. Another chromel-alumel thermocouple, located near the bottom of the growth cell, is used for controlling the temperature. The cooling rate during epitaxial growth is controlled by a EURO THERM Model 125

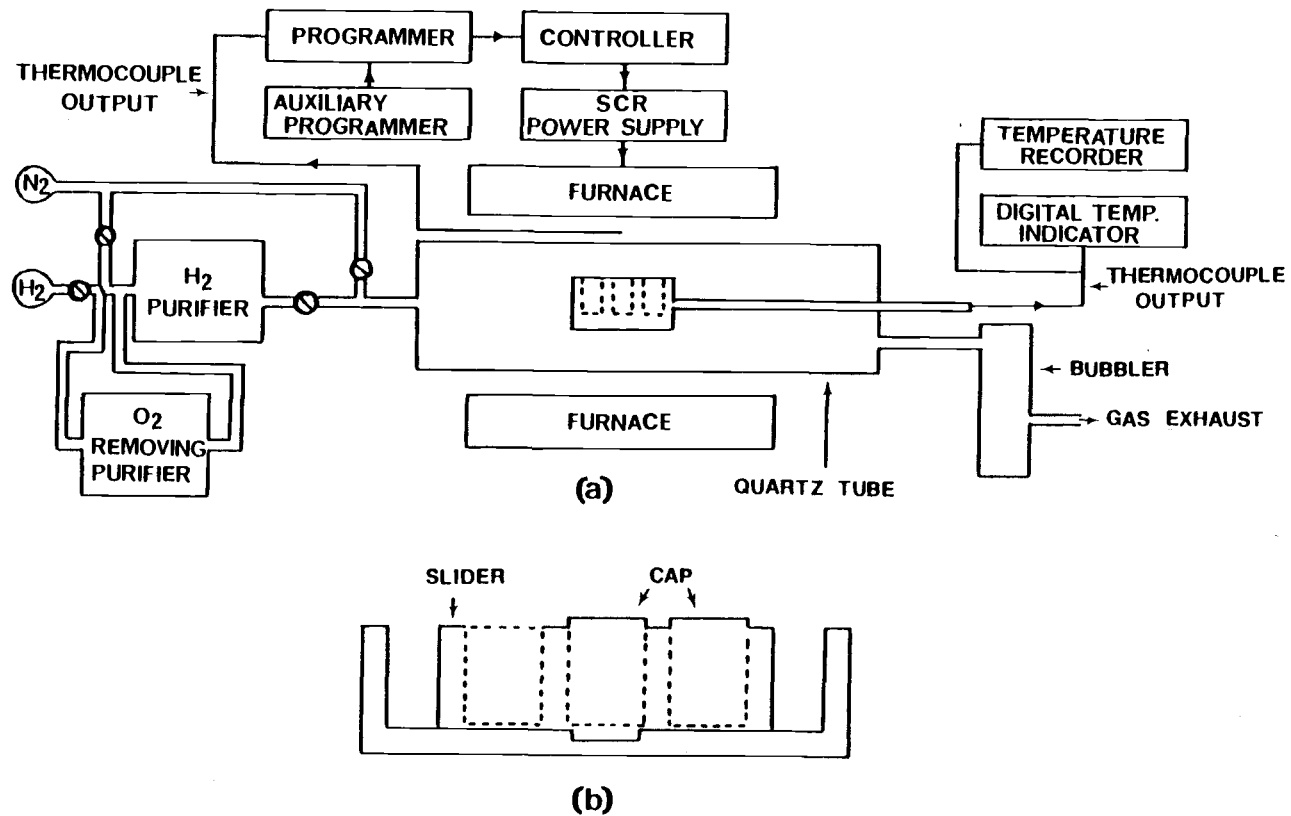


Figure 3.1. Schematic of LPE growth system: (a) LPE growth system, (b) graphite boat with a slider.

programmer and can be varied from 0.1 to 1.9°C/min. To minimize contamination in the system, Pd-diffused purified H<sub>2</sub> is continuously passed through the reactor at a rate of 0.7 standard cubic feet per hour (SCFH). In addition, an O<sub>2</sub>-purifying unit is used to prevent O<sub>2</sub> from being introduced into the H<sub>2</sub> purifier. The H<sub>2</sub> gas, used as the ambient during crystal growth, is exhausted through a silicone oil bubbler.

### 3.2 Materials Preparation for Epitaxial Growth

Successful epitaxial growth depends largely on the availability of defect-free and clean substrates. A rigid procedure has to be followed to minimize the damage introduced into the substrate during substrate preparation and handling. The surface morphology of polished, (100)-oriented InP substrates obtained from Varian Associates were further improved by chemi-mechanical polishing with bromine methanol. The polishing was done on KODAK lens-cleaning paper in successively weaker bromine methanol solutions. The final polish was achieved with a 0.5% solution. The polished substrate was degreased by boiling sequentially in high-purity trichloroethylene (TCE), acetone, and isopropyl alcohol (IPA). Usually this procedure was followed by a 30 sec etch in aqueous HCl (1:1) and a final rinse in IPA. The substrate was dried in IPA vapor and loaded in the growth cell. The same procedure was used to clean the polycrystalline InP source material. Indium to be used as the melt was etched in aqueous HNO<sub>3</sub> (1:1) for 1 or 2 min. immediately before each growth sequence.

### 3.3 Growth Procedure

The starting materials for LPE growth were grade AlA (6N) In and high-purity undoped polycrystalline InP as the source for P. Typical free-carrier concentration and mobility in the polycrystalline material were  $1.2 \times 10^{15} \text{ cm}^{-3}$  and  $5700 \text{ cm}^2/\text{V.s}$ , respectively, at 300K, and  $1.0 \times 10^{15} \text{ cm}^{-3}$  and  $74,700 \text{ cm}^2/\text{V.s}$ , respectively, at 77K. The semi-insulating (SI) InP:Fe substrates, grown by the liquid encapsulated Czochralski (LEC) technique, were oriented in the (100) crystallographic direction and had resistivities greater than  $10^7$  ohm-cm at room temperature. The etch-pit density in the substrates was less than  $5 \times 10^3 \text{ cm}^{-2}$ .

The time-temperature cycle for a typical epitaxial growth run is shown in Fig. 3.2. The graphite boat was initially heated at  $1300^\circ\text{C}$  under a vacuum of  $\sim 10^{-6}$  Torr for 10 hr. The boat was then loaded with approximately 4 g In in two wells (Fig. 3.1(b)) and baked at  $730^\circ\text{C}$  in the reactor tube for 72 hr under a  $\text{H}_2$ -flow-rate of 0.7 SCFH. At the end of this procedure the boat was cooled to room temperature and the In was removed. This baking is necessary to enable the dissolution of residual impurities from the boat into the In<sup>(40)</sup>. The boat was next loaded with 4 g In for the *in situ* etching<sup>(41)</sup>, 2.5 g In for the melt, and an appropriate amount of polycrystalline InP needed to saturate the melt. The reactor tube was sealed and purged with  $\text{H}_2$  for at least two hours (A to B in Fig. 3.2). The In-InP solution was then baked at  $700^\circ\text{C}$  for 10 hr. During this period (C to D) the In-InP solution was covered with a graphite cap to prevent evaporation of the volatile P. At time E, the polished and

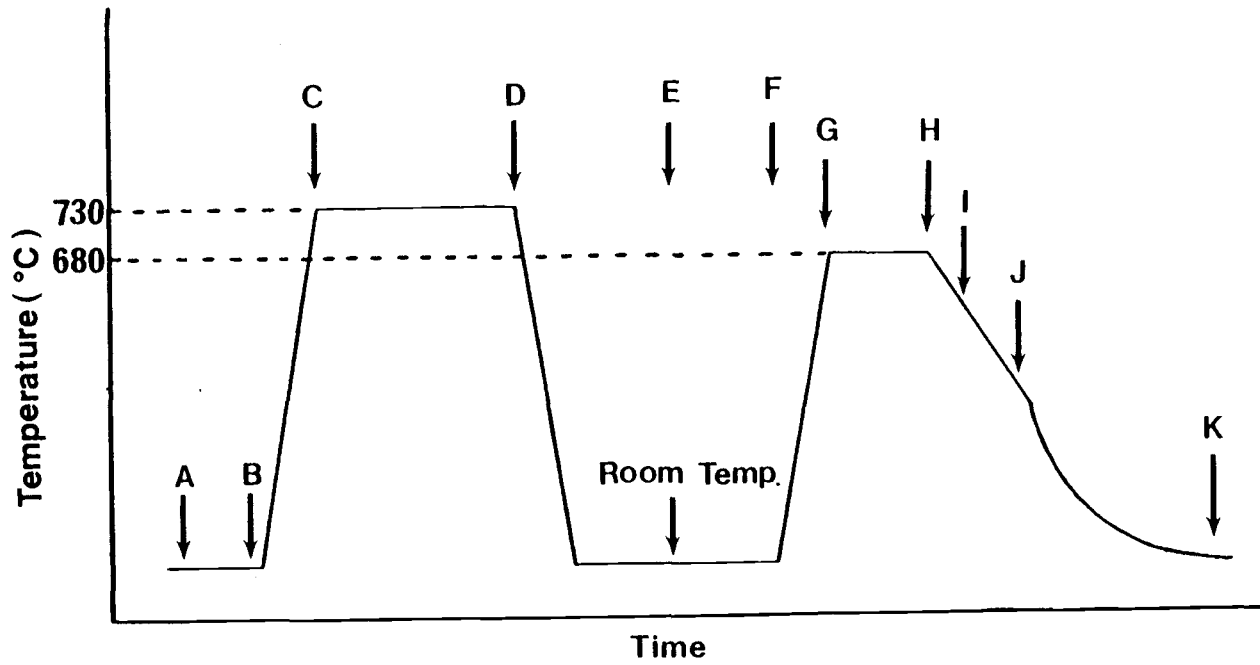


Figure 3.2. Time-temperature cycle for a typical epitaxial growth run with ramp-cooling and *in situ* meltback etching.

cleaned substrate was loaded into the boat at room temperature. The growth system was again purged with  $H_2$  for two hr (E to F). The temperature was then raised to, and held at, the growth temperature for 30 min. During this time (G to H) the substrate was covered with a graphite cap to minimize loss of P from its surface. The boat and its charge were then cooled at  $1^\circ C/min$ . When the temperature of the saturated In melt was  $5^\circ C$  below the growth temperature (time I), *in situ* etching of the substrate was accomplished by sliding the second pure In melt on top of the substrate for a few seconds. Epitaxial growth was initiated by pulling the In-InP saturated melt on the substrate. Growth was terminated by sliding the melt away from the grown epitaxial layer (time J). The growth time typically varied from 15 to 20 min. The furnace was then cooled to room temperature, the epitaxial layer was removed from the boat and any In adhering to its surface was removed by soaking in concentrated  $HNO_3$  at room temperature.

### 3.4 Layer Characterization

Morphological and electrical characteristics of the epitaxial layers were evaluated after each growth run. These evaluations provided necessary information for adjustments during subsequent growth.

#### 3.4.1 Layer Thickness

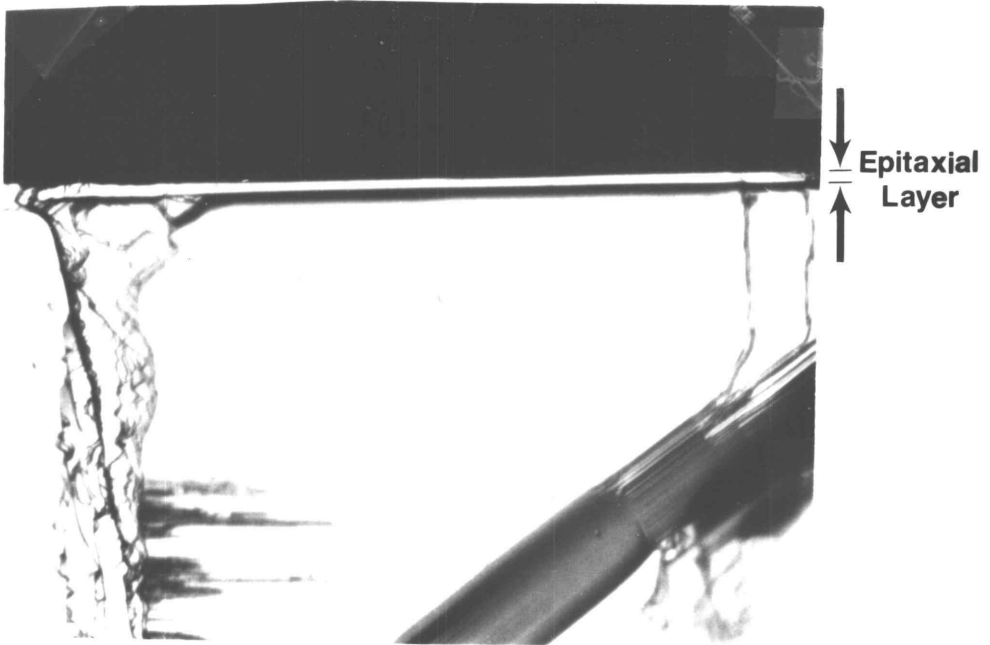
The epitaxial layer thickness was estimated by delineating the epitaxial layer-substrate junction on a cleaved face by the A-B dislocation etch technique<sup>(42)</sup>. Interfaces in InP were delineated

by dipping the cleaved (110) face into the hot ( $\sim 50-75^{\circ}\text{C}$ ) etchant for 2 or 3 min. Figure 3.3(a) shows the photomicrograph of a typical cleaved edge with the delineated interface between the substrate and the grown InP epitaxial layer. The thickness of the epitaxial layer was accurately measured by a calibrated microscope. Typical layer thicknesses varied from 4 to 5  $\mu\text{m}$ . As seen in Fig. 3.3(a), the interface is planar and the layer thickness is quite uniform.

#### 3.4.2 Surface Morphology

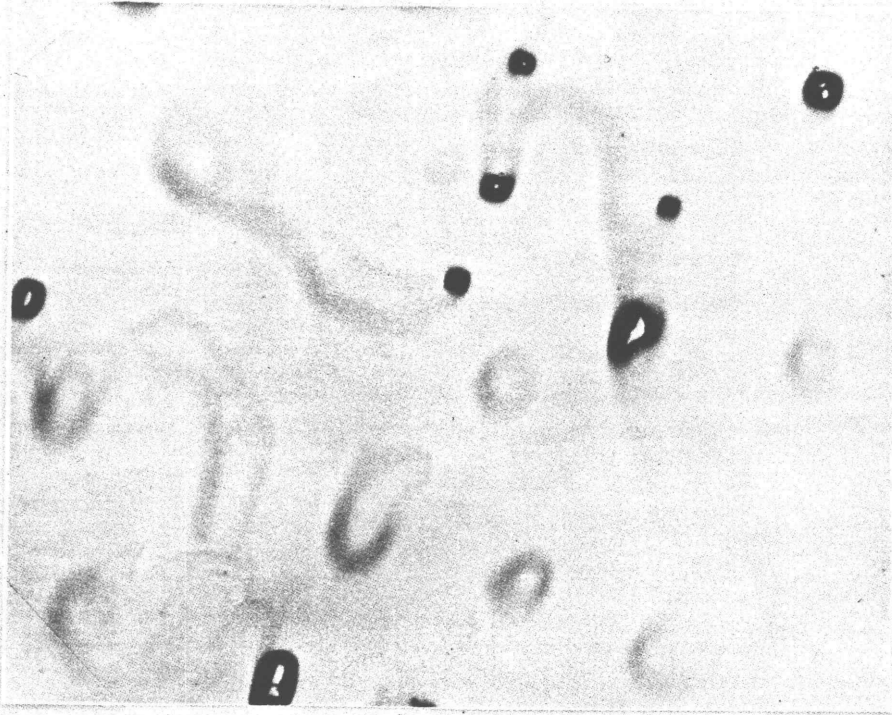
The surfaces of several LPE layers grown in the course of this study were mirror-like, as shown in Fig. 3.3(b). Indium inclusions, as shown in Fig. 3.4(a), were sometimes found to be present. A few layers had isolated morphologically degraded areas caused by poor wetting of the substrate by the growth solution. Figure 3.4(b) shows such a region. The poor wetting is believed to be caused by a residual oxide film on the substrate surface, in spite of the *in situ* etching. Figures 3.5(a) and (b) show remains of polycrystalline InP on the LPE layers.

Figures 3.6(a) highlights the ripple morphology commonly observed on the surface of InP LPE layers<sup>(43)</sup>. Earlier work on the growth of LPE InP has indicated that the surface morphology is strongly dependent on substrate orientation<sup>(44)</sup>. Pak et al.<sup>(45)</sup> have reported that the ripples appear on a misoriented surface and the average direction of the ripple front is at right angles to the gradient of the misoriented substrate plane. These authors

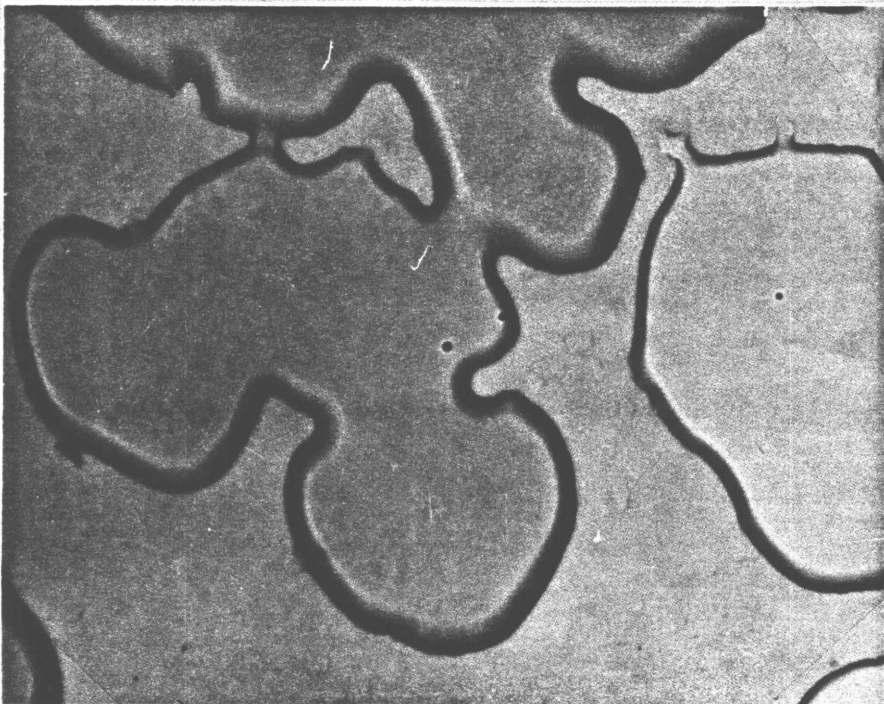


(b) 50  $\mu\text{m}$

Figure 3.3. Photomicrographs of (a) the cleaved cross section of an LPE layer and (b) mirror-like surface morphology.

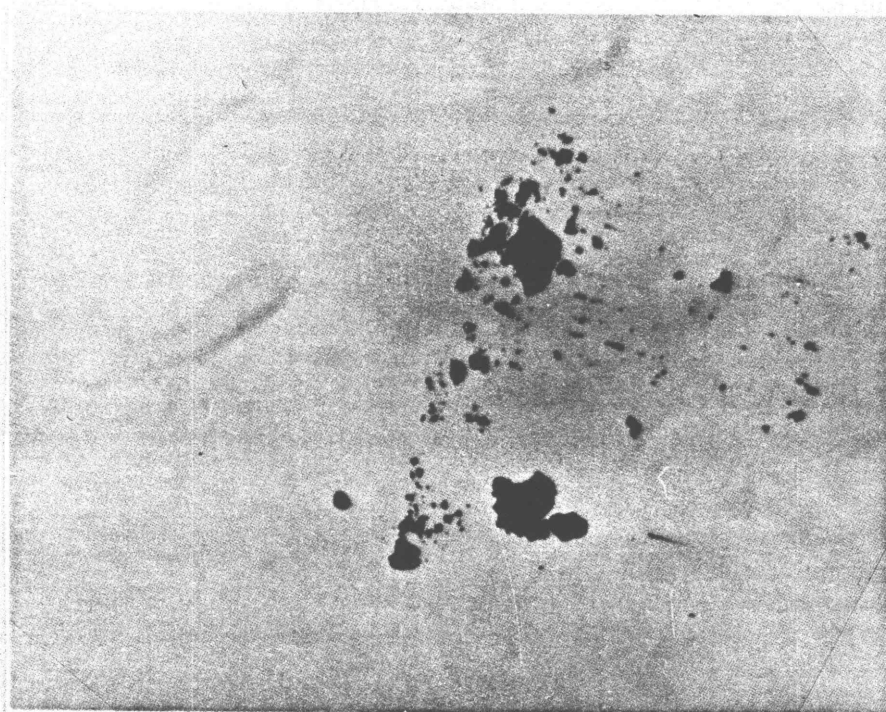


(a) 50  $\mu\text{m}$

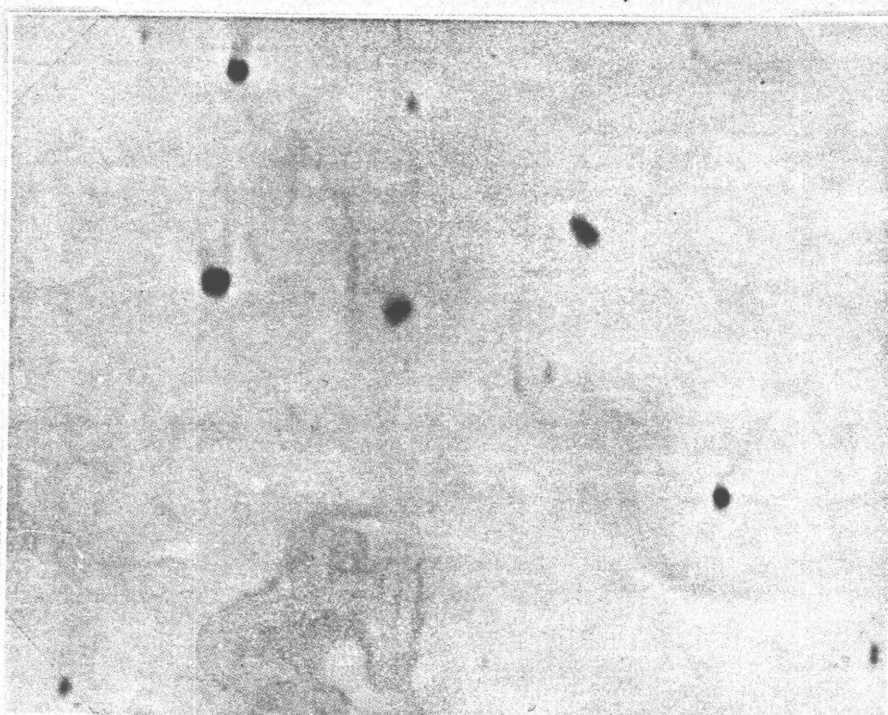


(b) 50  $\mu\text{m}$

Figure 3.4. Photomicrographs of surface morphologies depicting:

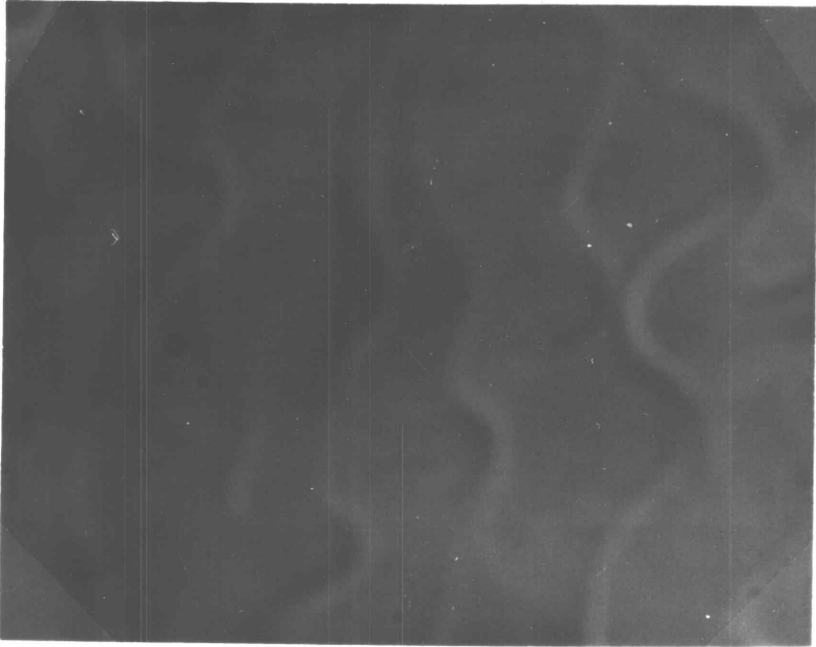


(a)  $50\ \mu\text{m}$

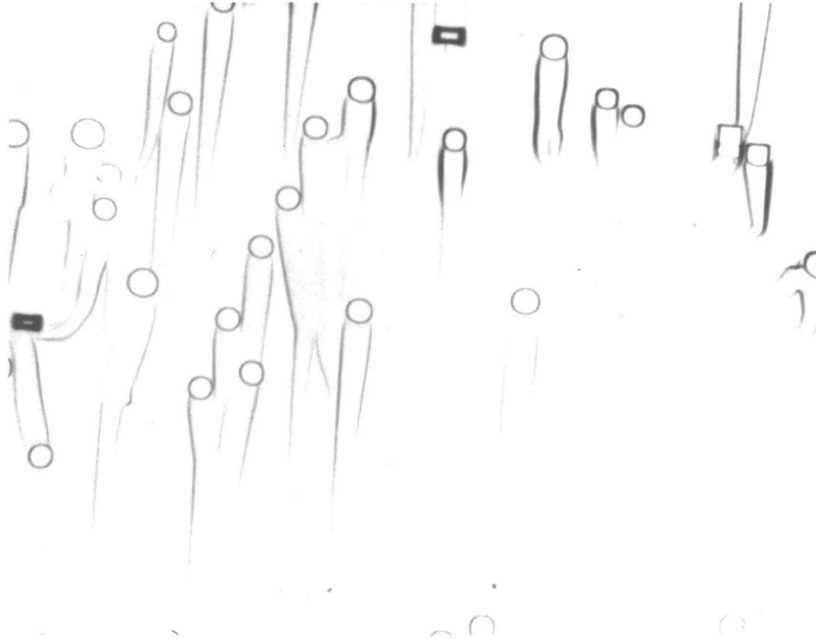


(b)  $50\ \mu\text{m}$

Figure 3.5. Photomicrographs depicting remains of polycrystalline InP on the grown epitaxial layer.



(a)  $50\ \mu\text{m}$



(b)  $50\ \mu\text{m}$

Figure 3.6. Photomicrographs of surface morphologies showing (a) ripples, and (b) etch patterns created during *in situ* etching.

observed the disappearance of the ripple morphology in InP epitaxial layers grown on exactly oriented (100) substrates. Hence the ripples observed in most of the LPE layers grown during this study are attributed to a slight misorientation of the substrates from the (100) direction.

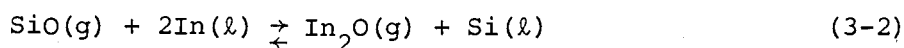
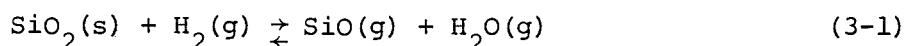
Etch patterns were observed, as shown in Fig. 3.6(b), when the *in situ* etching time was too long, viz., 15-25 sec. From this photomicrograph it is evident that the In moves and etches along a regular crystallographic direction.

### 3.5 Discussion

Heat treatment of InP at temperatures higher than 370°C readily degrades its stoichiometry. This is due to noncongruent evaporation and preferential loss of P which takes place above this temperature. Therefore, the thermal decomposition of the InP substrate prior to growth is one of the major problems in the reproducible growth of high-quality InP LPE layers<sup>(46)</sup>. The use of a graphite cover for the substrate during high growth-cell temperatures and *in situ* etching are indispensable in LPE growth of InP. It is also believed that some residual contaminants can be etched and removed during *in situ* etching.

Si and S have been identified as residual background donors<sup>(47)</sup> and C as acceptors<sup>(48)</sup> in LPE InP. The S impurities are introduced in the epitaxial layers by outdiffusion from the In and their incorporation can be reduced by prebaking the melt. Sulfur usually evaporates<sup>(23)</sup> during the prebaking period. Carbon is probably

introduced from the graphite boat. Silicon was the major unwanted background impurity in the layers grown. It was present in the In and in the polycrystalline InP used to saturate the growth solutions. The element also has a high distribution coefficient ( $\sim 30$ )<sup>(49)</sup> at typical InP LPE growth temperatures. Weiner<sup>(50)</sup> has proposed that the Si contamination results from a reaction of the reactor walls with the H<sub>2</sub> ambient during growth. The process can be described by the equations:



The above reversible equations also imply that the Si may be purged from the In-melt by water vapor. Intentional addition of purified O<sub>2</sub> has, in fact, been used to create a low background water vapor content<sup>(51)</sup>. Holmes and Kamath<sup>(47)</sup> have reported a considerable reduction in carrier concentration with addition of water vapor in the ambient.

## CHAPTER IV

PROPERTIES OF SEMI-INSULATING AND ION-IMPLANTED GaAs

The different measurements performed on semi-insulating and ion-implanted GaAs and the results obtained therefrom are presented in this chapter. The data have been analyzed and discussed in the latter half of the chapter.

4.1 Device Fabrication

The semi-insulating (SI) GaAs samples used for this study were grown either by the Liquid Encapsulation Czochralski (LEC) technique or by the horizontal Bridgman technique and were normally oriented in the (100) direction. The resistivity in the samples is  $\sim 10^7$  ohm-cm at room temperature. Vapor phase epitaxial (VPE) layers used for subsequent implantation were grown on SI GaAs:Cr substrates by the  $H_2$ -HCl-Ga-AsH<sub>3</sub> technique at Tektronix Laboratories. The undoped epitaxial layers have net electron concentration,  $n$ , ranging from  $\sim 10^{13}$  to  $\sim 10^{16}$  cm<sup>-3</sup> at 300K and thickness ranging from 3 to 7  $\mu$ m. The semi-insulating and epitaxial layers were implanted with  $^{28}Si^+$  at an energy of 100 KeV, with doses varying from  $1 \times 10^{12}$  to  $1 \times 10^{13}$  cm<sup>-2</sup>. A 4000 Å silox layer, formed by chemical vapor deposition at 420°C, was used to selectively mask regions being implanted. After implantation, the silox mask was removed and a 2000 Å silox encapsulant was deposited on the sample surface. The sample was then annealed at 800 or 850°C for 20 min. in an ambient of flowing forming gas ( $H_2:N_2 = 10:90$ ).

#### 4.1.1 Devices for Photo-Induced Current Transient Measurements

Devices were made from samples of SI GaAs  $5 \times 5 \text{ mm}^2$  in area and having a thickness of 200-300  $\mu\text{m}$ . The samples were degreased by the procedure described in Chapter III and etched for 5 - 10 sec. in  $5 \text{ H}_2\text{SO}_4 : 1 \text{ H}_2\text{O}_2 : 1 \text{ H}_2\text{O}$  at room temperature. A semitransparent circular Au film (diameter = 1.5 mm, thickness  $\approx 100\text{-}200 \text{ \AA}$ ) was deposited on the polished top surface and a thicker Au layer ( $\sim 1000 \text{ \AA}$ ) was deposited on the entire opposite face by evaporation under a vacuum of  $\sim 10^{-6}$  Torr. Similar devices were made by evaporating Cr or eutectic Au-Ge contacts, but they gave rise to low S/N ratio during the Photo-Induced Current Transient (PICT) measurements.

#### 4.1.2 Schottky Diodes on Epitaxial and Ion-Implanted Semiconductors

5000  $\text{ \AA}$  of Au-Ge (12%) followed by 500  $\text{ \AA}$  of Ni were evaporated under high vacuum to form two parallel strip contacts on the epitaxial or implanted GaAs samples. The contacts were alloyed in an ultra-high purity  $\text{N}_2$  atmosphere at a temperature of  $450^\circ\text{C}$  for 3-5 min. The samples were then etched for 5-10 sec. in  $5 \text{ H}_2\text{SO}_4 : 1 \text{ H}_2\text{O}_2 : 1 \text{ H}_2\text{O}$  at room temperature with a protective coating of wax on the ohmic contacts to remove any thin oxide layers which may have formed on the surface during alloying. Circular Au dots with  $(1\text{-}2) \times 10^{-3} \text{ cm}^2$  area and 300-500  $\text{ \AA}$  thick were then evaporated to form Schottky diodes on the epitaxial and implanted layers. Only devices which exhibited good rectifying characteristics and low reverse leakage were used for the measurements.

#### 4.1.3 GaAs Field Effect Transistors on Ion-Implanted Layers

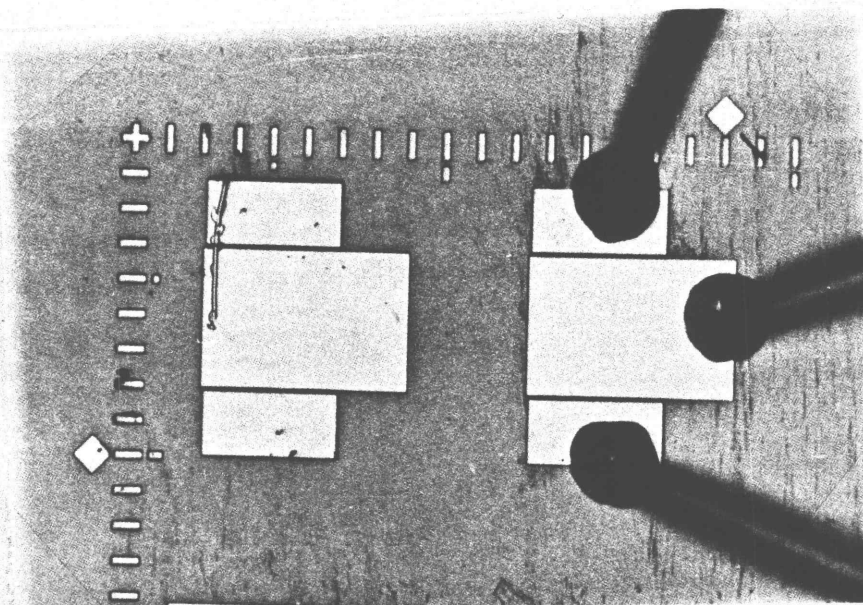
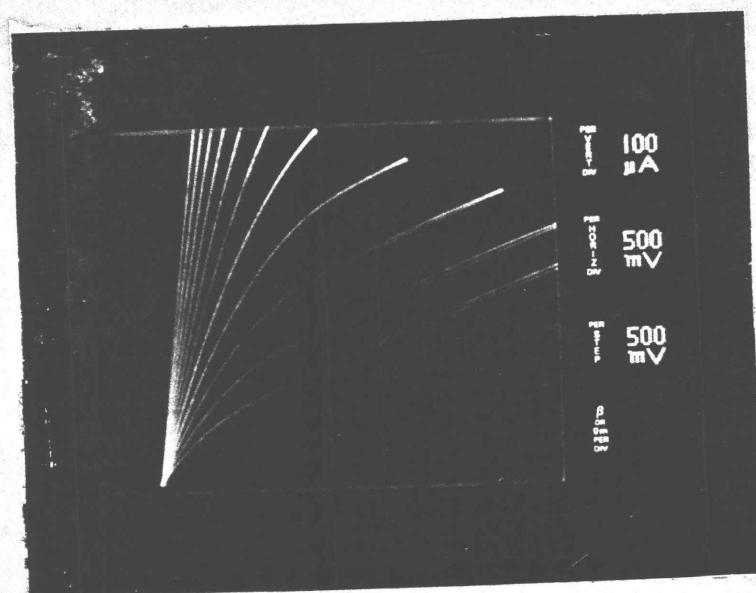
GaAs Field Effect Transistors (FETs) for transient measurements were fabricated at Tektronix Laboratories by conventional photolithography and lift-off techniques. The FETs have both gate length and width of 100  $\mu\text{m}$  and source-gate and gate-drain spacings of 5  $\mu\text{m}$ . A photomicrograph of a typical FET is shown in Fig. 4.1(a). Typical current-voltage characteristics for a FET used for subsequent measurements is shown in Fig. 4.1(b).

#### 4.1.4 Devices for Hall Effect Measurements

Symmetrical samples for Hall measurements were made by evaporating small-area ohmic contacts at the four corners and subsequent alloying.

#### 4.2 Photo-Induced Current Transient Measurements on Semi-Insulating GaAs

The Photo-Induced Current Transient (PICT) technique, first reported by Hurtes et al.<sup>(8)</sup>, has to be employed since it is not possible to perform conventional capacitance transient measurements on materials exhibiting high resistivity. The schematic of the PICT measurements is shown in Fig. 4.2. Intrinsic photoexcitation generates electron-hole pairs just underneath the circular Au film. The excess carriers are captured by electron or hole traps in the sample, if they exist. After removal of the photoexcitation, detrapping due to the thermal re-emission gives rise to a transient current between the two contacts. Typical values of the bias applied between the Au contacts varied from 8 to 10 V. Arrhenius plots for the emissions

(a) 100  $\mu\text{m}$ 

(b)

Figure 4.1. (a) a typical GaAs FET structure and (b) typical  $I_{DS} - V_{DS}$  characteristics.

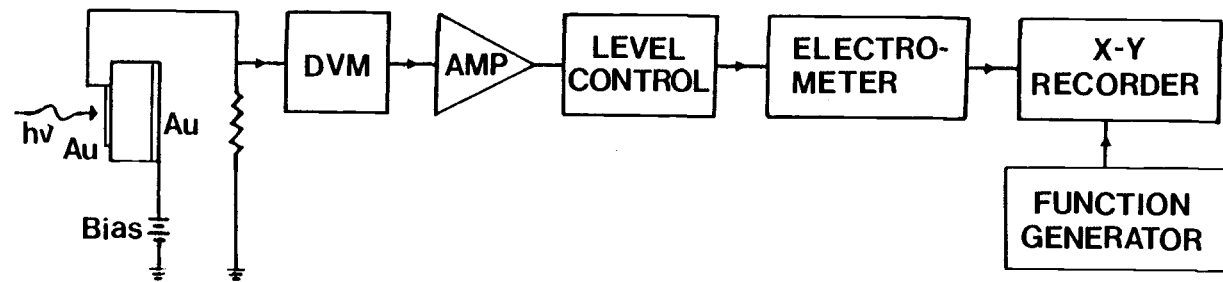


Figure 4.2. Schematic for Photo-Induced Current Transient measurements.

detected in SI GaAs:Cr and undoped GaAs are shown in Figs. 4.3 and 4.4, respectively. For experiments with intrinsic photoexcitation, the distinction between electron and hole emissions can be made by observing the direction of the transient current variation. It should be noted that the activation energies,  $\Delta E_T$ , in Tables 4.1 and 4.2 were obtained from the slopes of  $\ln(T^2\tau)$  vs.  $1/T$  plots and include the barrier energy  $\Delta E_B$ . Similarly, the capture cross sections,  $\sigma_\infty$ , were obtained from the emission rate prefactor of Eq. (2-12). The true capture cross section of the centers can be obtained from a measurement of the thermal capture rates<sup>(27)</sup>.

#### 4.3 Transient Capacitance Measurements on Ion-Implanted Semi-Insulating GaAs:Cr

Transient capacitance and photocapacitance measurement techniques were used to detect and characterize deep levels in the implanted SI GaAs:Cr and in as-grown and implanted vapor phase epitaxial (VPE) GaAs. Majority and minority carrier trap levels in the depletion region of Schottky barriers made from n-type samples can be filled by a bias or an optical pulse, respectively. The capacitance change of the diode due to thermal emissions from deep levels is monitored by a 1 MHz capacitance bridge and recorded. The activation energy and the thermal capture cross section of the various traps are determined from the measured thermal carrier emission rates at several fixed temperatures by virtue of Eqs. (2-1) and (2-2). The trap concentration,  $N_T$ , is estimated from the free carrier concentration and the capacitance change at the termination of the filling pulse by using Eq. (2-5). It may be noted that the sensitivity of

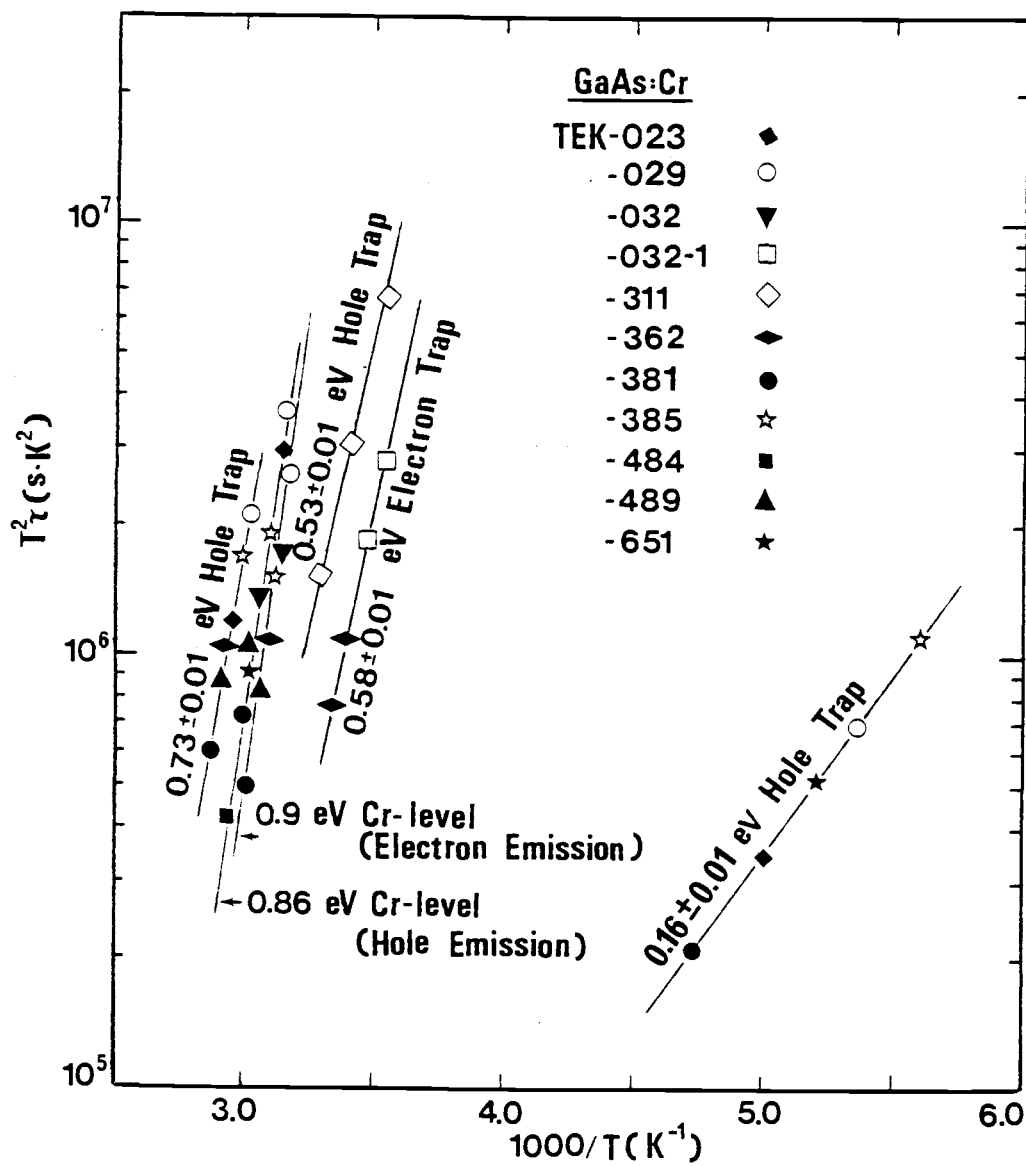


Figure 4.3. Arrhenius plots for electron and hole trap levels in SI GaAs:Cr. The symbols located arbitrarily represent the different samples and are not data points.

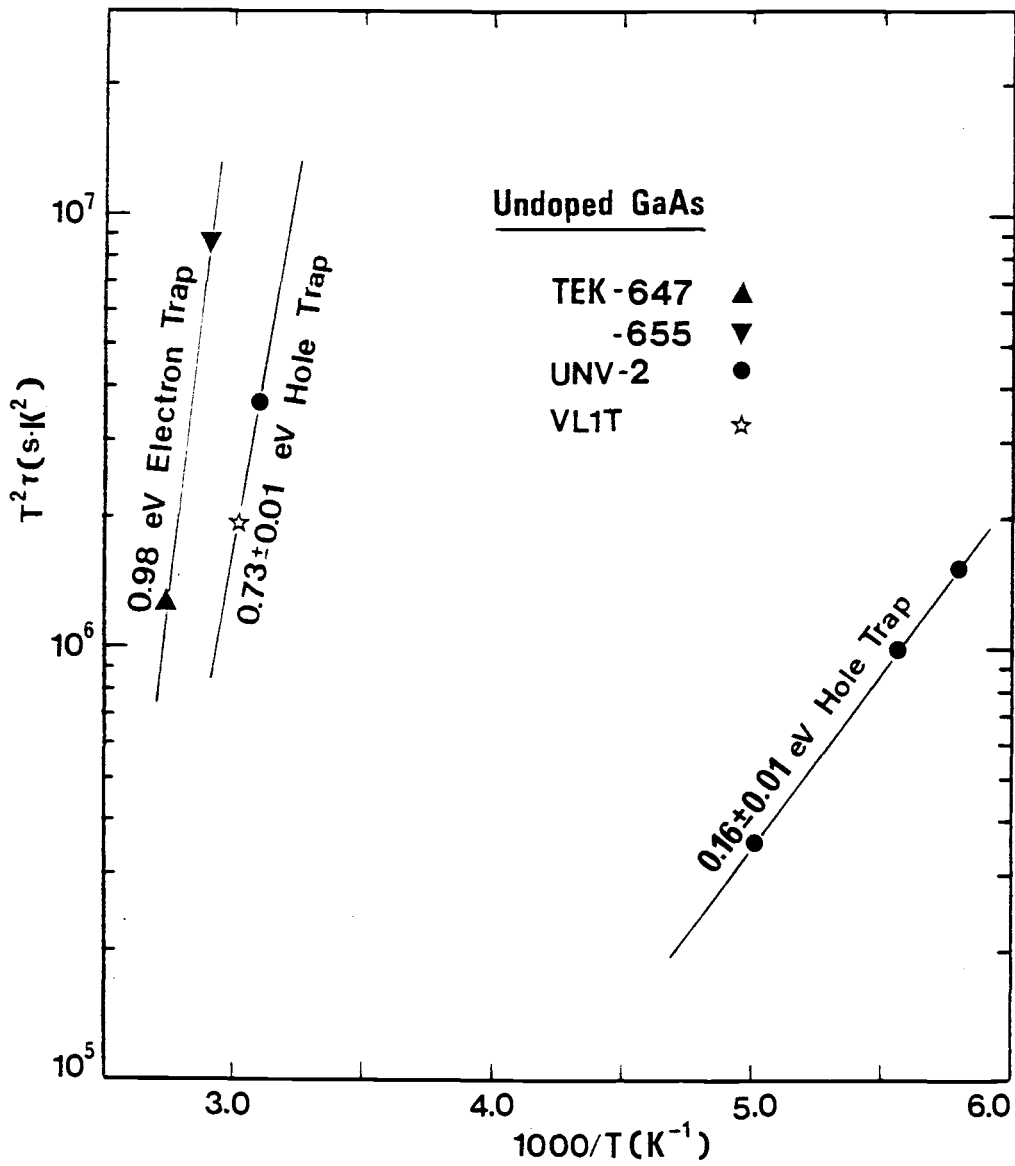


Figure 4.4. Arrhenius plots for electron and hole trap levels in SI undoped GaAs. The symbols located arbitrarily represent the different samples and are not data points.

Table 4.1. Characteristics of Deep Levels in SI GaAs:Cr.

Sample	Electron Trap		Hole Trap	
	$\Delta E_T$ (eV)	$\sigma_\infty$ (cm <sup>2</sup> )	$\Delta E_T$ (eV)	$\sigma_\infty$ (cm <sup>2</sup> )
TEK023			0.86	$1.2 \times 10^{-13}$
			0.73	$5.1 \times 10^{-17}$
			0.16	$3.9 \times 10^{-22}$
TEK029	0.90	$2.2 \times 10^{-12}$	0.87	$1.2 \times 10^{-13}$
			0.74	$5.0 \times 10^{-17}$
			0.16	$4.0 \times 10^{-22}$
TEK032	0.89	$2.1 \times 10^{-12}$	0.86	$1.1 \times 10^{-13}$
TEK0321	0.58	$4.5 \times 10^{-17}$		
TEK311			0.53	$3.2 \times 10^{-19}$
TEK 362	0.90	$2.3 \times 10^{-12}$	0.72	$5.2 \times 10^{-17}$
	0.58	$4.6 \times 10^{-17}$		
TEK381	0.91	$2.1 \times 10^{-12}$	0.85	$1.2 \times 10^{-13}$
			0.73	$5.1 \times 10^{-17}$
			0.15	$3.8 \times 10^{-22}$
TEK385	0.90	$2.2 \times 10^{-12}$	0.86	$1.2 \times 10^{-13}$
			0.73	$5.1 \times 10^{-17}$
			0.16	$3.9 \times 10^{-22}$
TEK484			0.87	$1.1 \times 10^{-13}$
TEK 489	0.90	$2.2 \times 10^{-12}$	0.86	$1.2 \times 10^{-13}$
			0.72	$5.0 \times 10^{-17}$
TEK651			0.86	$1.3 \times 10^{-13}$
			0.17	$3.9 \times 10^{-22}$

Table 4.2. Characteristics of Deep Levels in SI Undoped GaAs.

Sample	Electron Trap		Hole Trap	
	$\Delta E_T$ (eV)	$\sigma_\infty$ (cm <sup>2</sup> )	$\Delta E_T$ (eV)	$\sigma_\infty$ (cm <sup>2</sup> )
TEK657	0.98	$1.6 \times 10^{-13}$		
TEK655	0.97	$1.5 \times 10^{-13}$		
UNV2			0.73	$5.1 \times 10^{-17}$
			0.16	$3.9 \times 10^{-22}$
VL1T			0.74	$5.0 \times 10^{-17}$

the measurements, which is primarily determined by the noise added to the transient signal, sets the detection limit for traps. It was estimated that traps with concentration  $10^{-4}$  times lower than the free carrier concentration in the sample would not be detected.

The characteristics of electron and hole trap levels detected in the implanted and annealed SI GaAs samples with different implanted doses are listed in Table 4.3. These results are representative of over 30 samples characterized in this study. The electron trap levels with  $\Delta E_T = 0.17 \pm 0.01$  and  $0.21 \pm 0.01$  eV do not appear consistently and are ascribed to unknown impurities and/or defects. Chromium is observed to be present, as evidenced by the  $0.85 \pm 0.01$  eV hole emission. The electron trap level with  $\Delta E_T = 0.52 \pm 0.01$  eV and the hole trap level with  $\Delta E_T = 0.15 \pm 0.01$  eV were consistently detected in the implanted and annealed SI GaAs:Cr samples. Neither level was detected in sample B14. This may be due to the fact that the concentration of the traps in the sample was below the detection limit of the measurements.

#### 4.4 Transient Measurements on GaAs Field Effect Transistors

A suitable quiescent reverse bias is applied to the Schottky gate of the FETs so that near-pinch-off condition exists in the channel. An injection pulse is applied to the gate for the detection of majority carrier traps. Variations of depletion region with the injection pulse is illustrated schematically in Fig. 4.5. During the injection pulse, trap levels formerly within the depletion region are filled with electrons. As the trapped electron population returns

Table 4.3. Characteristics of Deep Levels in Si-Implanted and Annealed SI GaAs:Cr. Thermal Annealing of all Samples was Done at 800°C for 20 min. in Flowing Forming Gas.

Sample	Implant Dose ( $10^{12} \text{ cm}^{-2}$ )	Electron Trap		Hole Trap	
		$\Delta E_T$ (eV)	$\sigma_\infty$ ( $\text{cm}^2$ )	$\Delta E_T$ (eV)	$\sigma_\infty$ ( $\text{cm}^2$ )
C 41	1.0	0.53	$1.3 \times 10^{-18}$	0.84	$1.4 \times 10^{-13}$
		0.21	$3.1 \times 10^{-21}$	0.16	$5.8 \times 10^{-23}$
B 36	2.0	0.51	$1.5 \times 10^{-18}$	0.85	$1.3 \times 10^{-13}$
		0.17	$5.3 \times 10^{-23}$	0.15	$5.9 \times 10^{-23}$
C 31	2.0	0.51	$1.6 \times 10^{-18}$	0.84	$1.4 \times 10^{-13}$
		0.17	$5.3 \times 10^{-23}$	0.14	$6.0 \times 10^{-23}$
B 26	4.0	0.52	$1.4 \times 10^{-18}$	0.86	$1.2 \times 10^{-13}$
		0.16	$5.5 \times 10^{-23}$	0.14	$6.0 \times 10^{-23}$
C 21	4.0	0.52	$1.4 \times 10^{-18}$	0.86	$1.2 \times 10^{-13}$
		0.18	$5.2 \times 10^{-23}$	0.15	$5.9 \times 10^{-23}$
B 14	8.0	-	-	0.86	$1.2 \times 10^{-13}$
S 45	10.0	0.53	$1.3 \times 10^{-18}$	0.85	$1.3 \times 10^{-13}$
				0.15	$6.0 \times 10^{-23}$

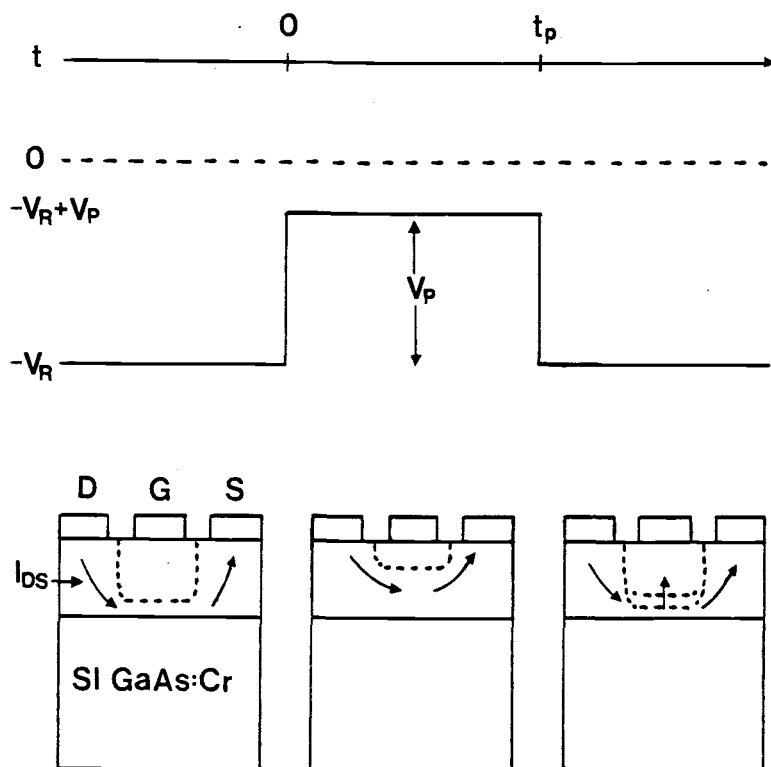


Figure 4.5. Pulse sequence and channel depletion-region behavior during direct trap measurements on GaAs FETs.

to equilibrium by thermal emission, the drain-source current,  $I_{DS}$ , also returns to its quiescent value. Photoexcitation was used to alter the population of minority carrier traps. Similar measurements have been performed on Si-implanted GaAs FETs by Simons and King<sup>(52)</sup>.

The capacitance transient results described in the previous section were corroborated by the transient measurements on GaAs FETs fabricated by ion-implantation technology. Values of  $\Delta E_T$  and  $\sigma_\infty$  for various electron and hole emissions observed in the channel of the GaAs FETs are listed in Table 4.4. The  $0.52 \pm 0.01$  and  $0.15 \pm 0.01$  eV electron and hole trap levels, respectively, are again observed consistently. The 0.15 eV hole trap level is probably present in the channel of FET18 also, but its concentration is below the detection limit. Hole emission from the Cr center is also observed.

#### 4.5 Transient Capacitance Measurements on Vapor Phase Epitaxial GaAs

The Arrhenius plots of different traps detected in the various as-grown VPE GaAs samples are depicted in Fig. 4.6. The electron trap with an activation energy of 0.83 eV is a dominant deep level in VPE and bulk GaAs. It has been shown to be associated with a native defect<sup>(53)</sup>. The  $0.37 \pm 0.01$  eV electron trap level detected in some samples has been observed in  $\text{AsCl}_3$  VPE and organometallic VPE GaAs<sup>(53)</sup>. A hole trap level with  $\Delta E_T = 0.85 \pm 0.01$  eV is detected in some samples upon photoexcitation. The measured concentration of the level is characteristically small. This hole trap level has not been observed in the rest of the as-grown VPE GaAs samples. The characteristics of traps detected in the various as-

Table 4.4 Characteristics of Deep Levels in GaAs FETs  
Fabricated by Ion-Implantation Technology.

Sample	Implant Dose ( $10^{12}$ cm $^{-2}$ )	Electron Trap		Hole Trap	
		$\Delta E_T$ (eV)	$\sigma_\infty$ (cm $^2$ )	$\Delta E_T$ (eV)	$\sigma_\infty$ (cm $^2$ )
FET 8	2.0	0.52	$1.4 \times 10^{-18}$	0.84 0.15	$1.4 \times 10^{-13}$ $5.9 \times 10^{-23}$
FET 15	3.0	0.51	$1.5 \times 10^{-18}$	0.86 0.14	$1.2 \times 10^{-13}$ $6.0 \times 10^{-23}$
FET 16	3.0	0.52	$1.4 \times 10^{-18}$	0.85 0.16	$1.3 \times 10^{-13}$ $5.8 \times 10^{-23}$
FET 18	4.0	0.53	$1.4 \times 10^{-18}$	0.85 -	$1.3 \times 10^{-13}$ -
FET 20	4.0	0.53	$1.2 \times 10^{-18}$	0.86 0.15	$1.2 \times 10^{-13}$ $5.9 \times 10^{-23}$

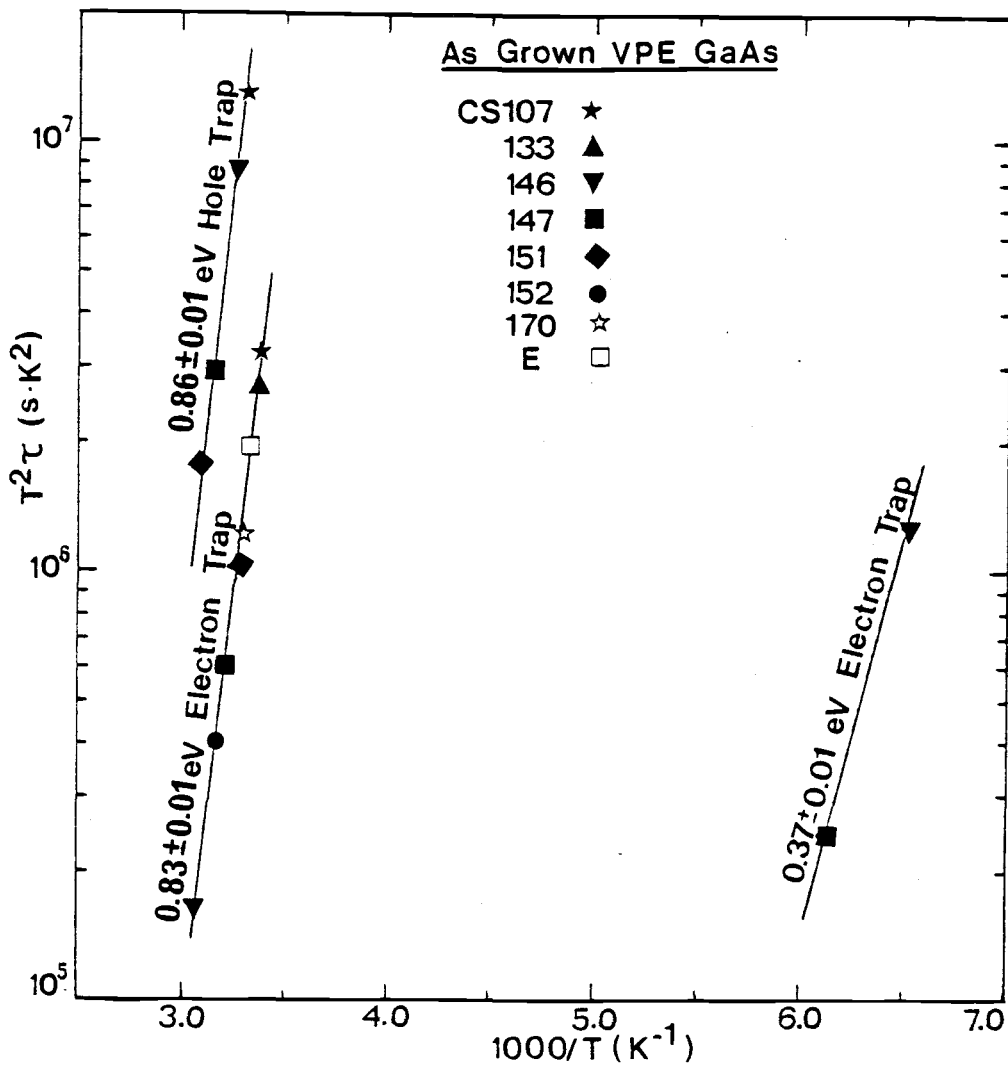


Figure 4.6. Arrhenius plots for electron and hole trap levels in as-grown VPE GaAs. The symbols located arbitrarily represent the different samples and are not data points.

grown VPE GaAs samples are listed in Table 4.5.

#### 4.6 Transient Capacitance Measurements on Ion-Implanted Vapor Phase Epitaxial GaAs

The Arrhenius plots of traps detected in implanted VPE GaAs are shown in Fig. 4.7. Several distinct features may be noted. The 0.86 eV hole trap level is now observed more consistently and with a larger concentration. Another hole trap with a thermal activation energy of 0.15 eV is detected consistently. The two electron trap levels present in the as-grown materials are no longer observed in this material; instead, an electron trap level with an activation energy of 0.53 eV is observed. A barrier energy  $\Delta E_B = 0.33 \text{ eV}^{(21)}$  was determined for this trap from electron capture rate measurements. Thus the enthalpy of the level is 0.20 eV; however, in order to avoid any confusion, the level will be referred to as the 0.53 eV electron trap. The characteristics of traps detected in two VPE samples after implant and anneal are listed in Table 4.6.

#### 4.7 Transport Measurements

##### 4.7.1 Semi-Insulating GaAs

The variations of Hall electron mobility with temperature in the range 380-600K for semi-insulating Cr-doped and undoped GaAs are depicted in Fig. 4.8(a) and (b), respectively. The variations of  $R_H T^{3/2}$ ,  $(\sigma R_H)^{-1}$  and dark conductivity,  $\sigma$ , with inverse temperature are shown in Figs. 4.9 to 4.11(a) and (b) for SI GaAs:Cr and undoped GaAs, respectively. The variations are almost linear in the temperature range of interest. The measured transport parameters

Table 4.5. Electrical Characteristics of As-Grown VPE GaAs.

Sample	$\mu_{\text{electron}}$ ( $\text{cm}^2/\text{V.s}$ )		n at 300K ( $\text{cm}^{-3}$ )	Total <sup>a)</sup> Ionized Impurity $N_A + N_D$ ( $\text{cm}^{-3}$ )	Electron Traps			Hole Traps		
	300K	80K			$\Delta E_T$ (eV)	$N_T$ ( $\text{cm}^{-3}$ )	$\sigma_{\infty}$ ( $\text{cm}^2$ )	$\Delta E_T$ (eV)	$N_T$ ( $\text{cm}^{-3}$ )	$\sigma_{\infty}$ ( $\text{cm}^2$ )
	CS151	-			-	$1.6 \times 10^{15}$	-	0.83	$1.0 \times 10^{13}$	$2.0 \times 10^{-14}$
CS146	-	-	$1.0 \times 10^{14}$	-	0.83	$2.2 \times 10^{13}$	$1.2 \times 10^{-14}$	0.84	$2.0 \times 10^{13}$	$1.2 \times 10^{-13}$
CS147	-	-	$1.4 \times 10^{15}$	-	0.83 0.36	$1.3 \times 10^{13}$ $5.1 \times 10^{13}$	$1.2 \times 10^{-14}$ $1.0 \times 10^{-14}$	0.86	$3.2 \times 10^{12}$	$1.2 \times 10^{-13}$
CS107	6,320	40,000	$5.0 \times 10^{13}$	$3.6 \times 10^{15}$	0.83	$1.2 \times 10^{13}$	$4.0 \times 10^{-14}$	0.86	$5.3 \times 10^{11}$	$1.2 \times 10^{-13}$
CS152	7,056	70,000	$2.1 \times 10^{15}$	$2.4 \times 10^{15}$	0.83 0.38	$6.7 \times 10^{14}$ $7.2 \times 10^{12}$	$2.0 \times 10^{-14}$ $1.0 \times 10^{-14}$	-	-	-
E	3,516	6,000	$8.7 \times 10^{16}$	$1.4 \times 10^{17}$	0.83	$1.7 \times 10^{14}$	$2.0 \times 10^{-14}$	-	-	-
CS133	6,935	45,000	$4.0 \times 10^{15}$	$6.0 \times 10^{15}$	0.83	$1.8 \times 10^{14}$	$1.2 \times 10^{-14}$	-	-	-
CS170	5,000	45,000	$2.5 \times 10^{15}$	-	0.83	$0.9 \times 10^{14}$	$1.5 \times 10^{-14}$	-	-	-

a) From analysis of Hall-effect data.

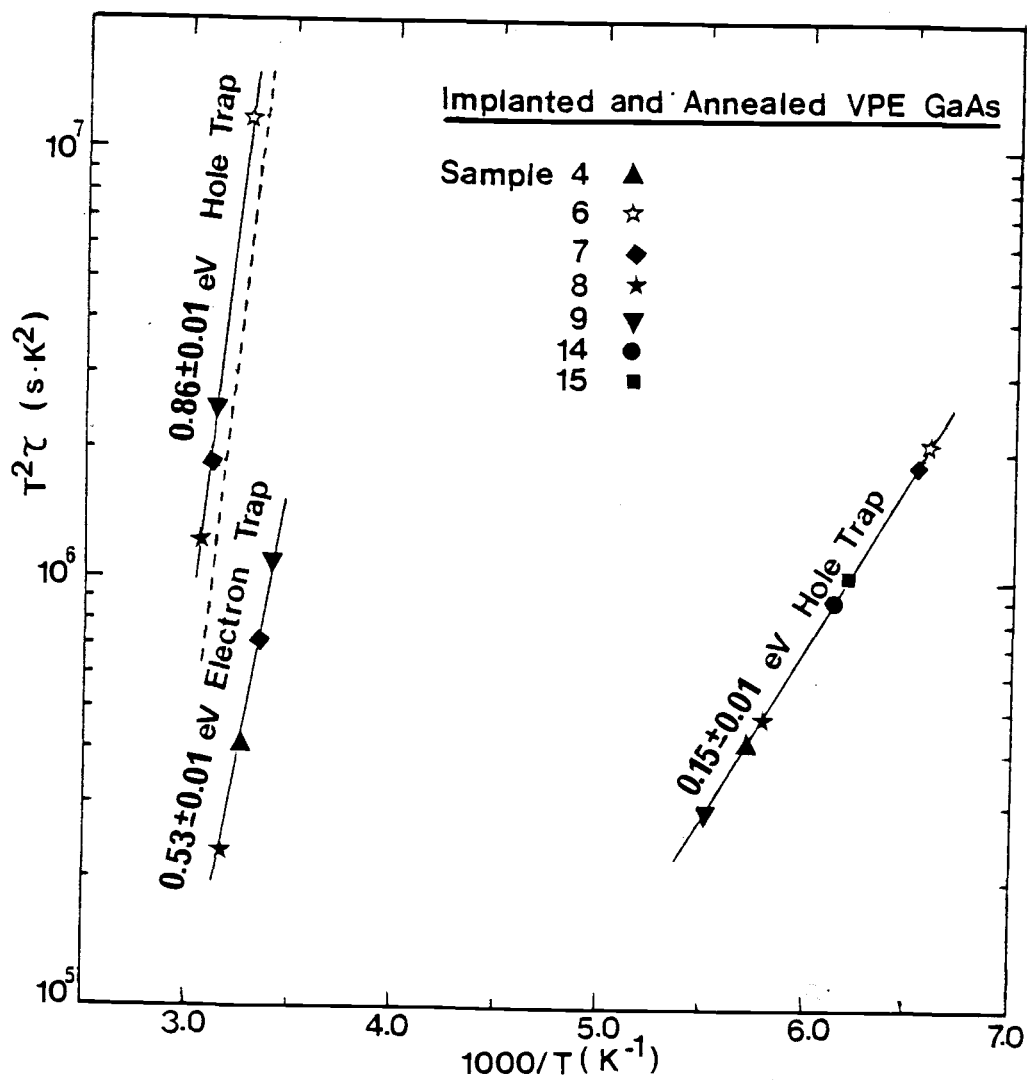


Figure 4.7. Arrhenius plots for electron and hole trap levels in Si-implanted and annealed VPE GaAs. The symbols located arbitrarily represent the different samples and are not data points. The dashed line represents electron emission from the Cr-center.

Table 4.6. Electrical Characteristics of Implanted and Annealed VPE GaAs.

VPE Sample	Implanted Sample No.	Implant Dose (cm <sup>-2</sup> )	$\mu$ electron (cm <sup>2</sup> /V.s)		$n_s$ at 300K (cm <sup>-2</sup> )	Electron Traps			Hole Traps		
			300K	80K		$\Delta E_T$ (eV)	$N_T$ (cm <sup>-3</sup> )	$\sigma_\infty$ (cm <sup>2</sup> )	$\Delta E_T$ (eV)	$N_T$ (cm <sup>-3</sup> )	$\sigma_\infty$ (cm <sup>2</sup> )
CS133 <sup>a)</sup>	6 <sup>c)</sup>	$5 \times 10^{12}$	4,303	6,254	$2.7 \times 10^{12}$	-	-	-	0.86 0.15	$3.0 \times 10^{15}$ $1.7 \times 10^{15}$	$1.2 \times 10^{-13}$ $5.9 \times 10^{-23}$
	9 <sup>c)</sup>	$5 \times 10^{12}$	4,237	6,348	$2.7 \times 10^{12}$	0.53	$4.9 \times 10^{16}$	$7.0 \times 10^{-18}$	0.86 0.15	$3.7 \times 10^{15}$ $2.0 \times 10^{16}$	$1.2 \times 10^{-13}$ $5.1 \times 10^{-23}$
	8	$5 \times 10^{12}$	4,152	-	$2.7 \times 10^{12}$	0.53	$4.8 \times 10^{15}$	$7.0 \times 10^{-18}$	0.86 0.15	$1.2 \times 10^{16}$ $1.0 \times 10^{17}$	$1.2 \times 10^{-13}$ $5.9 \times 10^{-23}$
	4	$8 \times 10^{12}$	3,863	-	$4.7 \times 10^{12}$	0.53	$3.6 \times 10^{15}$	$7.0 \times 10^{-18}$	0.15	$3.0 \times 10^{16}$	$5.9 \times 10^{-23}$
	7	$8 \times 10^{12}$	3,683	-	$4.7 \times 10^{12}$	0.53	$1.6 \times 10^{16}$	$7.0 \times 10^{-18}$	0.86 0.15	$4.7 \times 10^{15}$ $4.3 \times 10^{16}$	$1.2 \times 10^{-13}$ $5.9 \times 10^{-23}$
CS152 <sup>a)</sup>	14	$1 \times 10^{13}$	1,424	-	$1.5 \times 10^{13}$	-	-	-	0.15	$2.6 \times 10^{16}$	$5.9 \times 10^{-23}$
	15 <sup>c)</sup>	$1 \times 10^{13}$ <sup>b)</sup>	2,491	3,370	$1.2 \times 10^{13}$	-	-	-	0.15	$2.4 \times 10^{16}$	$5.9 \times 10^{-23}$

a) Samples implanted with 100 keV <sup>28</sup>Si<sup>+</sup> and annealed at 800°C for 20 min. with 2000 Å/420°C silox.

b) Annealing at 850°C, other conditions remaining the same.

c) Ionized impurity density ( $N_A + N_D$ ) =  $1.4 \times 10^{17}$ ,  $1.4 \times 10^{17}$ , and  $1.4 \times 10^{18}$  cm<sup>-3</sup> for samples 6, 9 and 15, respectively from analysis of Hall-effect data.

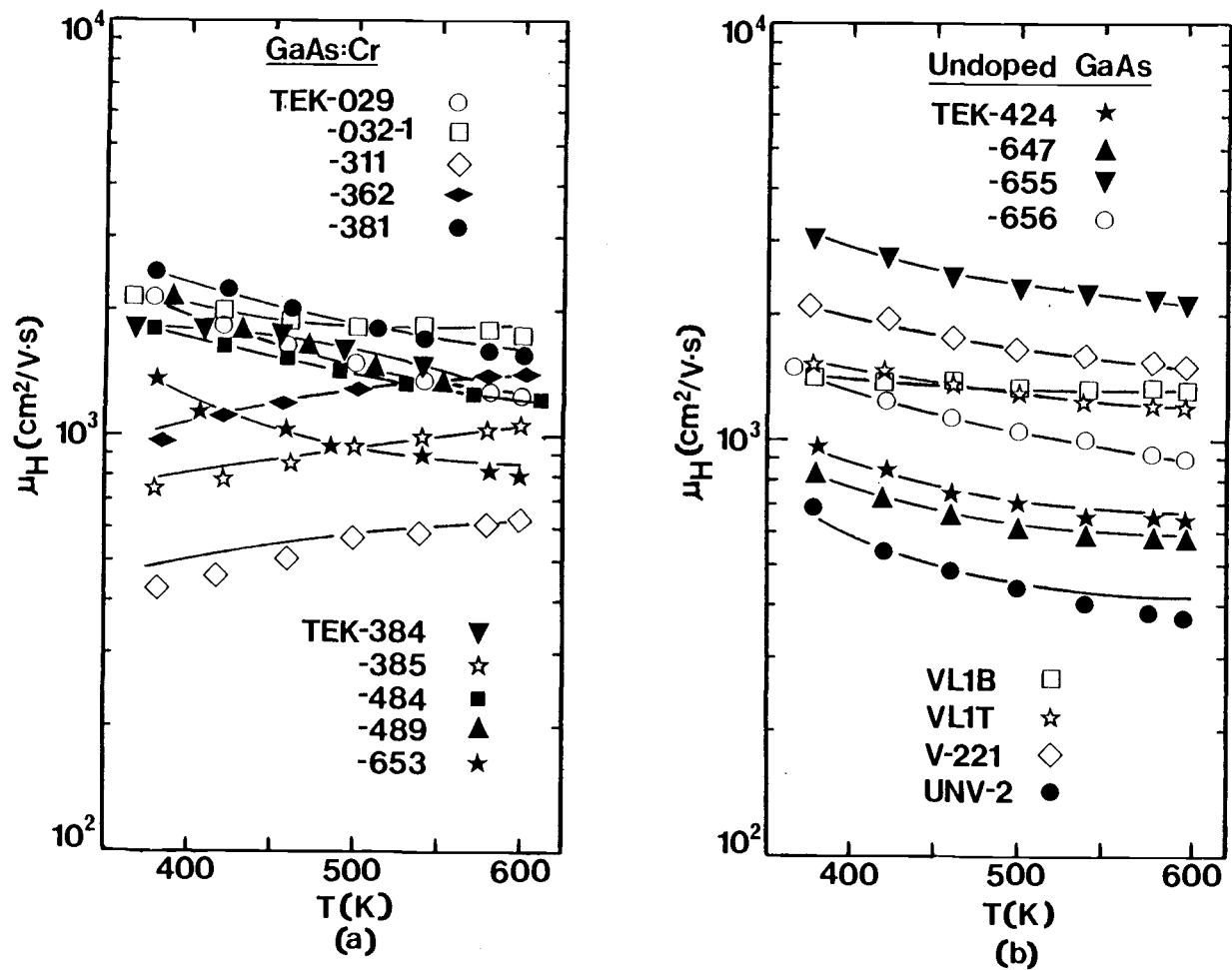


Figure 4.8. Variation of Hall mobility with temperature in (a) SI GaAs:Cr and (b) SI undoped GaAs.

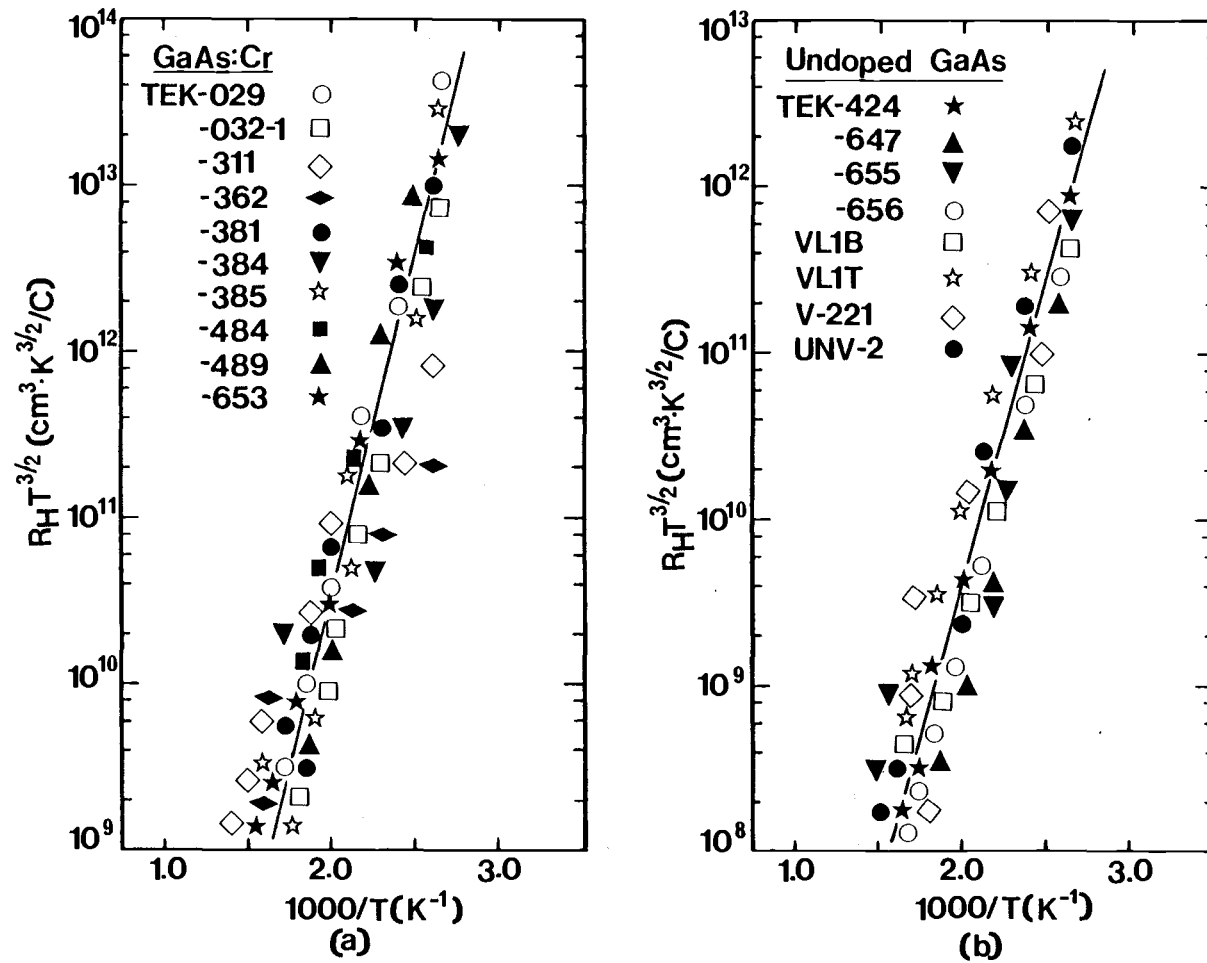


Figure 4.9. Plots of  $R_H T^{3/2}$  versus inverse temperature in (a) SI GaAs:Cr and (b) SI undoped GaAs.

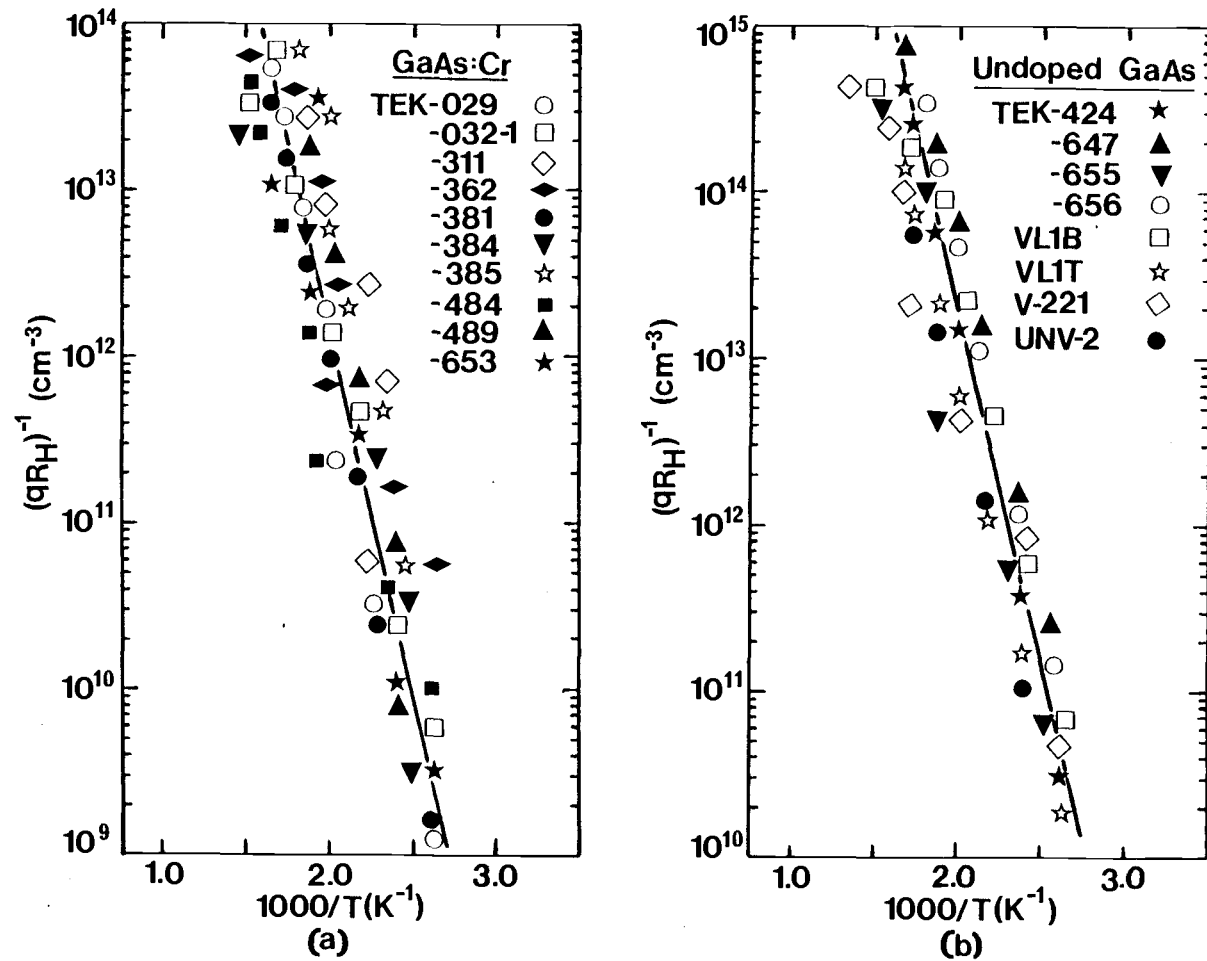


Figure 4.10. Plots of  $(qR_H)^{-1}$  versus inverse temperature in (a) SI GaAs:Cr and (b) SI undoped GaAs.

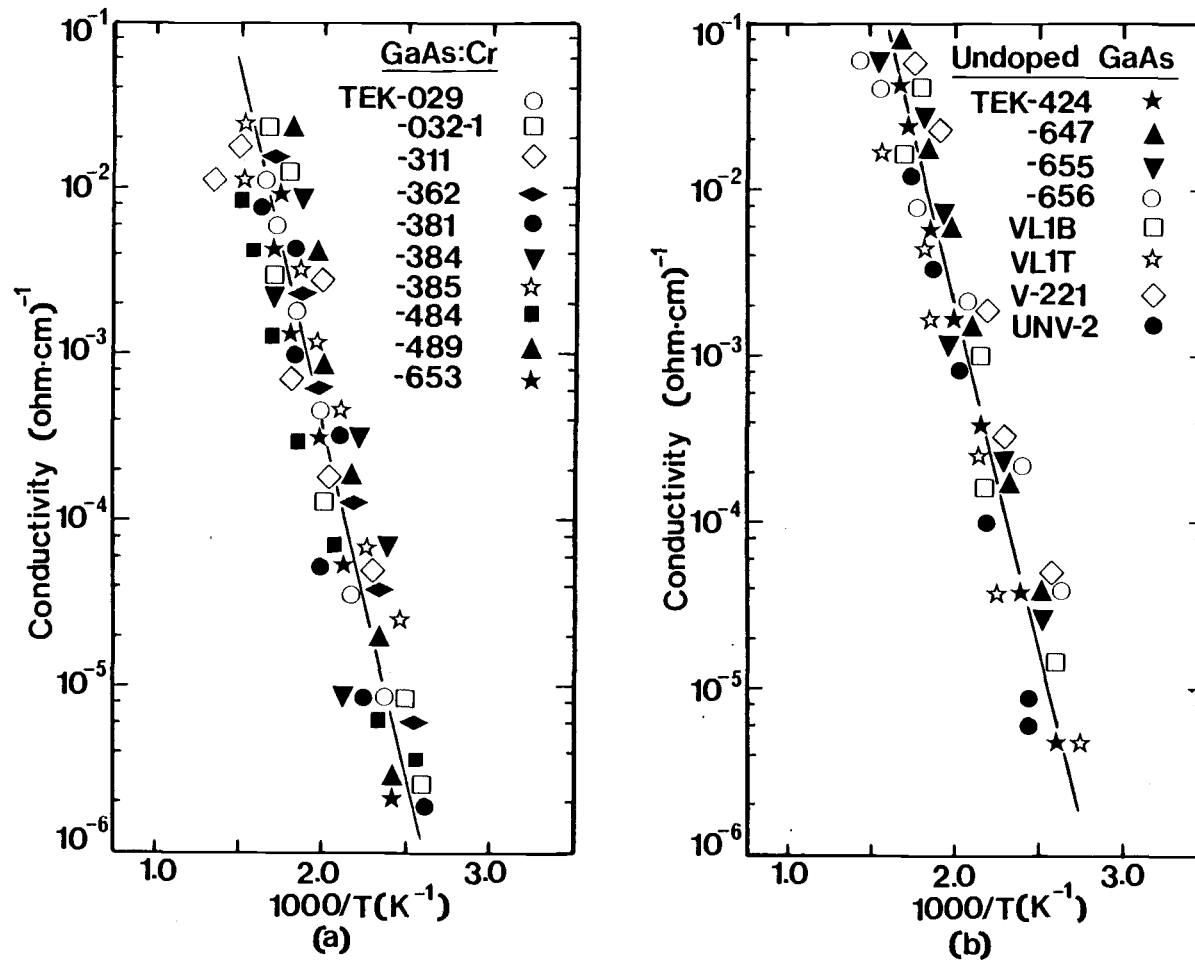


Figure 4.11. Plots of dark conductivity,  $\sigma$ , versus inverse temperature in (a) SI GaAs:Cr and (b) SI undoped GaAs.

at 400K in SI GaAs:Cr and undoped GaAs are listed in Tables 4.7 and 4.8, respectively.

#### 4.7.2 Ion-Implanted GaAs

Provisions were made for illuminating the sample with monochromatic light. Due to the uncertainty in the active layer thickness of the implanted samples, only the surface carrier concentration in these samples could be evaluated.

Variation of the Hall electron mobility,  $\mu_H$ , with temperature in the range 80-550K for as-grown and implanted VPE GaAs samples are shown in Figs. 4.12, 4.13 and 4.14. The noticeable feature is the significant decrease in mobility upon implanting the VPE GaAs samples. A similar decrease is noticed in the mobility variation of as-grown sample E, in which  $n(\approx 8.7 \times 10^{16} \text{ cm}^{-3})$  is significantly higher than for the other as-grown VPE GaAs samples. Values of the mobility,  $\mu_H$ , at 300K and 80K are also listed in Tables 4.5 and 4.6. The Hall electron mobility at 300K in the implanted and annealed SI GaAs:Cr samples varied from 1778-3900  $\text{cm}^2/\text{V}\cdot\text{s}$  depending on the implant dose. Typical variations of the Hall carrier concentration,  $n_H$ , in the as-grown VPE GaAs samples and the surface carrier concentration,  $n_s$ , in the implanted VPE GaAs samples are depicted in Fig. 4.15(a) and (b), respectively. The slight increase in the value of  $n_H$  with decrease in temperature in the case of as-grown VPE sample CS152 is an anomalous effect and is probably due to a change in the value of the scattering factor, which has been assumed to be unity. The mobility data listed in Table 4.6 indicates that  $\mu_H$  decreases with increase in

Table 4.7. Transport Data in SI GaAs:Cr Obtained from Hall Measurements. Also Listed are the Values of the Fermi Energy at 400K and Energy Position of the Deep Acceptor Levels Derived from Analysis of Hall-Effect Data.

Sample	$(qR_H)^{-1}$ at 400K ( $\text{cm}^{-3}$ )	$\mu_H$ at 400K ( $\text{cm}^2/\text{V.s}$ )	Slope of $\ln(R_H T^{3/2})^{-1}$ (eV)	$(E_G - E_{AA})$ From Analysis (eV)	$(E_G - E_F)$ at 400K From Analysis (eV)
TEK 029	$5.8 \times 10^9$	2020	0.82	0.81	0.64
TEK 0321	$1.7 \times 10^{10}$	2100	0.84	0.83	0.60
TEK 311	$2.0 \times 10^{11}$	275	0.65	0.83	0.52
TEK 362	$4.0 \times 10^{10}$	790	0.66	0.83	0.57
TEK 381	$7.2 \times 10^9$	2450	0.80	0.81	0.63
TEK 384	$1.0 \times 10^{10}$	1880	0.80	0.82	0.62
TEK 385	$6.0 \times 10^{11}$	560	0.85	0.84	0.48
TEK 484	$1.7 \times 10^{10}$	1770	0.81	0.82	0.60
TEK 489	$2.8 \times 10^{10}$	1950	0.86	0.83	0.58
TEK 653	$1.1 \times 10^{10}$	1250	0.87	0.83	0.62

Table 4.8. Transport Data in SI Undoped GaAs Obtained from Hall Measurements. Also Listed are the Values of Fermi Energy at 400K and Energy Position of the Deep Donor Levels Derived from Analysis of Hall-Effect Data.

Sample	$(qR_H)^{-1}$ at 400K ( $\text{cm}^{-3}$ )	$\mu_H$ at 400K ( $\text{cm}^2/\text{V.s}$ )	Slope of $\ln(R_H T^{3/2})^{-1}$ (eV)	$(E_G - E_{DD})$ From Analysis (eV)	$(E_G - E_F)$ at 400K From Analysis (eV)
TEK 424	$1.25 \times 10^{11}$	890	0.75	0.74	0.53
TEK 647	$7.8 \times 10^{11}$	780	0.67	0.72	0.47
TEK 655	$2.3 \times 10^{11}$	2950	0.71	0.72	0.51
TEK 656	$4.2 \times 10^{11}$	1350	0.68	0.73	0.49
UNV2	$3.2 \times 10^{10}$	600	0.77	0.75	0.58
VL1B	$1.9 \times 10^{11}$	1425	0.65	0.71	0.52
VL1T	$7.5 \times 10^{10}$	1475	0.74	0.74	0.55
V221	$1.85 \times 10^{11}$	2075	0.71	0.72	0.52

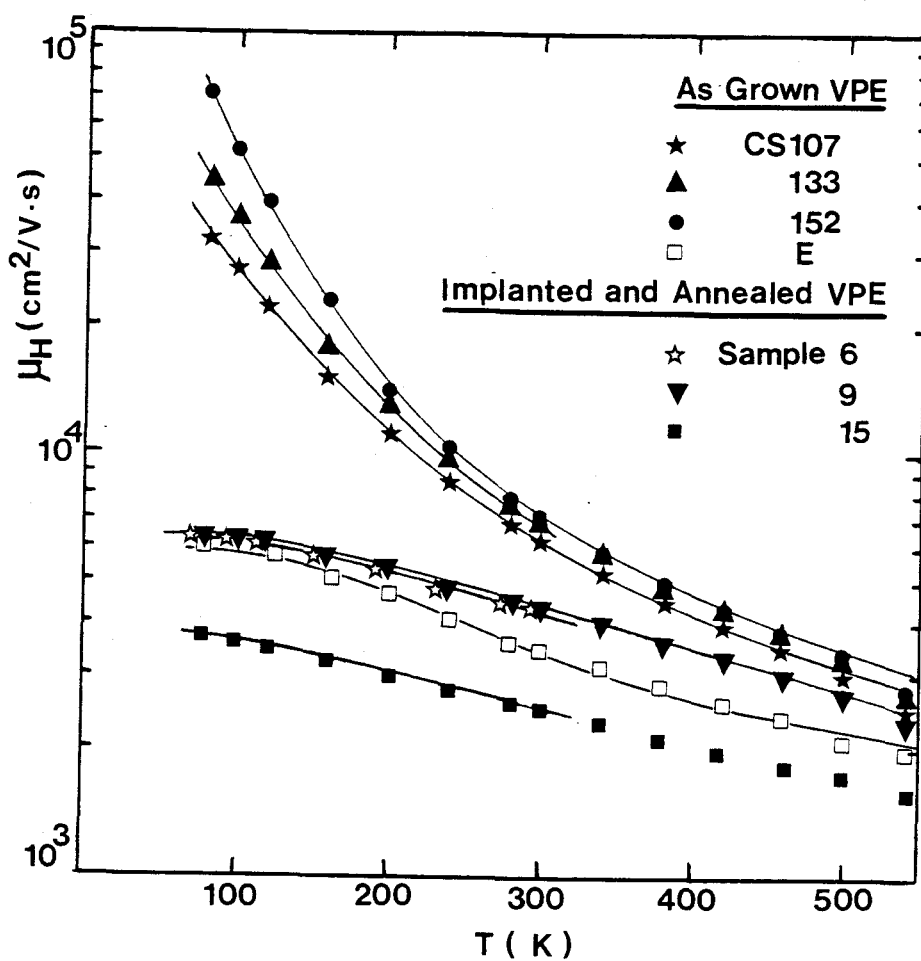


Figure 4.12. Variation of Hall electron mobility with temperature in as-grown and implanted VPE GaAs. The solid curves for  $80 \leq T \leq 300\text{K}$  in all the samples and for  $T > 300\text{K}$  in samples CS107, CS152, E and 9 represent theoretically calculated mobilities.

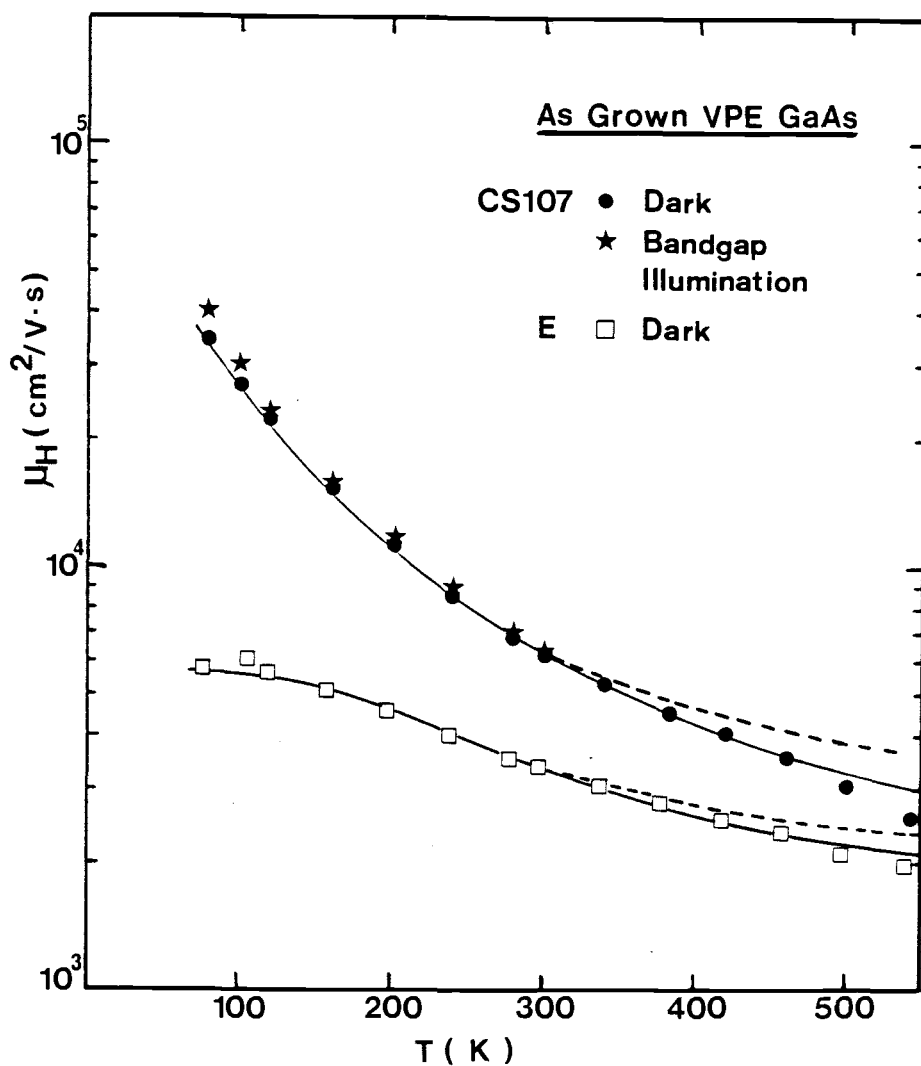


Figure 4.13. Variation of electron mobility with temperature in as-grown samples E and CS107. The dashed and solid curves for  $T > 300\text{K}$  represent theoretically calculated mobilities with and without the inclusion of space-charge scattering, respectively.

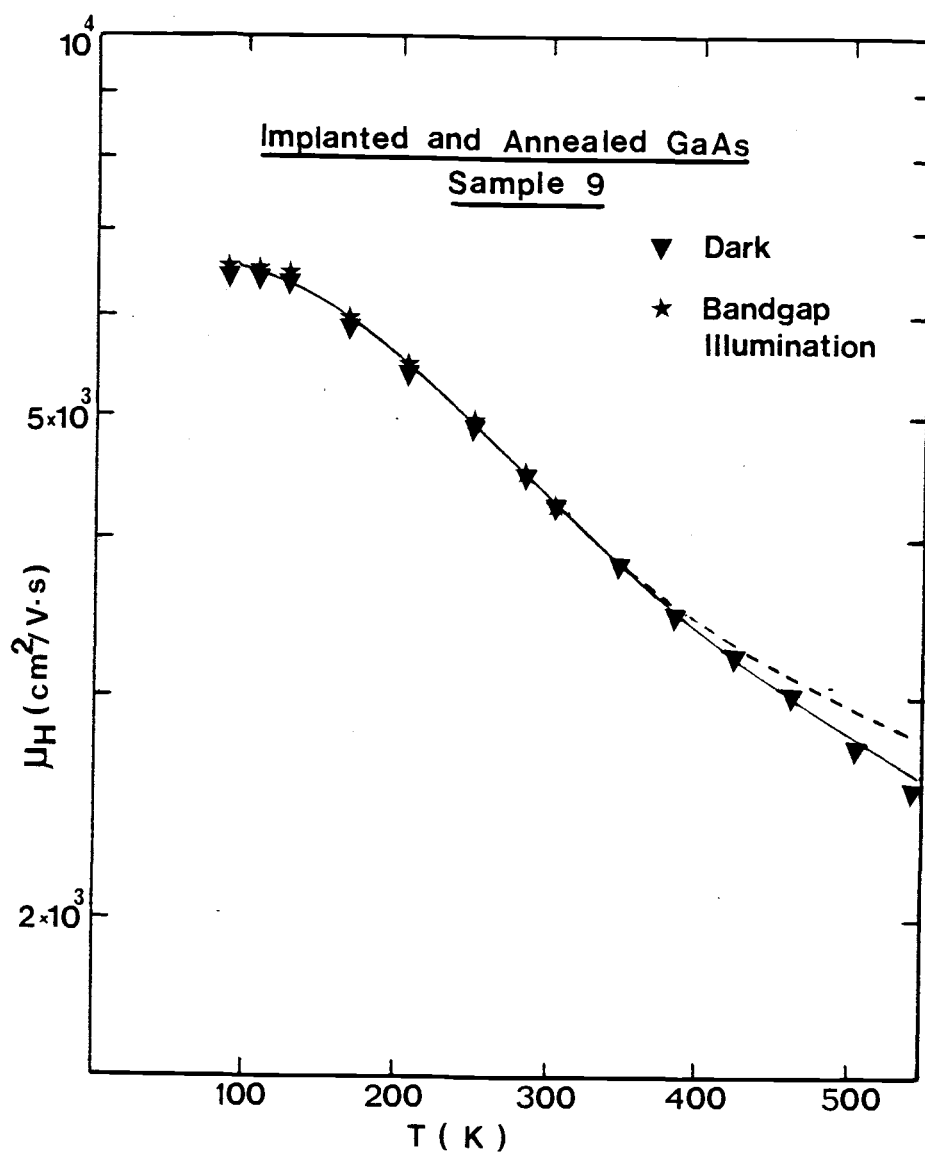


Figure 4.14. Electron mobility variation with temperature in implanted and annealed sample 9. The dashed and solid curves for  $T > 300\text{K}$  represent theoretically calculated mobilities with and without the inclusion of space-charge scattering, respectively.

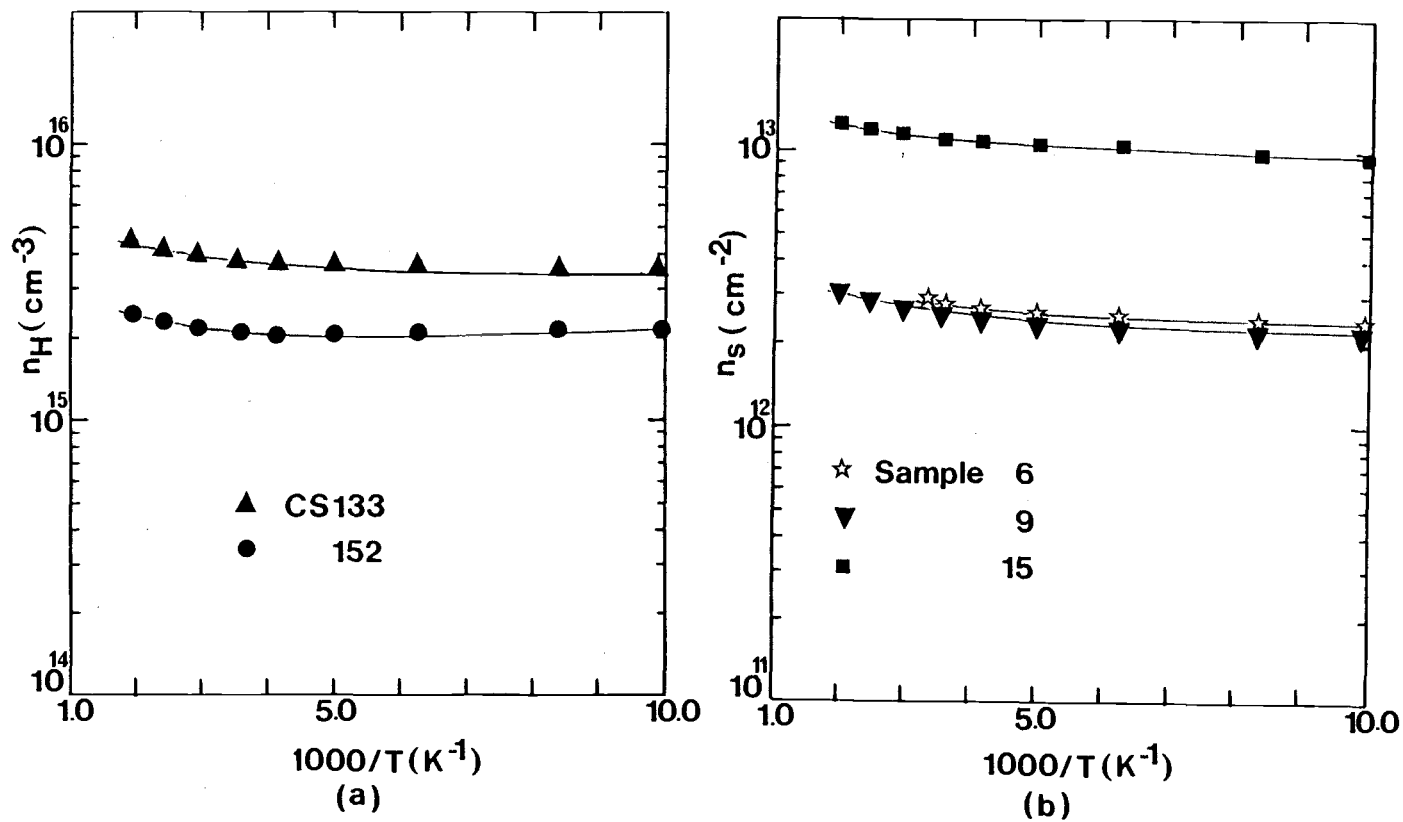


Figure 4.15. Temperature dependence of (a) Hall electron concentration in as-grown VPE GaAs and (b) activated surface carrier concentration in implanted and annealed VPE GaAs.

implant dose. The values of free carrier concentration,  $n (\approx N_D - N_A)$ , in the as-grown VPE GaAs samples at 300K listed in Table 4.5 were determined by capacitance-voltage measurements on the Schottky diodes and agree reasonably well with the values of  $n_H$  in the same samples.

#### 4.8 Analysis of Transport Data

The mobility-limiting mechanisms included in the analysis of the Hall data were ionized impurity (Brooks-Herring formulation)<sup>(54)</sup>, polar optical phonon<sup>(55)</sup>, deformation potential<sup>(56)</sup>, piezoelectric<sup>(57)</sup> and space-charge scattering<sup>(58,59)</sup> for the as-grown and the implanted materials. In the semi-insulating materials neutralized impurity scattering<sup>(36)</sup> had also to be included. The equations and programs used for analyzing the data are listed in Appendices I and III, respectively.

##### 4.8.1 Semi-Insulating GaAs

Theoretical fits to the variations of Hall mobility with temperature are indicated by the solid lines in Fig. 4.12. In some SI GaAs:Cr samples the Hall mobility is seen to increase with temperature. A probable reason is that the impurity concentration is inhomogeneously distributed through the sample<sup>(58,60)</sup>. Piezoelectric scattering was found to have a negligible contribution to the total mobility. A Hall scattering factor of unity was assumed for simplicity. It was also found that  $\mu_H \approx \mu_n$  for all samples in the temperature range of interest and the hole mobilities could be ignored. The parameters used for calculating the mobilities limited by polar optical phonon,

deformation potential and piezoelectric scattering are listed in Appendix II. The final values of the concentrations and the compensation ratios are listed in Table 4.9 for SI GaAs:Cr and Table 4.10 for SI undoped GaAs, respectively. Values for the deep acceptor and donor concentrations,  $N_{AA}$  and  $N_{DD}$ , and their energy depth measured from the conduction band edge, were estimated by fitting the experimental values of  $R_H T^{3/2}$ ,  $(qR_H)^{-1}$  and  $\sigma$  using the theoretical equations derived in Chapter II. The estimated values of  $(E_G - E_{AA})$  and  $(E_G - E_{DD})$  are listed in Tables 4.7 and 4.8, and of  $N_{AA}$  and  $N_{DD}$  in Tables 4.9 and 4.10.

#### 4.8.2 Ion-Implanted GaAs

The mobility-temperature data for four as-grown and three implanted samples, as shown in Figs. 4.12, 4.13 and 4.14, were analyzed in detail. It was found that the space-charge scattering did not have a pronounced effect in the temperature range  $80 < T < 300\text{K}$ . Reasonably good fits to the experimental data, as indicated by the solid lines, could be obtained up to 300K with values of total ionized impurity concentration  $(N_D + N_A)$  listed in Tables 4.5 and 4.6. A value of  $(N_A + N_D) = 1.4 \times 10^{17} \text{ cm}^{-3}$ , which is similar to those in the implanted samples, is obtained from the analysis of the temperature dependence of mobility in as-grown sample E. This comparison suggests that the reduced mobility in the implanted samples is due to increased impurity scattering and is not intrinsic to the implant and annealing process.

The same combination of scattering parameters, including space-

Table 4.9. Shallow and Deep Acceptor Level Concentrations and Compensation Ratios in SI GaAs:Cr Determined from Analysis of Hall-Effect Data.

Sample	$N_{AA}$ ( $\text{cm}^{-3}$ )	$N_{D3}$ ( $\text{cm}^{-3}$ )	$N_A$ ( $\text{cm}^{-3}$ )	$\frac{N_{AA}}{N_D - N_A}$
TEK 029	$4.2 \times 10^{16}$	$3.0 \times 10^{16}$	$2.1 \times 10^{16}$	4.6
TEK 0321	$2.3 \times 10^{16}$	$2.8 \times 10^{16}$	$2.0 \times 10^{16}$	2.8
TEK 311	$1.19 \times 10^{17}$	$2.0 \times 10^{17}$	$1.0 \times 10^{17}$	1.19
TEK 362	$1.9 \times 10^{16}$	$7.5 \times 10^{16}$	$6.5 \times 10^{16}$	1.9
TEK 381	$2.5 \times 10^{16}$	$2.9 \times 10^{16}$	$2.1 \times 10^{16}$	3.1
TEK 384	$3.5 \times 10^{16}$	$3.3 \times 10^{16}$	$2.3 \times 10^{16}$	3.5
TEK 385	$1.08 \times 10^{16}$	$9.4 \times 10^{16}$	$8.4 \times 10^{16}$	1.08
TEK 484	$2.5 \times 10^{16}$	$3.6 \times 10^{16}$	$2.6 \times 10^{16}$	2.5
TEK 489	$1.8 \times 10^{16}$	$3.1 \times 10^{16}$	$2.2 \times 10^{16}$	2.0
TEK 653	$3.0 \times 10^{16}$	$3.5 \times 10^{16}$	$2.5 \times 10^{16}$	3.0

Table 4.10. Shallow and Deep Donor Level Concentrations and Compensation Ratios in SI Undoped GaAs Determined from Analysis of Hall-Effect Data.

Sample	$N_{DD}$ ( $\text{cm}^{-3}$ )	$N_D$ ( $\text{cm}^{-3}$ )	$N_A$ ( $\text{cm}^{-3}$ )	$\frac{N_{DD}}{N_A - N_D}$
TEK 424	$2.1 \times 10^{17}$	$9.0 \times 10^{16}$	$9.8 \times 10^{16}$	26.25
TEK 647	$1.4 \times 10^{18}$	$1.0 \times 10^{17}$	$1.1 \times 10^{17}$	140.0
TEK 655	$4.3 \times 10^{16}$	$9.0 \times 10^{15}$	$1.0 \times 10^{16}$	43.0
TEK 656	$3.2 \times 10^{17}$	$2.3 \times 10^{16}$	$2.7 \times 10^{16}$	80.0
UNV2	$2.2 \times 10^{17}$	$1.8 \times 10^{17}$	$2.1 \times 10^{17}$	7.3
VL1B	$7.2 \times 10^{16}$	$2.2 \times 10^{16}$	$2.4 \times 10^{16}$	36.0
VL1T	$3.0 \times 10^{16}$	$2.1 \times 10^{16}$	$2.3 \times 10^{16}$	15.0
V221	$3.5 \times 10^{16}$	$1.7 \times 10^{16}$	$1.8 \times 10^{16}$	35.0

charge scattering, did not provide a good fit to the experimental data for  $T > 300\text{K}$ . The calculated values using  $N_s \cdot A = 3.5 \times 10^4 \text{ cm}^{-1}$  for the as-grown sample CS107 and  $4.7 \times 10^4 \text{ cm}^{-1}$  for the implanted sample 9 are shown by dashed lines in Figs. 4.13 and 4.14, respectively.  $N_s$  and  $A$  are, respectively, the concentration and effective scattering area of the space-charge regions<sup>(58)</sup>. It is expected that the magnitude of the mobility limited by space-charge scattering would be considerably altered by photoexcitation due to a change in the width of the space-charge region. However, little or no change was observed in the mobility values upon photoexcitation at high temperatures in both classes of samples, as shown in Figs. 4.13 and 4.14. Hence, some other mechanism must be invoked to explain the results. It is evident from the photoluminescence spectra that C is a distinct acceptor specie in as-grown VPE GaAs as well as in the implanted samples<sup>(21)</sup>. C in GaAs has a large electro-negativity compared to As, a small ionization energy, and consequently would introduce additional scattering due to a highly localized central-cell potential. Based on these properties, Stringfellow and Künzel<sup>(61)</sup> have recently demonstrated that the acceptor C, or an associate involving C, acts as a scattering center in  $\text{Ga}_{1-x}\text{Al}_x\text{As}$ . Their observations in the ternary material were very similar to the ones in this study. The mobility data were reanalyzed taking into account this central-cell correction, expressed by<sup>(61)</sup>

$$\mu = \frac{3.4 \times 10^{20}}{N_A} \left[ \frac{15}{8} (kT)^{1/2} + \frac{E_A}{(kT)^{1/2}} \right] (\text{cm}^2/\text{V.s}) \quad (4-1)$$

$N_A$  is the concentration of the scattering centers and  $E_A$  is the ionization energy for the electrons bound to them. The agreement with the experimental data up to 500K with  $E_A = 0.055$  eV<sup>(61)</sup> and using  $N_A = 2.2 \times 10^{15}$  and  $1.4 \times 10^{16}$  cm<sup>-3</sup> for samples CS107 and 9, respectively, was excellent. This is depicted in Figs. 4.13 and 4.14 by the solid lines for  $T > 300$ K. The disagreement at higher temperatures ( $\geq 500$ K) is probably due to increased substrate conduction. Similar agreement is depicted by the solid lines for  $T > 300$ K in Fig. 4.12 in the case of as-grown samples CS152 and E.

#### 4.9 Photocurrent Spectra in Semi-Insulating GaAs

These measurements were performed to confirm some of the results obtained from PICT and high-temperature Hall measurements and to detect deep levels which may not have been revealed by the previous measurements. The photocurrent spectra were recorded in the spectral range 0.4 - 1.5 eV with a Jarrel-Ash monochromator with an appropriate combination of filters. The device configuration was the same as that for the PICT measurements. The constant electric field across the samples varied in the range  $(1.0 \sim 3.5) \times 10^2$  V/cm. Typical photocurrent spectra in SI GaAs:Cr at 100 and 203K are shown in Fig. 4.16(a).

Chromium in GaAs is usually located in a Ga site giving rise to a deep-lying acceptor impurity. Four charge-states of the Cr-related centers have been reported<sup>(62)</sup>, giving rise to multiple activation energies between 0.56 to 0.9 eV<sup>(63)</sup>. The onset at 0.65 eV has been observed by several investigators and is probably related to oxy-

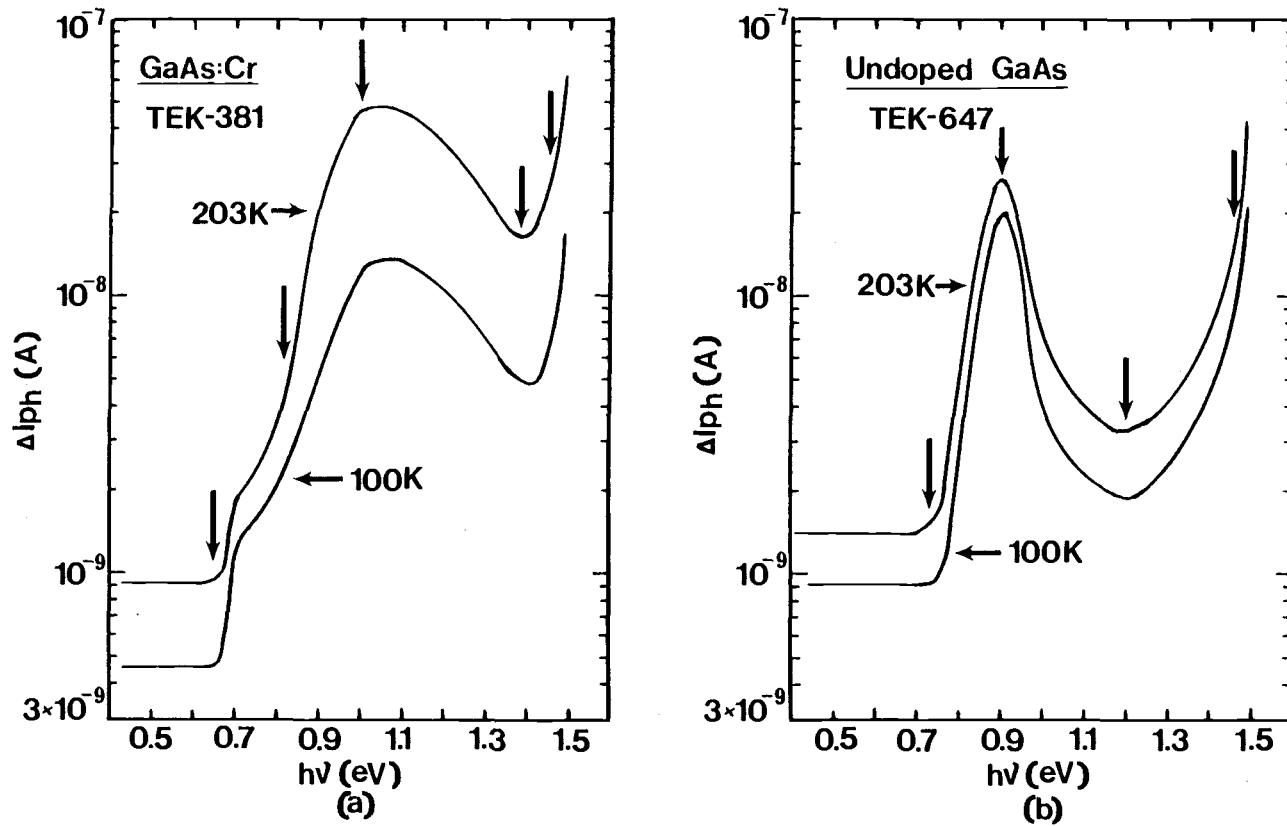


Figure 4.16. Photocurrent spectra obtained at  $T = 203$  and  $100\text{K}$  for (a) SI GaAs:Cr and (b) SI undoped GaAs.

gen<sup>(63,64)</sup>. The rise in photosensitivity at 0.81 eV is probably due to Cr<sup>(63,65)</sup>. The peak at  $\sim 1.0$  eV has been attributed to the intra-transition from the  $^5T_2$  ground state to the  $^5E$  excited state of Cr<sup>2+(66)</sup>. The transition at 1.39 eV was observed for the first time in this study. It may be due to electron transition from an ubiquitous impurity or defect level.

With reference to Fig. 4.16(b), which depicts the photocurrent spectra for SI undoped GaAs, the onset at 0.73 eV has been observed by several investigators and is attributed to oxygen<sup>(67,68)</sup>. The transition at 1.2 eV has been observed by Williams<sup>(69)</sup> and Farbe<sup>(70)</sup>, but its origin is yet unknown.

#### 4.10 Discussion

The hole trap with  $\Delta E_T = 0.86 \pm 0.01$  eV, which is detected in almost all the SI GaAs:Cr samples, is attributed to Cr<sup>(71)</sup>. The  $0.90 \pm 0.01$  eV electron trap level detected in the same samples is attributed to electron emission from the same centers<sup>(21,27)</sup>. The  $0.58 \pm 0.01$  and  $0.53 \pm 0.01$  eV electron and hole trap levels, respectively, are ascribed to unknown impurities. The electron trap may be identical to the 0.60 eV electron trap reported by Fairman and Oliver<sup>(72)</sup> in SI GaAs or center EL3 (0.575 eV) reported by Martin et al.<sup>(73)</sup> in VPE GaAs. The hole trap has thermal activation energy and capture cross section very similar to trap HS1 (0.58 eV) reported by Mitonneau et al.<sup>(74)</sup> in LPE GaAs. The  $0.73 \pm 0.01$  eV hole trap level also detected in SI undoped GaAs, has a thermal activation energy very similar to trap B (0.71 eV) detected by Lang and Logan<sup>(27)</sup> in LPE GaAs and related to a native defect. However, the thermal hole

capture cross sections are at least 2 or 3 orders higher than for the 0.73 eV centers detected in this study. The 0.16 eV hole trap level, detected for the first time in this study, can probably be ascribed to native defects since it was detected in both SI GaAs:Cr and undoped GaAs. Fewer deep levels were detected in SI undoped GaAs. The  $0.98 \pm 0.01$  eV electron trap level, detected for the first time in this study, can be ascribed to unknown impurities and further studies are necessary to elucidate its origin.

The presence of Cr was confirmed by high-temperature Hall and photocurrent measurements. Similarly the presence of the deep donor level at  $E_c - 0.73$  eV detected by high-temperature Hall measurement on SI undoped GaAs was confirmed by the photocurrent measurements. This level could not be detected by the PICT measurements due to strong optical quenching, possibly by the deep level at  $E_v + 0.9$  eV. The consistency in the values of the ionization energy obtained from the different measurements indicates minimal lattice coupling associated with these centers.

The 0.83 and  $0.37 \pm 0.01$  eV electron trap levels detected in as-grown VPE GaAs are characteristically absent after implant and anneal. Hasegawa and Majerfeld<sup>(75)</sup> have shown that the 0.83 eV electron trap level is annealed by heat treatment under  $H_2$ -flow for 30 min. at 600°C and above. Hence, it may be concluded that implantation is not responsible for the removal of this center. Another possibility is that the center is present after implant and anneal but electron emission from the 0.53 eV electron trap level prevents its detection. The mechanism involved in the removal of

the  $0.37 \pm 0.01$  eV trap is not yet understood.

A 0.15 eV hole trap level is consistently observed in the implanted VPE GaAs samples. The 0.53 eV electron trap level is also consistently present except in the samples implanted with higher doses. Both levels have also been detected in implanted SI GaAs:Cr and are believed to be characteristic of Si-implantation and annealing in GaAs. The 0.53 eV electron trap level may prove detrimental to device performance since it appears near room temperature. It is evident from this study that relatively few deep-level traps are introduced in GaAs by implantation. A similar observation was made by Jervis et al.<sup>(20)</sup> from measurements on implanted LPE GaAs.

The 0.86 eV hole trap level detected in some as-grown VPE layers with a very low density and in the implanted layers with larger density is attributed to Cr impurities, probably diffusing from the substrate. The identification with Cr was confirmed after measurement of the transient capacitance spectra in lightly-doped VPE GaAs:Cr. Depending on the position of the Fermi level, the Cr-centers are usually filled more with electrons than holes<sup>(27)</sup>. Hence it is more likely to detect hole emission, as was the case in this study, if the Cr concentration is low. Therefore, the 0.86 eV hole trap concentrations listed in Tables 4.5 and 4.6 are not the total concentrations of the Cr centers. Kaufmann and Schneider<sup>(76)</sup> have recently reported the results of Electron Spin Resonance (ESR) studies which indicate that isolated Cr can act as a hole trap in GaAs. If there is any electron emission from the Cr-center, it may be masked by electron emission from the 0.83 eV electron trap level in the as-grown

VPE samples and the 0.53 eV electron trap level in the implanted samples. The greatly increased concentration of the Cr centers observed in the implanted samples, compared to the as-grown VPE samples, is attributed to the outdiffusion of Cr from the substrate during the thermal anneal<sup>(77)</sup>. However, emission from the Cr center was not observed in the implanted samples 14 and 15 which suggests that Cr atoms did not outdiffuse sufficiently to reach the active layers.

The mobility profiles as a function of temperature are markedly different for the as-grown VPE and implanted samples, the values being lower in the latter. A detailed analysis of the mobility data including the relevant scattering mechanisms indicate that the decreased mobility is due to increased ionized impurity density. The values of  $n_g$  in implanted samples 14 and 15 are actually higher than the implant dose. A similar effect has been observed by Asbeck et al.<sup>(77)</sup> in ion-implanted GaAs:Cr.

## CHAPTER V

PROPERTIES OF SEMI-INSULATING AND ION-IMPLANTED InP

The characteristics of deep-level defects in semi-insulating and ion-implanted InP, including the compensating Fe- and Cr-related levels, are reported in this chapter. The nature of the traps were inferred by performing the PICT measurements with intrinsic monochromatic photoexcitation. The energy positions of some of the more dominant defect levels were also obtained from spectral photocurrent variations and from analysis of these spectra. The transport parameters were obtained from analyses of temperature-dependent Hall measurement data.

### 5.1 Fabrication of Devices

The semi-insulating InP used for this work was grown by the liquid encapsulation Czochralski technique and nominally oriented in the (100)-direction. The resistivity of the samples varied from  $\sim 10^3$  to  $\sim 10^7$  ohm-cm at room temperature. LPE layers of InP were grown by the procedure described in Chapter III.  $^{28}\text{Si}^+$  ions were subsequently implanted into the InP samples at an energy of 100 or 200 KeV with doses varying from  $6 \times 10^{11}$  to  $5 \times 10^{13}$   $\text{cm}^{-2}$ . Either a 2000-3000 Å silox or a 1000 Å  $\text{Si}_3\text{N}_4$  encapsulating layer was deposited on the implanted surface which was then annealed at temperatures ranging from 670 to 800°C for 20 min. in a forming gas ambient.

Devices for PICT, transient capacitance and Hall measurements were made by following a procedure identical to that for the GaAs

samples. The samples were etched by using a 0.2% solution of bromine methanol and a Ag-Sn eutectic alloy was used for ohmic contacts. Thin natural oxide films were grown<sup>(78)</sup> on the InP epitaxial and implanted layers before evaporating Au Schottky diodes in order to enhance the barrier height.

## 5.2 Photo-Induced Current Transient Measurements on Semi-Insulating InP

Deep levels in SI InP:Fe and InP:Cr have been studied by PICT measurements for the first time. Arrhenius plots for the emissions detected in SI InP:Fe and InP:Cr are shown in Figs. 5.1 and 5.2, respectively. The dominant hole emission observed in SI InP:Cr with activation energy  $\Delta E_T = 0.96 \pm 0.01$  eV and  $\sigma_\infty = (9.5 \pm 1.0) \times 10^{-13}$  cm<sup>2</sup> is probably from the Cr-level and the dominant hole emission in SI InP:Fe with  $\Delta E_T = 0.69 \pm 0.01$  eV and  $\sigma_\infty = (1.4 \pm 0.5) \times 10^{-16}$  cm<sup>2</sup> is thought to arise from the Fe-level. An electron trap with  $\Delta E_T = 0.68 \pm 0.01$  eV and  $\sigma_\infty = (4.7 \pm 0.5) \times 10^{-15}$  cm<sup>2</sup> and two hole traps with  $\Delta E_T = 0.50 \pm 0.005$  eV and  $0.67 \pm 0.01$  eV and  $\sigma_\infty = (4.6 \pm 0.5) \times 10^{-19}$  cm<sup>2</sup> and  $(1.3 \pm 0.5) \times 10^{-17}$  cm<sup>2</sup>, respectively, were detected in some samples of SI InP:Fe. The electron trap with  $\Delta E_T = 0.68 \pm 0.01$  eV in SI InP:Fe can be identified with the trap E4 ( $0.59 \pm 0.04$  eV) detected by McAfee et al.<sup>(7)</sup> in bulk LEC n-InP. The capture cross section of the trap E4 is almost identical to that of the  $0.68 \pm 0.01$  eV electron trap. The trap also seems identical with trap Q (0.68 eV) seen by White et al.<sup>(79)</sup> and trap A (0.63 eV) detected by Wada et al.<sup>(80)</sup>. The latter have reported that the center is frequently detected in LEC bulk InP.

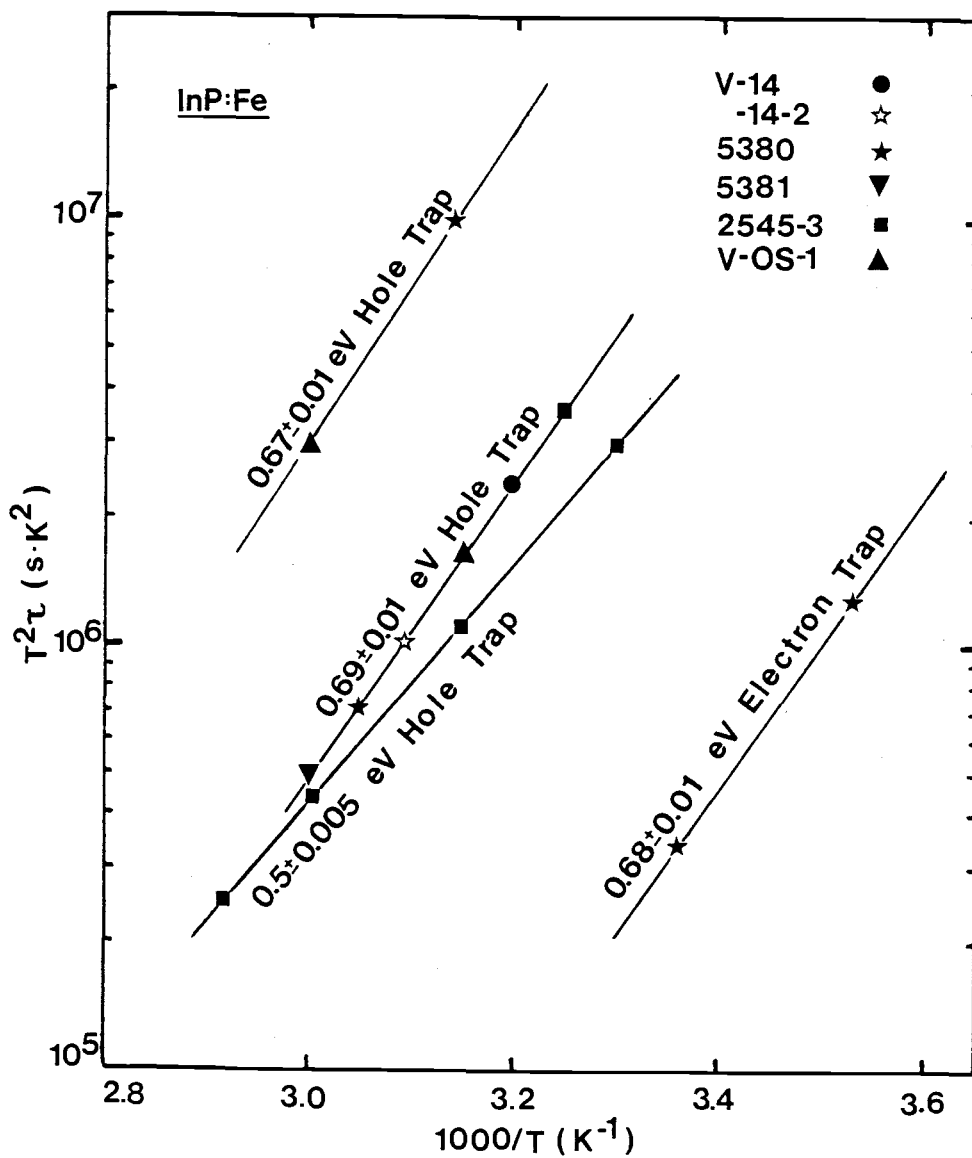


Figure 5.1. Arrhenius plots for electron and hole trap levels in SI InP:Fe. The symbols located arbitrarily represent the different samples and are not data points.

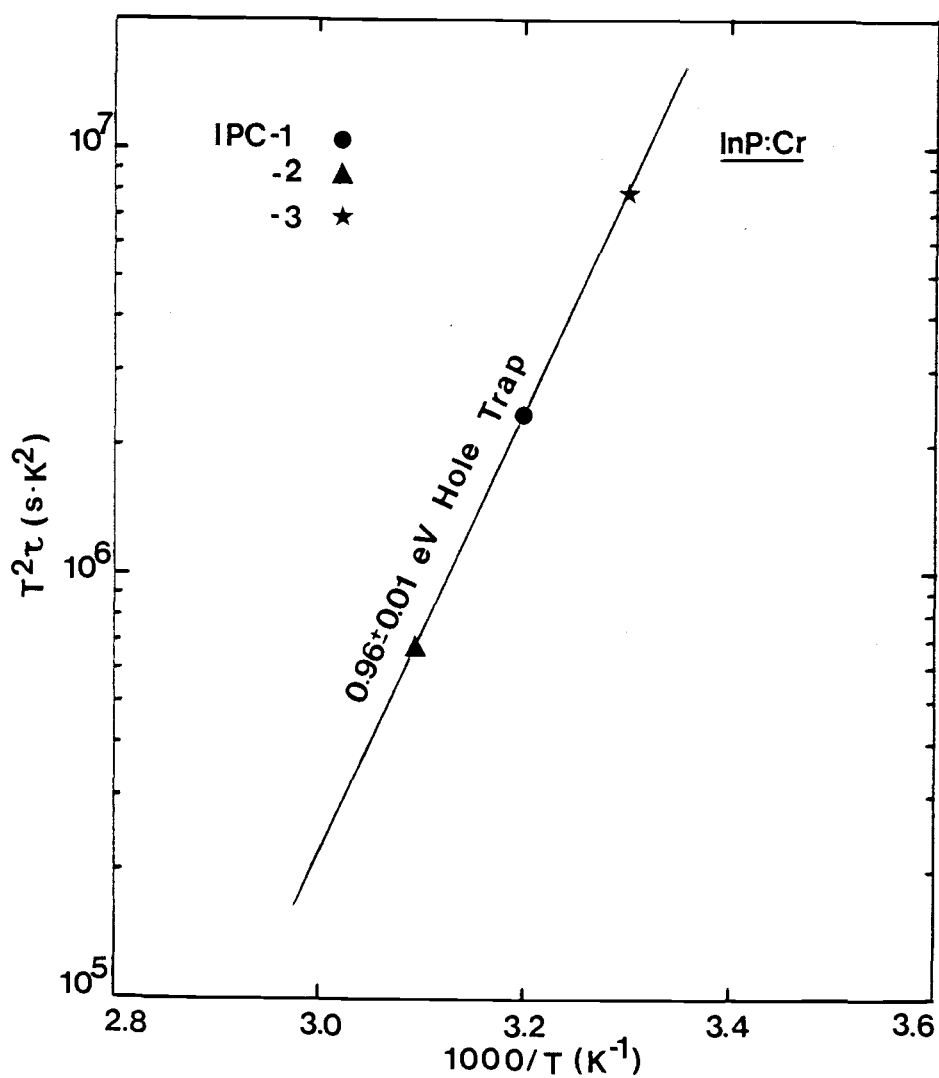


Figure 5.2. Arrhenius plots for hole trap levels in SI InP:Cr. The symbols located arbitrarily represent the different samples and are not data points.

The trap was not detected in SI InP:Cr. The possible explanations are that its concentration in this material is below the detection limit or it is absent. In a preliminary effort to identify the physico-chemical origin of this center, heat treatment on the SI InP:Fe sample was performed under  $H_2$ -flow in a high purity LPE furnace for 15 min. at  $\sim 490^\circ\text{C}$ . The trap was not detected after such annealing. It can be said, with some caution, that the trap is associated with native defects. The hole traps with  $\Delta E_T = 0.50 \pm 0.005$  and  $0.67 \pm 0.01$  eV are not consistently detected and at this point their origin is unknown. The identity of the two traps, which are probably observed for the first time, needs to be investigated in more detail. It may be added that the 0.67 eV trap was also removed after the heat treatment. The trap parameters on SI InP:Fe and InP:Cr are listed in Table 5.1.

It should be noted that the capture cross sections,  $\sigma_\infty$ , were calculated from the emission-rate prefactor in Eq. (2-12) and may be slightly larger than the value determined directly from the observation of capture rates<sup>(27,81)</sup>. Also, the thermal ionization energy  $\Delta E_T$  includes the barrier to thermal capture,  $\Delta E_B$ , by virtue of the equation  $\sigma = \sigma_\infty \exp(-\Delta E_B/kT)$ . However, the consistency in the value of the energy position of the Fe and Cr levels, which was of primary interest in this study, indicates that these centers do not have significant barriers to thermal capture.

### 5.3 Transient Capacitance Measurements on Liquid Phase Epitaxial InP

The Arrhenius plots of traps detected in as-grown LPE InP are

Table 5.1. Characteristics of Deep Levels in SI InP:Fe and InP:Cr.

Description	Sample	Electron Trap		Hole Trap	
		$\Delta E_T$ (eV)	$\sigma_\infty$ (cm <sup>2</sup> )	$\Delta E_T$ (eV)	$\sigma_\infty$ (cm <sup>2</sup> )
InP:Fe	V-OS-1			0.69	$1.4 \times 10^{-16}$
				0.67	$1.3 \times 10^{-17}$
	V-14			0.69	$1.5 \times 10^{-16}$
	V-14-2			0.68	$1.4 \times 10^{-16}$
	5380	0.68	$4.7 \times 10^{-15}$	0.69	$1.5 \times 10^{-16}$
				0.66	$1.3 \times 10^{-17}$
	5381			0.68	$1.4 \times 10^{-16}$
	2545-3			0.69	$1.4 \times 10^{-16}$
			0.50	$4.6 \times 10^{-19}$	
InP:Cr	IPC-1			0.96	$9.5 \times 10^{-13}$
	IPC-2			0.95	$9.6 \times 10^{-13}$
	IPC-3			0.96	$9.5 \times 10^{-13}$

depicted in Fig. 5.3. A center identical to the electron trap with an activation energy of  $0.38 \pm 0.01$  eV has been recently reported by Nickel et al.<sup>(82)</sup> and by McAfee et al.<sup>(7)</sup>. The origin of this trap is yet unknown<sup>(82)</sup> but the center can be identified with trap E (0.43 eV) reported by Wada et al.<sup>(80)</sup>, and with trap T (0.40 eV) or Trap U (0.42 eV) detected by White et al.<sup>(79)</sup>. The  $0.22 \pm 0.01$  eV hole trap is detected for the first time in this study. At this stage, the origin of the hole trap level is unknown. The characteristics of the traps detected in as-grown LPE InP are listed in Table 5.2.

#### 5.4 Transient Capacitance Measurements on Ion-Implanted Liquid Phase Epitaxial InP

The Arrhenius plots of traps observed in implanted and annealed LPE InP are shown in Fig. 5.4. The traps detected in as-grown LPE InP are characteristically absent after implant and anneal. A single electron trap level with  $\Delta E_T = 0.17 \pm 0.01$  eV was detected in almost all the implanted and annealed LPE InP samples.

McAfee et al.<sup>(7)</sup> have reported that the concentration of the trap E2 ( $0.35 \pm 0.03$  eV) detected by them in bulk InP was considerably reduced after a 4-h heat treatment at  $450^\circ\text{C}$  under a vacuum of  $10^{-3}$  Torr. Hence, it is possible that the  $0.38 \pm 0.01$  eV electron trap level detected in this study is removed from the as-grown LPE samples during the thermal anneal rather than the implant process. Another possibility is that emission from the trap level, if still present, is screened by stronger emission from the  $0.17 \pm 0.01$  eV electron trap.

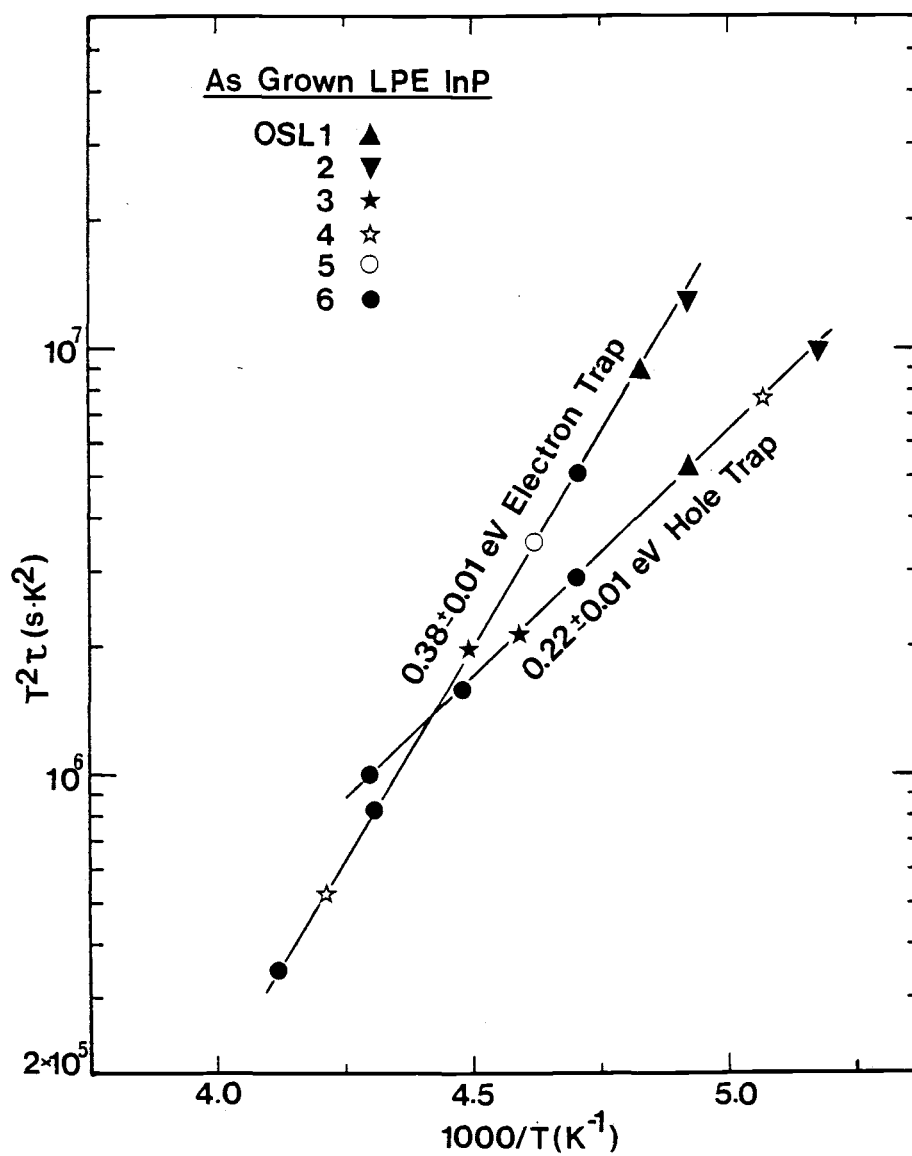


Figure 5.3. Arrhenius plots for electron and hole trap levels in as-grown LPE InP. The symbols located arbitrarily represent the different samples and are not data points.

Table 5.2. Characteristics of Deep Levels in As-Grown LPE InP.

Sample	Electron Trap			Hole Trap		
	$\Delta E_T$ (eV)	$N_T$ ( $\text{cm}^{-3}$ )	$\sigma_\infty$ ( $\text{cm}^2$ )	$\Delta E_T$ (eV)	$N_T$ ( $\text{cm}^{-3}$ )	$\sigma_\infty$ ( $\text{cm}^2$ )
OSL1	0.38	$1.4 \times 10^{15}$	$1.4 \times 10^{-18}$	0.22	$1.7 \times 10^{16}$	$1.5 \times 10^{-23}$
OSL2	0.37	$1.9 \times 10^{14}$	$1.5 \times 10^{-18}$	0.21	$1.2 \times 10^{15}$	$1.6 \times 10^{-23}$
OSL3	0.39	$9.2 \times 10^{13}$	$1.3 \times 10^{-18}$	0.23	$1.1 \times 10^{15}$	$1.5 \times 10^{-23}$
OSL4	0.38	$1.2 \times 10^{14}$	$1.4 \times 10^{-18}$	0.21	$6.1 \times 10^{15}$	$1.4 \times 10^{-23}$
OSL5	0.37	$7.6 \times 10^{14}$	$1.5 \times 10^{-18}$	-	-	-
OSL6	0.38	$1.3 \times 10^{15}$	$1.4 \times 10^{-18}$	0.22	$1.2 \times 10^{16}$	$1.5 \times 10^{-23}$

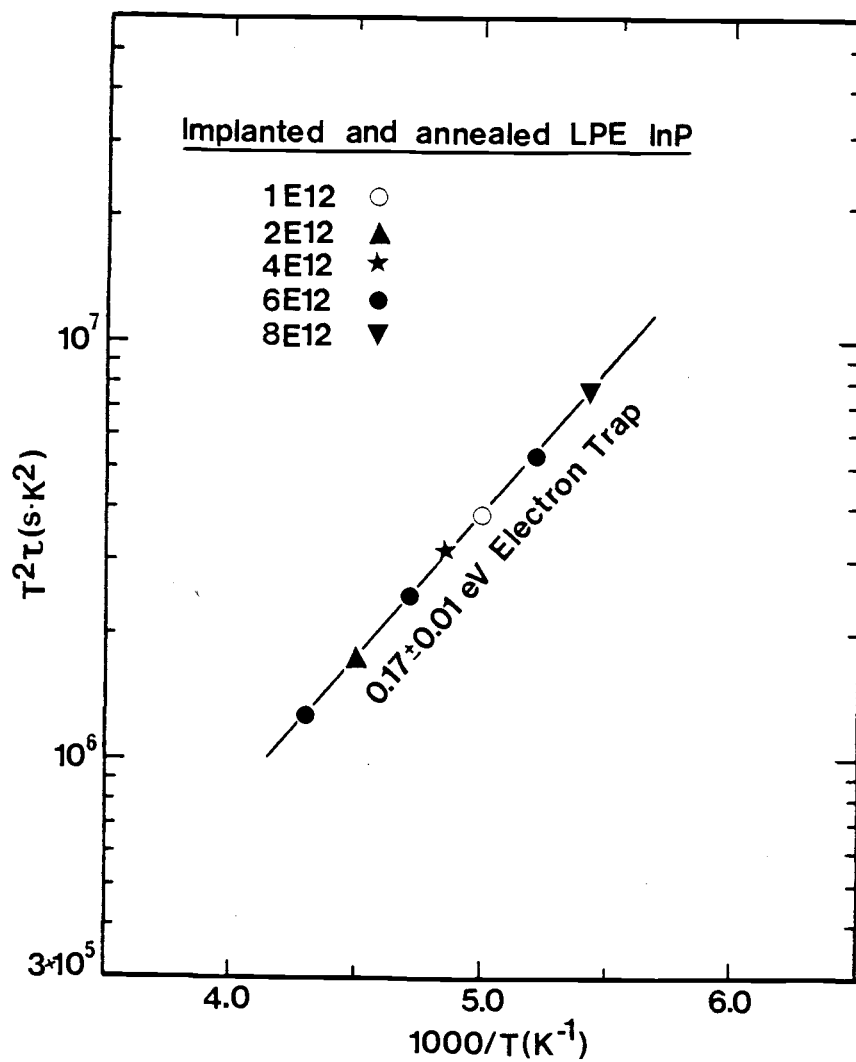


Figure 5.4. Arrhenius plots for electron trap levels in Si-implanted and annealed LPE InP. The symbols located arbitrarily represent the different samples and are not data points.

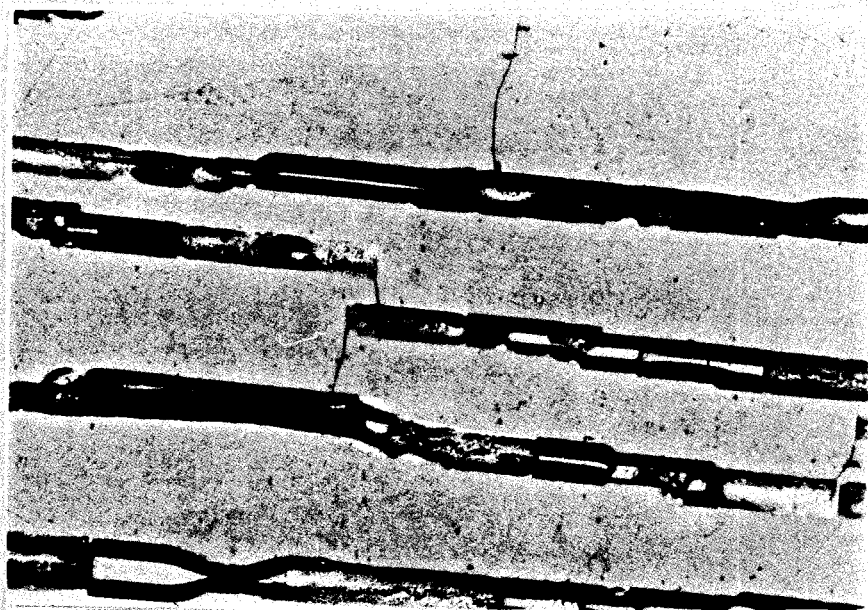
Table 5.3. Characteristics of Deep Levels in Si-Implanted and Annealed LPE InP. All the Samples were Thermally Annealed with a 1000 Å Si<sub>3</sub>N<sub>4</sub> Encapsulating Layer at 670°C for 20 min. in Flowing Forming Gas.

Sample	Implant Dose (cm <sup>-2</sup> )	Electron Trap		
		ΔE <sub>T</sub> (eV)	N <sub>T</sub> (cm <sup>-3</sup> )	σ <sub>∞</sub> (cm <sup>2</sup> )
OSL1	1.0 x 10 <sup>12</sup>	0.17	5.3 x 10 <sup>15</sup>	1.9 x 10 <sup>-24</sup>
OSL2	8.0 x 10 <sup>12</sup>	0.18	1.4 x 10 <sup>15</sup>	1.8 x 10 <sup>-24</sup>
OSL3	2.0 x 10 <sup>12</sup>	0.16	2.3 x 10 <sup>15</sup>	1.8 x 10 <sup>-24</sup>
OSL4	4.0 x 10 <sup>12</sup>	0.16	3.7 x 10 <sup>15</sup>	2.0 x 10 <sup>-24</sup>
OSL5	1.0 x 10 <sup>13</sup>	-	-	-
OSL6	6.0 x 10 <sup>12</sup>	0.17	1.3 x 10 <sup>16</sup>	1.9 x 10 <sup>-24</sup>

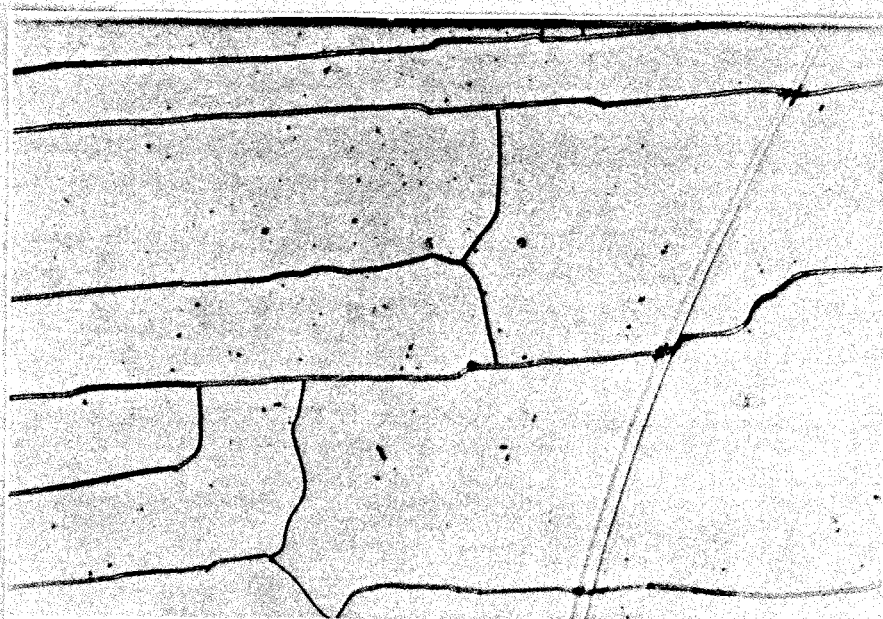
No hole trap levels were detected in this material. The characteristics of traps detected in implanted LPE samples are listed in Table 5.3.

### 5.5 Ion-Implanted and Annealed Semi-Insulating InP

In most of the earlier work reported in the literature, InP has been implanted with dopant ion doses of  $2 \times 10^{12} \text{ cm}^{-2}$  or higher at energies  $\geq 150 \text{ KeV}$ .  $\text{SiO}_2$  encapsulating layers are known to decompose if the deposition temperature is too high and thickness of the encapsulant is below  $2000 \text{ \AA}$  (17,18). Si ions were implanted in SI InP:Fe and InP:Cr samples for this study at an energy of  $100 \text{ KeV}$ , with doses ranging from  $6 \times 10^{11}$  to  $8 \times 10^{12} \text{ cm}^{-2}$ . A  $2000 \text{ \AA}$  silox encapsulating layer was deposited at  $420^\circ\text{C}$  on the implanted surface which was then annealed at temperatures ranging from  $750$  to  $800^\circ\text{C}$  for  $20 \text{ min.}$  in an ambient of flowing forming gas. In a second batch of samples,  $\text{Si}^+$  was implanted at  $200 \text{ KeV}$  with doses between  $1 \times 10^{12}$  to  $5 \times 10^{13} \text{ cm}^{-2}$ . In this case a  $3000 \text{ \AA}$  silox encapsulating layer was used to protect the samples during post-implantation anneal at  $670^\circ\text{C}$  in forming gas. Thermal decomposition of InP sample surface in the form of localized cracking and peeling, as shown in Fig. 5.5(a) and (b), was observed in some samples. A sputtered silicon nitride encapsulating layer on implanted LPE InP with a thickness of  $1000 \text{ \AA}$  seemed to prevent thermal decomposition during post-implantation anneal.



(a)  $50\mu\text{m}$



(b)  $50\mu\text{m}$

Figure 5.5. Photomicrographs of the decomposition in InP during post-implant anneal in (a) 2000 Å  $\text{SiO}_2$  encapsulating layer and (b) 3000 Å  $\text{SiO}_2$  with a piece of InP placed on top.

## 5.6 Transport Measurements

### 5.6.1 Semi-Insulating InP

Typical variations of Hall electron mobility with temperature in the range 350-600K in SI InP:Fe and InP:Cr are shown in Fig. 5.6(a) and (b), respectively. The plots of  $R_H T^{3/2}$ ,  $(qR_H)^{-1}$  and dark conductivity,  $\sigma$ , versus inverse temperature are depicted in Figs. 5.7, 5.8, and 5.9. It may be noticed that some samples of SI InP:Fe show significantly different variations of the above-mentioned transport parameters with temperature. The measured transport parameters at 400K in SI InP:Fe and InP:Cr are listed in Table 5.4.

### 5.6.2 Ion-Implanted InP

The variations of Hall electron mobility with temperature in the range 80-500K for as-grown and implanted LPE InP samples are shown in Figs. 5.10 and 5.11, respectively. A feature similar to that observed in GaAs is the significant decrease in mobility upon ion-implantation. Values of mobility at 300 and 80K are listed in Tables 5.5 for the as-grown samples and 5.6 for the implanted samples, respectively. It should be noted that the surface carrier concentration in all the implanted layers are more than the implant dose.

Hall measurements were performed on the implanted and annealed SI InP in the temperature range 100-500K. The measured Hall mobility and implant dose in the implanted SI InP samples are listed in Tables 5.7 for the first batch and 5.8 for the second batch, respectively. It is observed that n-type behavior with reasonable mobilities at 300K is obtained in implanted SI InP:Cr even for very low implant doses.

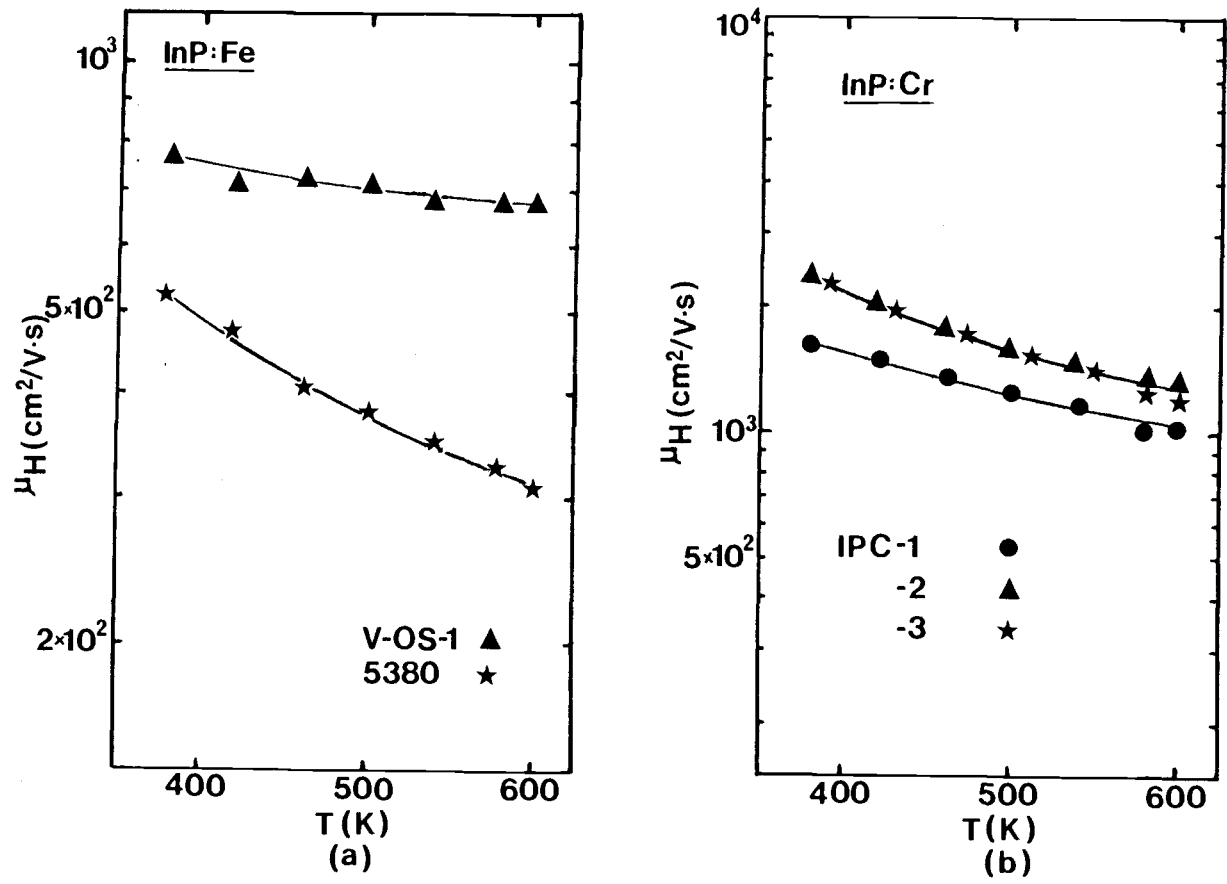


Figure 5.6. Variation of Hall mobility with temperature in (a) SI InP:Fe and (b) SI InP:Cr.

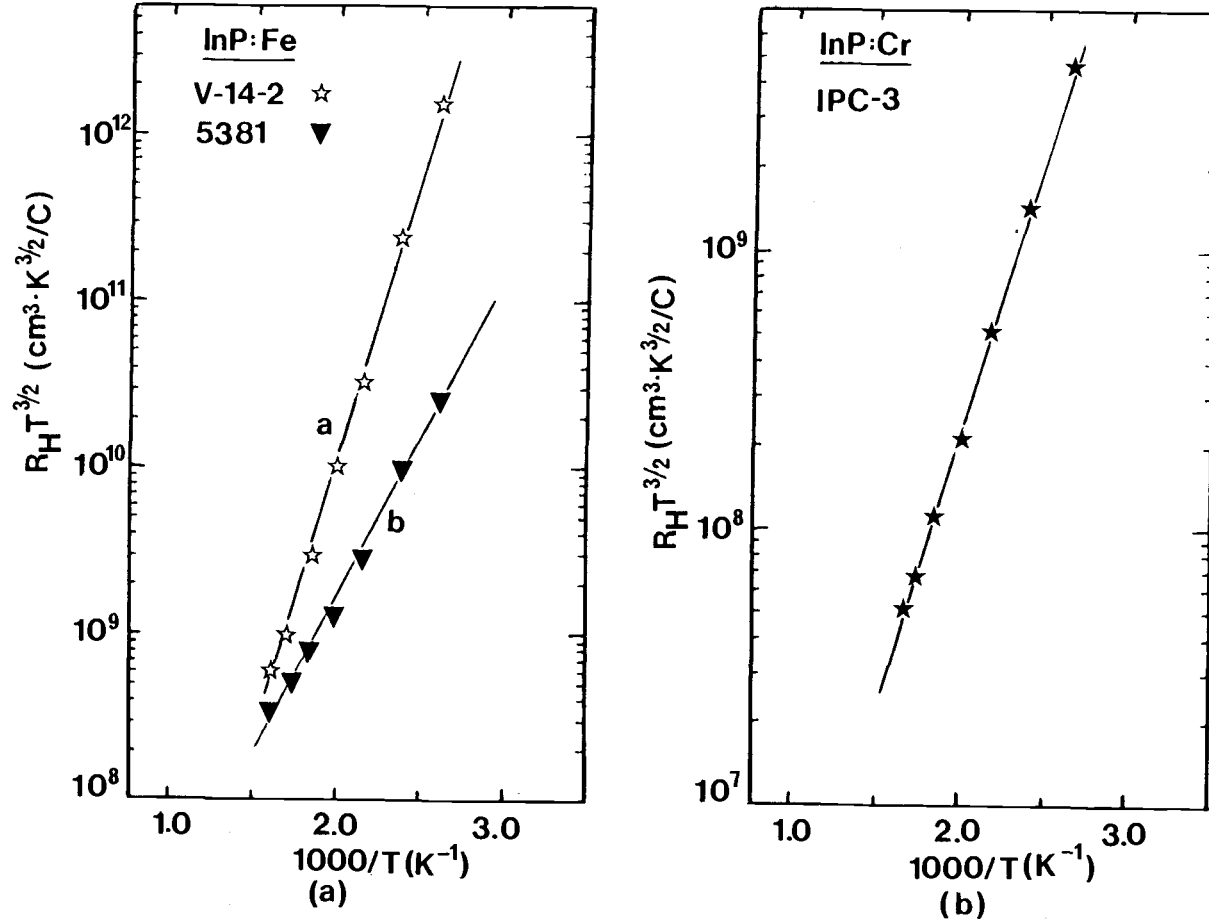


Figure 5.7. Plots of  $R_H T^{3/2}$  versus inverse temperature in (a) SI InP:Fe and (b) SI InP:Cr.

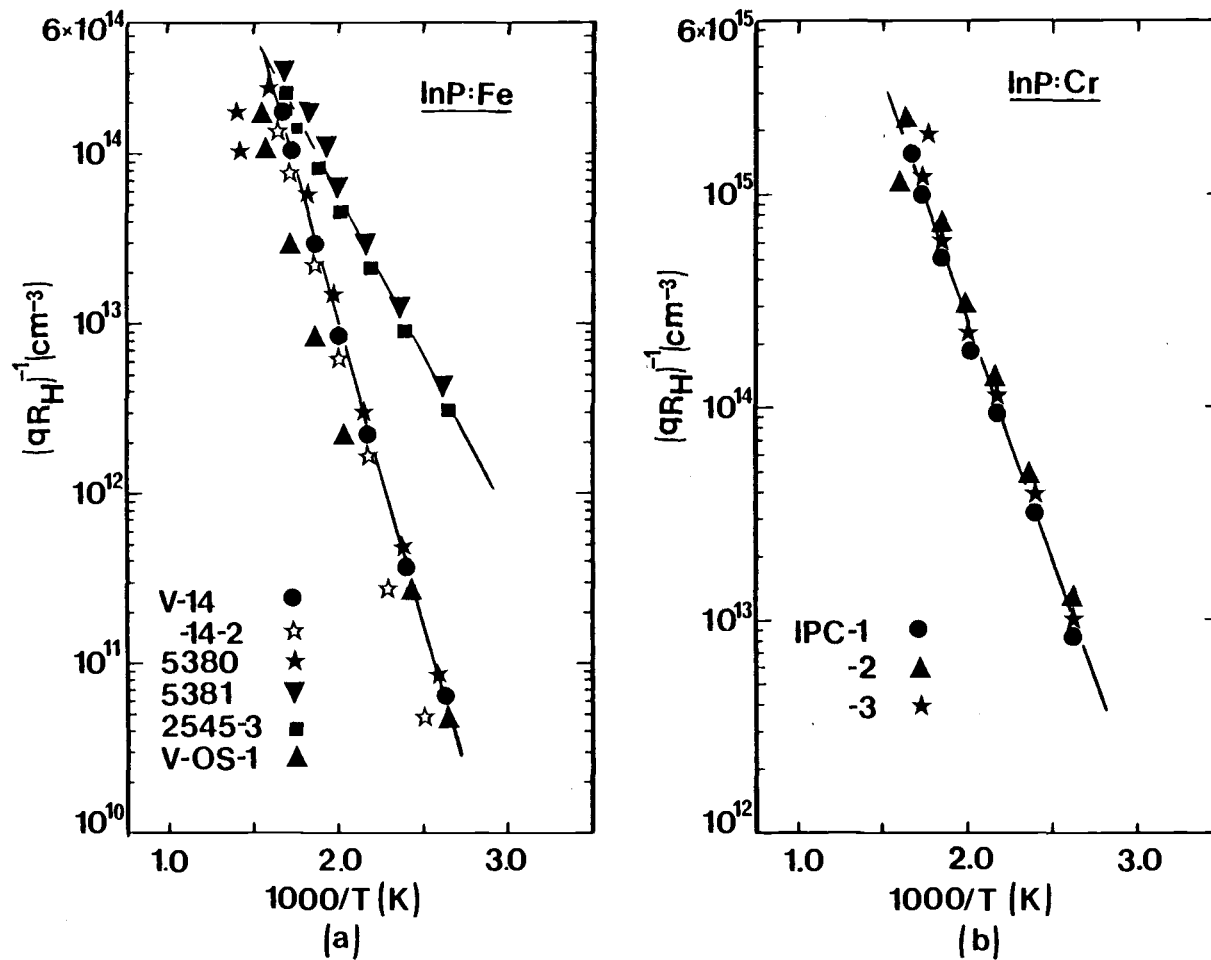


Figure 5.8. Plots of  $(qR_H)^{-1}$  versus inverse temperature in (a) SI InP:Fe and (b) SI InP:Cr.

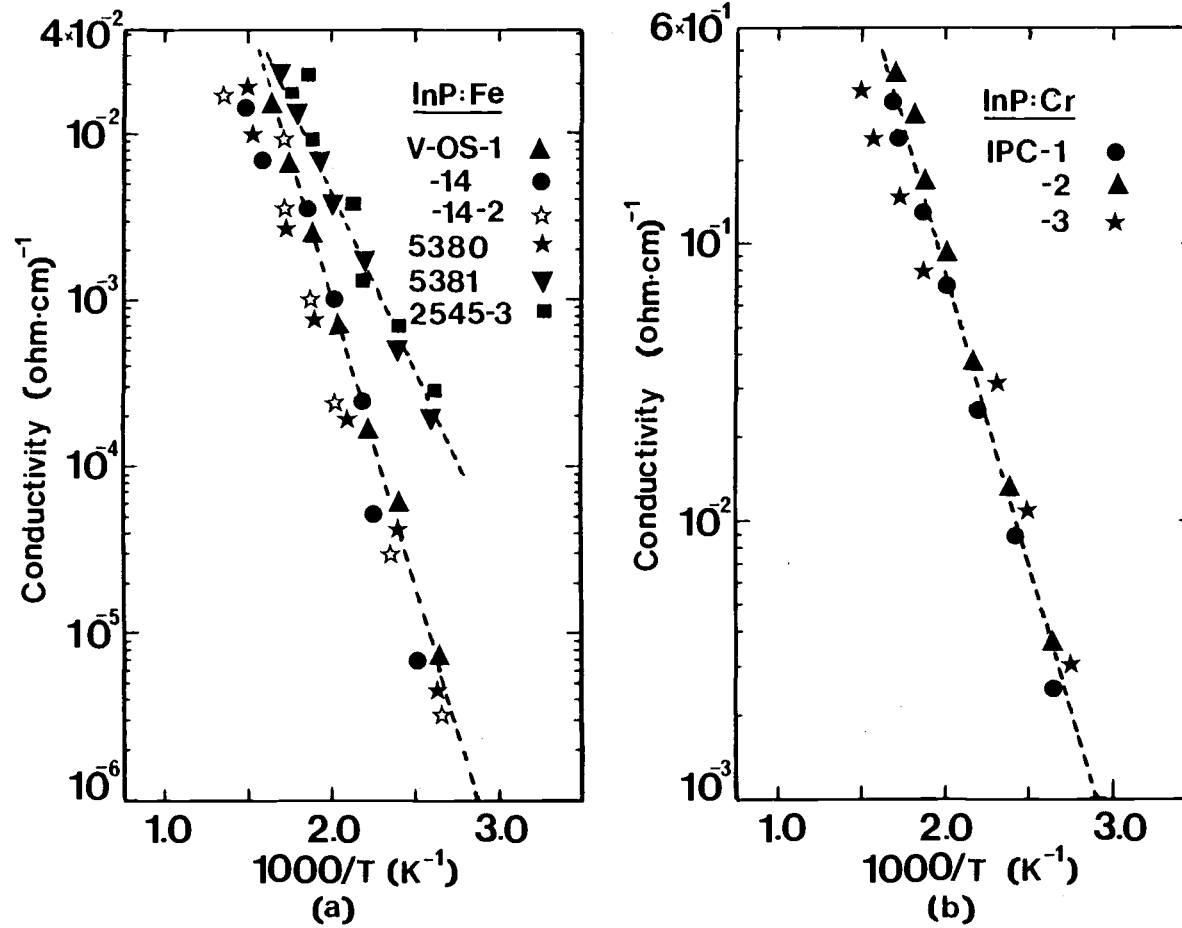


Figure 5.9. Plots of dark conductivity,  $\sigma$ , versus inverse temperature in (a) SI InP:Fe and (b) SI InP:Cr.

Table 5.4. Transport Data in SI InP:Fe and InP:Cr Obtained from Hall Measurements. Also Listed are Values of the Fermi Energy at 400K and Energy Position of the Deep Acceptor Levels Derived from Analysis of Hall-Effect Data.

Description	Sample	$(qR_H)^{-1}$ at 400K ( $\text{cm}^{-3}$ )	$\mu_H$ at 400K ( $\text{cm}^2/\text{V}\cdot\text{s}$ )	Slope of $\ln(R_H T^{3/2})^{-1}$ (eV)	$(E_G - E_{AA})$ From Analysis (eV)	$(E_G - E_F)$ at 400K From Analysis (eV)
InP:Fe	V-OS-1	$1.5 \times 10^{11}$	760	0.67	0.65	0.53
	V-14	$2.1 \times 10^{11}$	520	0.67	0.67	0.52
	V-14-2	$9.2 \times 10^{10}$	780	0.70	0.67	0.55
	5380	$1.7 \times 10^{11}$	520	0.71	0.66	0.53
	5381	$1.3 \times 10^{13}$	215	0.38	0.65	0.40
	2545-3	$2.5 \times 10^{13}$	200	0.40	0.66	0.38
InP:Cr	IPC-1	$1.6 \times 10^{13}$	1550	0.40	0.40	0.38
	IPC-2	$2.1 \times 10^{13}$	2025	0.41	0.40	0.37
	IPC-3	$2.05 \times 10^{13}$	2140	0.40	0.40	0.37

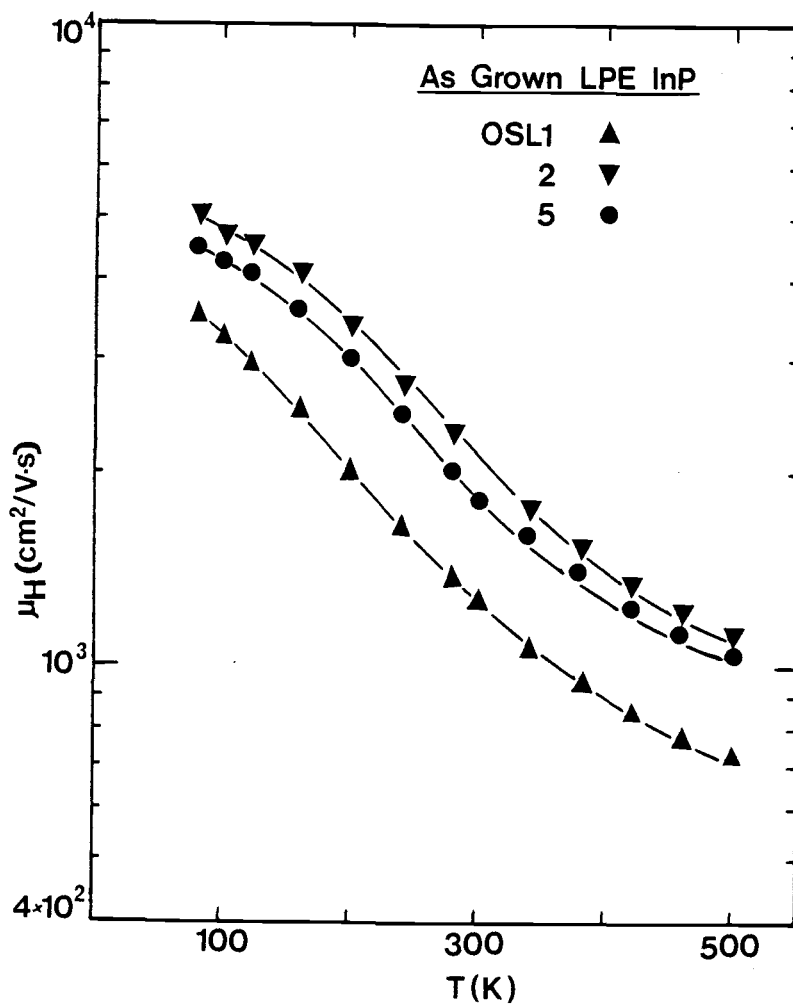


Figure 5.10. Variation of Hall electron mobility with temperature in as-grown LPE InP.

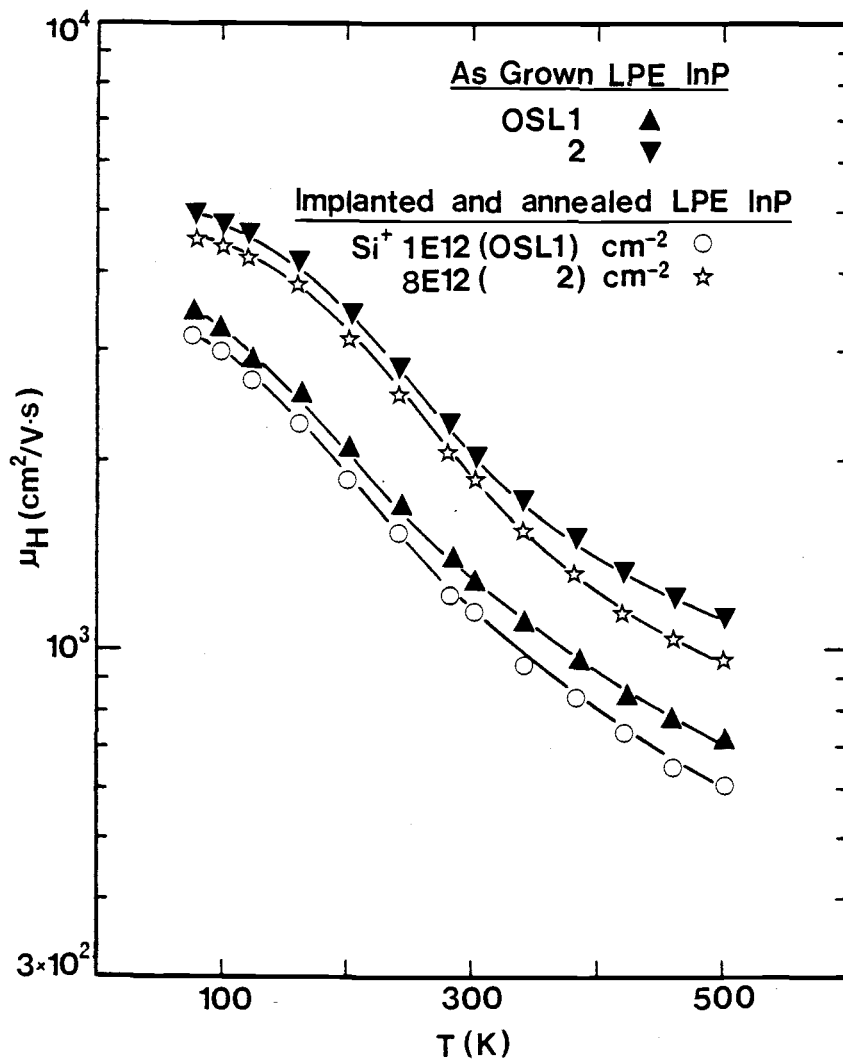


Figure 5.11. Variation of Hall electron mobility with temperature in Si-implanted and annealed LPE InP. The implant doses are mentioned in the diagram.

Table 5.5. Electrical Characteristics of As-Grown LPE InP.

Sample	$\mu_H$ at 300K (cm <sup>2</sup> /V.s)	$\mu_H$ at 80K (cm <sup>2</sup> /V.s)	n at 300K (cm <sup>-3</sup> )	Total Donor Con. $N_D$ (cm <sup>-3</sup> )	Total Acceptor Con. $N_A$ (cm <sup>-3</sup> )
OSL1	1275	3500	$2.6 \times 10^{17}$	$3.3 \times 10^{17}$	$6.0 \times 10^{16}$
OSL2	2035	5000	$6.4 \times 10^{16}$	$9.4 \times 10^{16}$	$3.0 \times 10^{16}$
OSL3	2086	-	$6.1 \times 10^{16}$	-	-
OSL4	1410	-	$2.5 \times 10^{17}$	-	-
OSL5	1825	4500	$8.5 \times 10^{16}$	$1.2 \times 10^{17}$	$3.4 \times 10^{16}$
OSL6	1175	-	$2.7 \times 10^{17}$	-	-

Table 5.6. Electrical Characteristics of Implanted and Annealed LPE InP. The Thermal Anneal for all Samples with a 1000 Å Si<sub>3</sub>N<sub>4</sub> Encapsulating Layer was Done at 670°C for 20 min. in Flowing Forming Gas.

Sample	Implant Doses (cm <sup>-2</sup> )	n <sub>s</sub> at 300K (cm <sup>-2</sup> )	Total Donor Con. N <sub>D</sub> (cm <sup>-3</sup> )	Total Acceptor Con. N <sub>A</sub> (cm <sup>-3</sup> )	μ <sub>H</sub> at 300K (cm <sup>2</sup> /V.s)	μ <sub>H</sub> at 80K (cm <sup>2</sup> /V.s)
OSL1	1.0 x 10 <sup>12</sup>	5.6 x 10 <sup>13</sup>	4.2 x 10 <sup>17</sup>	6.2 x 10 <sup>16</sup>	1180	3200
OSL2	8.0 x 10 <sup>12</sup>	3.1 x 10 <sup>13</sup>	1.2 x 10 <sup>17</sup>	3.3 x 10 <sup>16</sup>	1890	4500
OSL3	2.0 x 10 <sup>12</sup>	2.7 x 10 <sup>13</sup>	-	-	1960	-
OSL4	4.0 x 10 <sup>12</sup>	7.9 x 10 <sup>13</sup>	-	-	1270	-
OSL5	1.0 x 10 <sup>13</sup>	-	-	-	-	-
OSL6	6.0 x 10 <sup>12</sup>	3.8 x 10 <sup>13</sup>	-	-	1050	-

Table 5.7. Transport Data in Ion-Implanted and Annealed SI InP. The Samples Were Thermally Annealed With a 2000 Å Silox Encapsulating Layer at 750 to 800°C for 20 min. in Flowing Forming Gas.

Substrate Description	Implant Dose (cm <sup>-2</sup> )	$\mu_H$ at 300K (cm <sup>2</sup> /V.s)	Total Ionized Impurity $N_D+N_A$ (cm <sup>-3</sup> )
InP:Fe	$6.0 \times 10^{11}$	36	$7.5 \times 10^{16}$
	$1.4 \times 10^{12}$	17	$8.2 \times 10^{16}$
	$4.0 \times 10^{12}$	85	$7.2 \times 10^{16}$
	$6.0 \times 10^{12}$	1260	$1.1 \times 10^{18}$
	$8.0 \times 10^{12}$	75	$7.4 \times 10^{16}$
InP:Cr	$8.0 \times 10^{11}$	1387	$1.0 \times 10^{18}$
	$2.0 \times 10^{12}$	1155	$1.06 \times 10^{18}$

Table 5.8. Transport Data in Ion-Implanted and Annealed SI InP. The Samples Were Thermally Annealed at 670°C for 20 min. With a 3000 Å Silox Encapsulating Layer and a Piece of InP Placed on Top.

Substrate Description	Implant Dose (cm <sup>-2</sup> )	$\mu_H$ at 300K (cm <sup>2</sup> /V.s)	Total Ionized Impurity $N_D+N_A$ (cm <sup>-3</sup> )
InP:Fe	1.0 x 10 <sup>12</sup>	High resistivity	
	2.0 x 10 <sup>12</sup>		
	4.0 x 10 <sup>12</sup>	1700	1.8 x 10 <sup>17</sup>
	6.0 x 10 <sup>12</sup>	1300	1.06 x 10 <sup>18</sup>
	8.0 x 10 <sup>12</sup>	840	1.52 x 10 <sup>18</sup>
	10.0 x 10 <sup>12</sup>	130	8.5 x 10 <sup>16</sup>
	50.0 x 10 <sup>12</sup>	380	6.5 x 10 <sup>18</sup>
InP:Cr	4.0 x 10 <sup>12</sup>	1050	1.09 x 10 <sup>18</sup>
	6.0 x 10 <sup>12</sup>	940	1.27 x 10 <sup>18</sup>
	10.0 x 10 <sup>12</sup>	670	1.39 x 10 <sup>18</sup>

Similar behavior is observed in only one sample of SI InP:Fe implanted with a dose of  $6 \times 10^{12} \text{ cm}^{-2}$ . In addition, the surface carrier concentration in this sample is more than the implant dose. The rest of the implanted SI InP:Fe samples in the first batch exhibit p-type conductivity. On the other hand, only one sample in the second batch exhibits p-type conductivity. The variation of Hall mobility with temperature, in the implanted SI InP:Fe samples which exhibited n-type behavior, is shown in Fig. 5.12(a). The temperature dependence of Hall mobility in the implanted SI InP:Cr is depicted in Fig. 5.12(b). Anomalous behavior in the temperature dependence of the Hall mobility, as shown in Fig. 5.12, was observed at relatively low doses.

## 5.7 Analysis of Transport Data

### 5.7.1 Semi-Insulating InP

The solid lines in Fig. 5.6 are theoretical fits to the measured values of Hall mobility in SI InP. The final values of the concentrations and the compensation ratios are listed in Table 5.9. The values of  $E_F$  estimated from solutions of the charge neutrality equation are listed in Table 5.4. For some SI InP:Fe samples, where the measured value of  $(qR_H)^{-1}$  ( $\approx n$ ) is large, an activation energy of  $\sim 0.38 \text{ eV}$  is obtained from the slope of  $(qR_H)^{-1}$  versus  $1/T$  plot. It is clear that the relation (2-27) is approximately obeyed in such cases. The compensation mechanisms in different SI InP samples can also be visualized from a graphical solution of the charge neutrality equation, as depicted in Fig. 5.13. The value of the Fermi energy can be estimated from these diagrams.

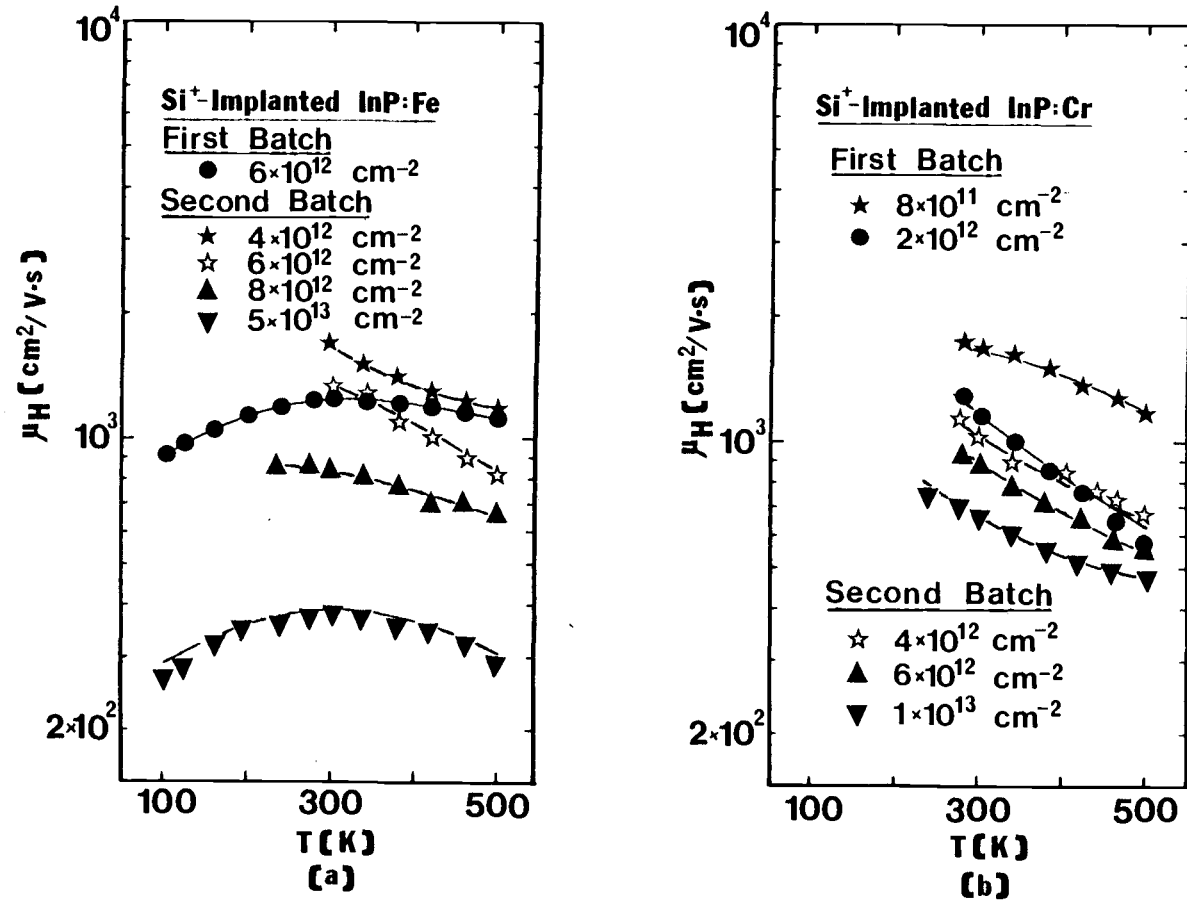


Figure 5.12. Variation of Hall mobility with temperature in Si-implanted and annealed SI InP: (a) implanted SI InP:Fe and (b) implanted SI InP:Cr. The implant doses and batches are mentioned in the diagrams.

Table 5.9. Shallow and Deep Acceptor Level Concentrations and Compensation Ratios in SI InP:Fe and InP:Cr Determined from Analysis of Hall-Effect Data.

Description	Sample	$N_{AA}$ ( $\text{cm}^{-3}$ )	$N_D$ ( $\text{cm}^{-3}$ )	$N_A$ ( $\text{cm}^{-3}$ )	$\frac{N_{AA}}{N_D - N_A}$
InP:Fe	V-OS-1	$8.5 \times 10^{15}$	$3.0 \times 10^{16}$	$2.5 \times 10^{16}$	1.7
	V-14	$5.2 \times 10^{15}$	$4.5 \times 10^{16}$	$4.0 \times 10^{16}$	1.04
	V-14-2	$5.7 \times 10^{15}$	$3.0 \times 10^{16}$	$2.5 \times 10^{16}$	1.14
	5380	$5.4 \times 10^{15}$	$3.5 \times 10^{16}$	$3.0 \times 10^{16}$	1.08
	5381	$1.001 \times 10^{16}$	$3.6 \times 10^{17}$	$3.5 \times 10^{17}$	1.001
	2545-3	$2.001 \times 10^{16}$	$1.7 \times 10^{17}$	$1.5 \times 10^{17}$	1.0005
InP:Cr	IPC-1	$3.6 \times 10^{15}$	$1.6 \times 10^{16}$	$1.5 \times 10^{16}$	3.6
	IPC-2	$4.5 \times 10^{14}$	$9.5 \times 10^{15}$	$9.2 \times 10^{15}$	1.5
	IPC-3	$5.0 \times 10^{14}$	$9.4 \times 10^{15}$	$9.1 \times 10^{15}$	1.67

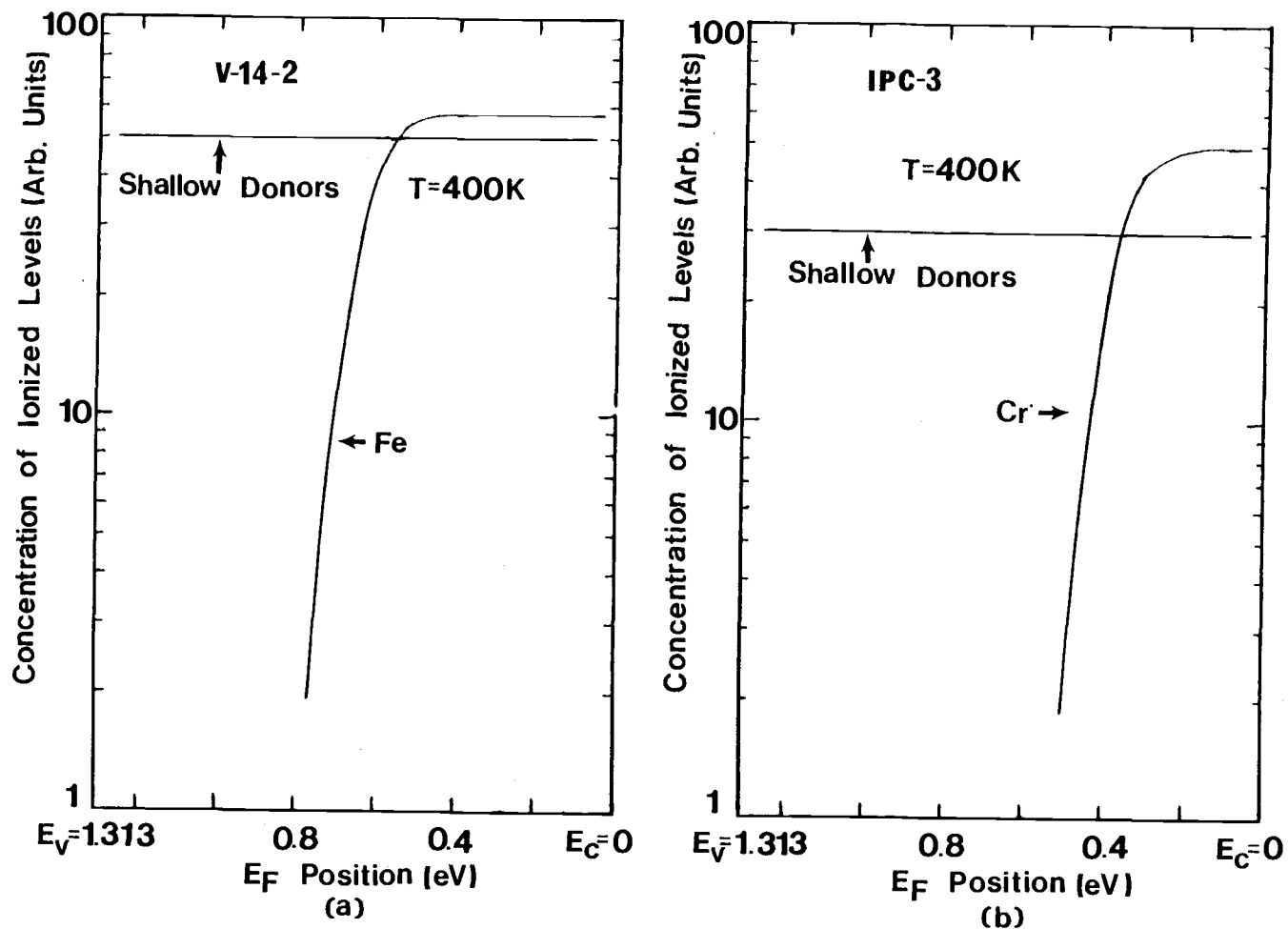


Figure 5.13. Calculated variation of the concentration of shallow and deep levels with the Fermi energy position in (a) SI InP:Fe and (b) SI InP:Cr. The intersections represent the values of the Fermi energy in the materials at 400K.

If  $n$  and  $p$  are considered negligible at high temperatures in a high-resistivity material, then the Fermi level can easily be estimated for a single compensating deep acceptor model;

$$E_F = E_{AA} + kT \ln g_{AA} - kT \ln \left( \frac{N_{AA}}{N_D - N_A} - 1 \right) \quad (5-1)$$

Using Eq. (5-1) and  $b = 20$  for SI InP, the normalized mobility  $\mu_H/\mu_{Hm}$  was calculated. The variation of this parameter with the compensation ratio is plotted in Fig. 5.14. The variation of the calculated value of  $p/n$  as a function of compensation ratio is shown in Fig. 5.15. From this trend in these diagrams a type conversion is expected for  $N_{AA}/(N_D - N_A) \approx 13.0$  in SI InP:Fe samples. On the other hand, no such prediction can be made for SI InP:Cr samples since the resistivity in these materials are much lower, and the assumptions made to derive Eq. (5-1) are not valid. By virtue of Eq. (2-14), the type conversion will occur when  $p/n = (\mu_n/\mu_p)^2 = 400$  in SI InP:Fe.

### 5.7.2 Ion-Implanted InP

The solid lines in Figs. 5.11 and 5.12, which depict the temperature dependence of mobility in ion-implanted InP, are the theoretical fits to the experimental results. The theoretical mobilities were calculated by taking into account the relevant scattering mechanisms. The decrease of mobility after implant and anneal, as shown in Fig. 5.11, is due to increased ionized impurity scattering. It should be noted that the high free-carrier concentrations in as-grown LPE samples are probably due to the contamination

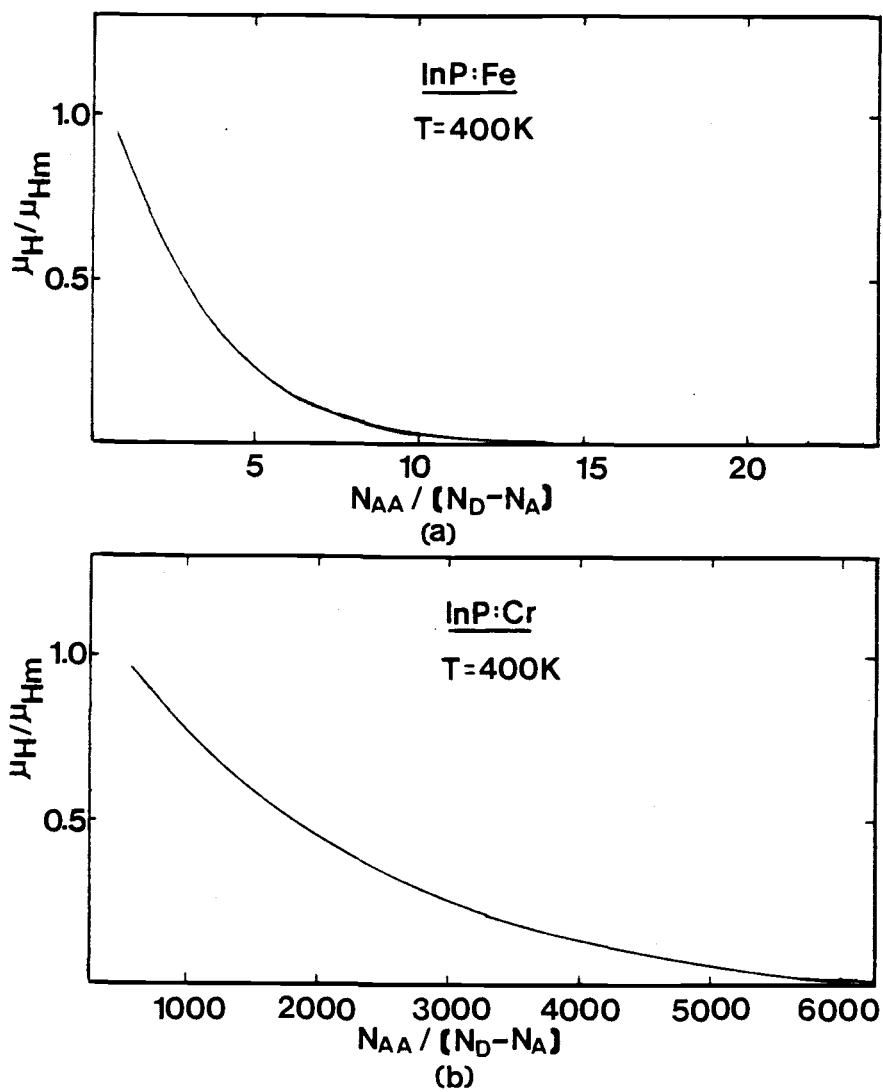


Figure 5.14. Calculated variations of the ratio  $\mu_H/\mu_{Hm}$  with compensation ratio in (a) SI InP:Fe and (b) SI InP:Cr.

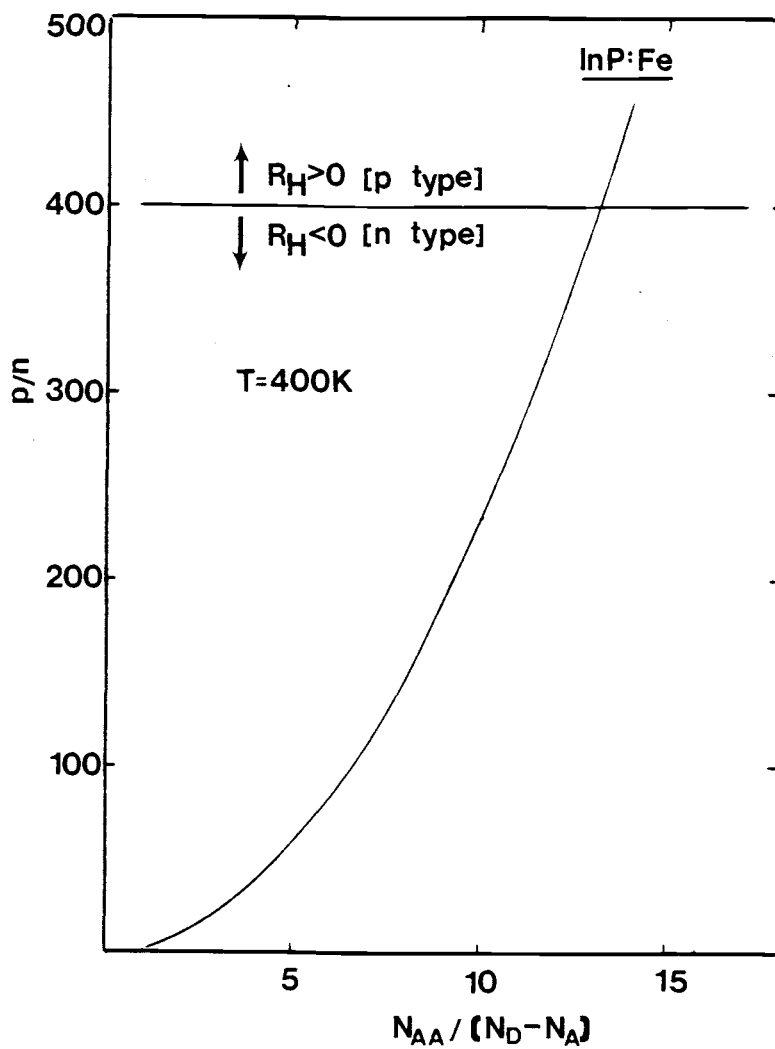


Figure 5.15. Calculated variation of the ratio  $p/n$  with compensation ratio in SI InP:Fe.

of Si and S in commercial In<sup>(47)</sup>. The observed over-activation of in some implanted samples may be explained as follows. Ion-implantation produce lattice damage which gives rise to donor-like centers. When their concentration, depending on the dose and energy of impinging ions, is more than the acceptor-like centers produced by thermal conversion<sup>(83)</sup> and outdiffusion of compensating acceptors from the substrate, n-type behavior results. The production of additional donors due to implantation can explain the over-activation. Similar effects have been observed by Donnelly and Hurwitz<sup>(16)</sup> after implanting SI InP:Fe with different doses of  $K_r^+$  at 400 KeV.

Two samples of SI InP:Fe exhibited high resistivity after being implanted with doses of  $(1-2) \times 10^{12} \text{ cm}^{-2} \text{ Si}^+$ . This is probably due to outdiffusion of Fe from the substrate into the implanted layer and compensation of the Si donors. All the implanted SI InP:Cr samples were n-type even after very low doses of  $\text{Si}^+$ .

### 5.8 Photocurrent Spectra in Semi-Insulating InP

A typical photocurrent spectra, in the spectral range 0.4-1.4 eV, recorded for SI InP:Fe at 100K and 203K are shown in Fig. 5.16(a). The spectrum at 100K shows a threshold of the photoresponse at  $\sim 0.68$  eV, has an onset near 1.08 eV which increases up to  $\sim 1.20$  eV, has a weaker onset at 1.20 eV, and finally a strong photoconductive onset at 1.38 eV due to band gap transitions. The spectrum at 223K shows similar features, except that the structure at 1.20 eV is absent. Typical recordings of the photocurrent spectra in SI InP:Cr are

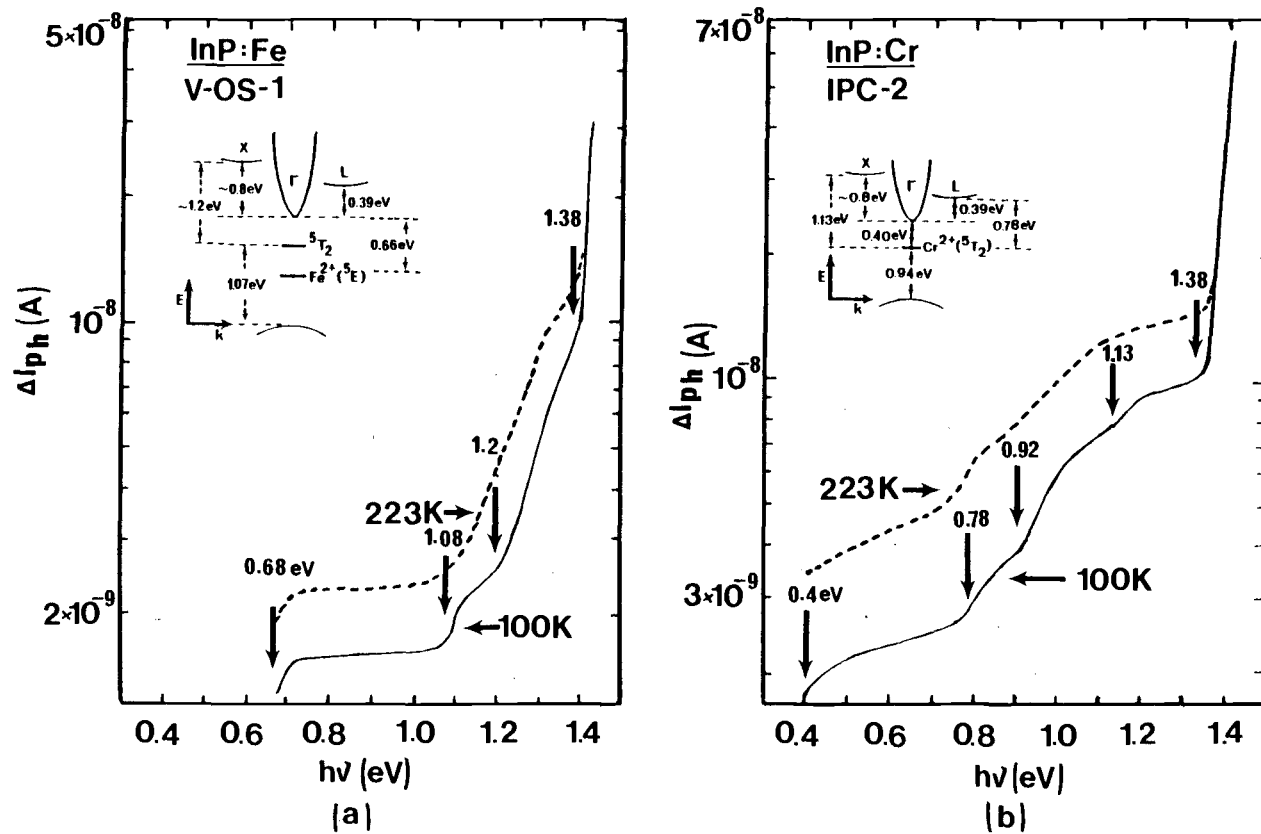


Figure 5.16. Photocurrent spectra obtained at  $T = 100$  and  $223\text{K}$  for (a) SI InP:Fe and (b) SI InP:Cr. The insets show the possible optical transitions.

shown in Fig. 5.16(b). The spectrum at 100K exhibits an onset of photoconductivity at  $\sim 0.4$  eV, has another onset at  $\sim 0.78$  eV followed by weak onsets at  $\sim 0.92$  and  $1.13$  eV, and a strong photoconductive onset at  $\sim 1.38$  eV. At 223K, weak onset at  $1.13$  eV is absent.

The known charge states of Fe in InP are  $\text{Fe}^{3+}$ ,  $\text{Fe}^{2+}$ , the one-electron trap state, and  $\text{Fe}^{1+}$ , the two-electron trap state. The latter two charge states are mostly contained in n-type crystals. With reference to Fig. 5.16(a), the onset at  $\sim 0.68$  eV, which corresponds to an ionization energy of  $0.66$  eV as depicted in Fig. 5.17(a), results from the excitation of electrons from the ground state of the  $\text{Fe}^{2+}$  state to the central conduction minimum<sup>(84)</sup>. The onset at  $\sim 1.08$  eV, corresponding to an ionization energy of  $1.07$  eV, results from the excitation of electrons from the valence band edge to the excited ( ${}^5T_2$ ) state of the  $\text{Fe}^{2+}$  state<sup>(84)</sup>. An additional onset at  $1.20$  eV (100K) observed in the photocurrent spectra can be attributed to several possible transitions. It may arise from an impurity or a defect level which is separated from either band edge by  $0.15$ - $0.20$  eV. Shallow trap levels in InP:Fe having activation energies in the above-mentioned range have been observed by Bonnafe et al.<sup>(85)</sup> who attributed their presence to background impurities. The onset in the photocurrent spectra can also be due to transitions from levels or one of the Fe charge states to higher lying portions of the conduction band structure. Transitions from either the  ${}^5E$  (ground state) or the  ${}^5T_2$  (excited state) level of the  $\text{Fe}^{2+}$  state to the L minima are unlikely in view of their energy separation of  $0.39$  eV from the  $\Gamma$  minimum, as determined by Wada et

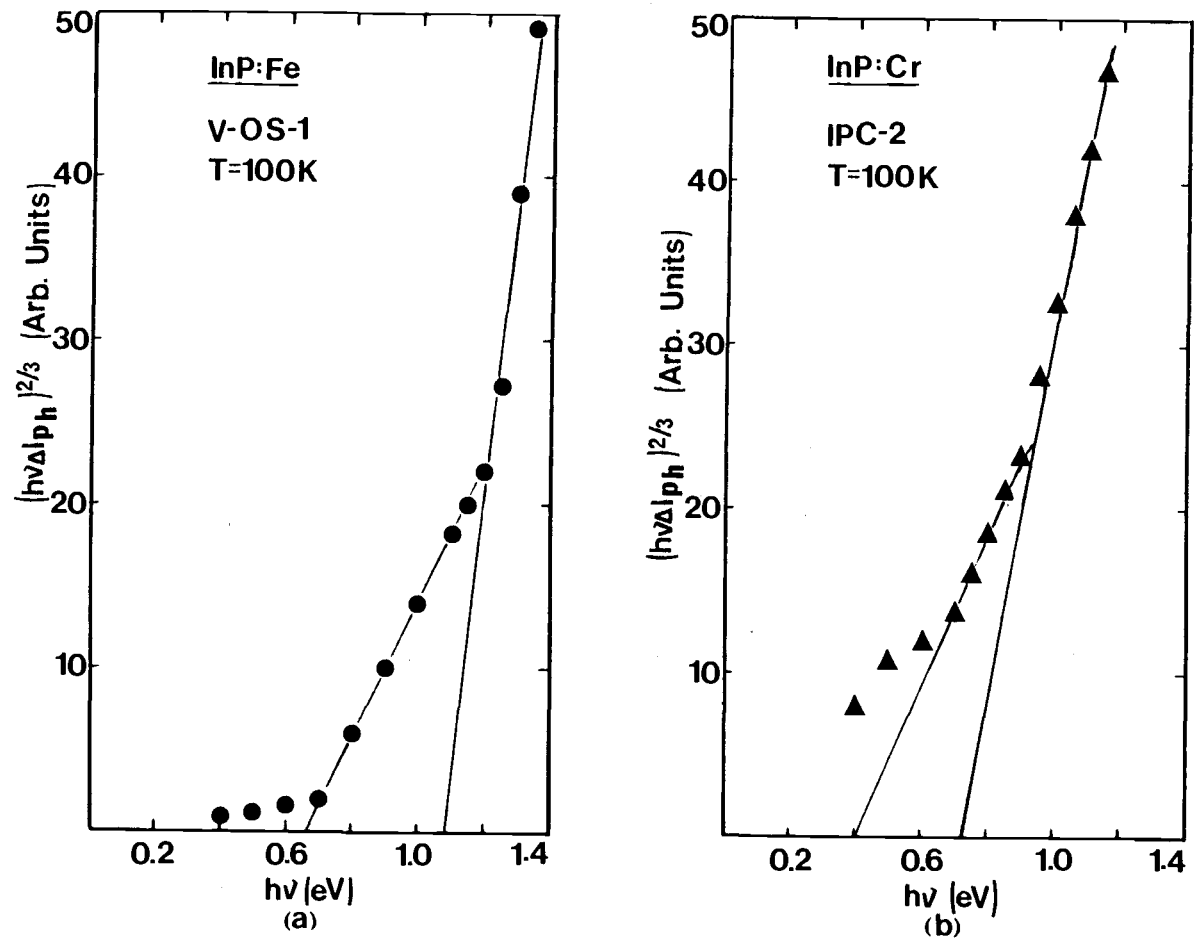


Figure 5.17. Plots of  $(h\nu\Delta I_{ph})^{2/3}$  versus photon energy for (a) SI InP:Fe and (b) SI InP:Cr. The intercepts on the energy axis give the optical transition energies.

al.<sup>(80)</sup>. But if the  $\Gamma$ -X separation of 0.8 eV<sup>(39)</sup> is assumed then transitions from the  $\text{Fe}^{2+}$  states to the X minimum can be conceived. The absence of these transitions at 223K is probably due to thermal quenching effects.

It is known that Cr in InP is present in the  $\text{Cr}^{3+}$ ,  $\text{Cr}^{2+}$  and  $\text{Cr}^{1+}$  states<sup>(86)</sup>. The initial onset of the photocurrent at 100K and the corresponding ionization energy of 0.4 eV is attributed to transitions from the Cr acceptor level ground state to the  $\Gamma$  conduction minimum<sup>(86)</sup>. The threshold at 0.92 eV is believed to be due to the complementary transition. In addition, onsets in the spectra at 100K were recorded at 0.78 and 1.13 eV. These may, again, be due to transitions between unknown trap levels and the band edges or between the Cr-level and higher lying portions of the conduction band. The former is less favorable as trap levels, other than the emission from the Cr-center, have not been detected from PICT measurements.

### 5.9 Photoconductivity Spectra in Ion-Implanted Semi-Insulating InP

Photoconductivity spectra for the implanted and annealed SI InP were recorded in the spectral range 0.4-1.4 eV at different temperatures below 300K. Typical photoconductivity spectra in the implanted SI InP:Fe and InP:Cr are shown in Figs. 5.18(a) and (b), respectively. The respective implant doses in the samples measured are mentioned in the figure. The general characteristics of the spectra are similar to those in SI InP described in the previous section. A noticeable feature is the presence of the onsets in photoconductivity which were attributed to transitions involving the Fe and Cr acceptor levels.

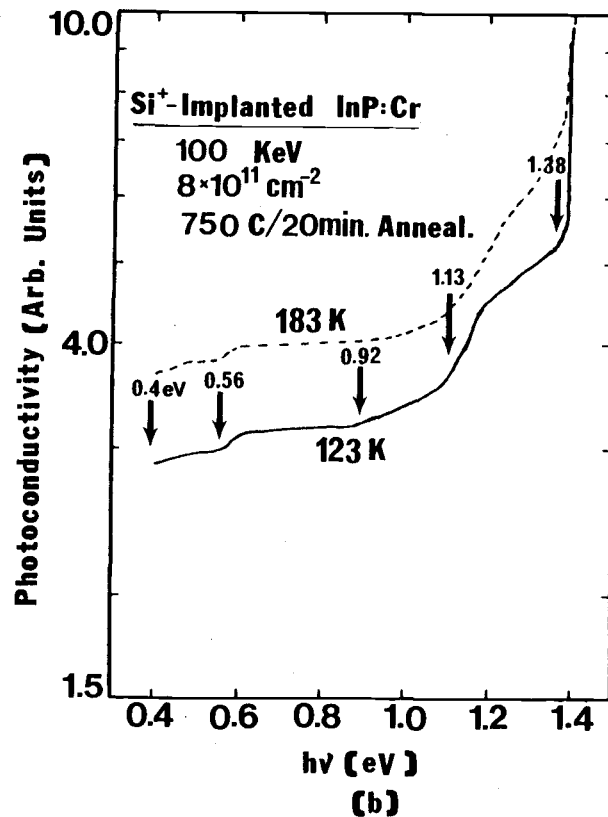
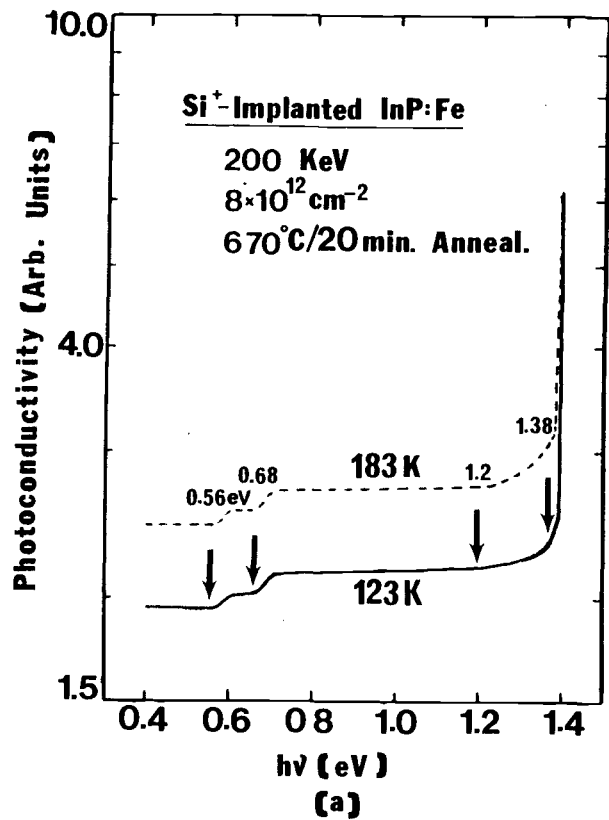


Figure 5.18. Photoconductivity spectra obtained for Si-implanted and annealed SI InP: (a) Si-implanted SI InP:Fe and (b) Si-implanted SI InP:Cr.

These also suggest that the anomalous behavior in the samples implanted with low doses of  $\text{Si}^+$  is probably due to outdiffusion of Fe and Cr atoms. The onset in photoconductivity observed at  $\sim 0.56$  eV, as shown in Figs. 5.18(a) and (b), has been recorded for all the implanted samples. The consistency of the transition indicates the creation of a center due to the implant damage or a complex involving  $\text{Si}^+$  and a native defect. The decrease in the relative intensity of the spectra for the implanted and annealed InP, compared with those for SI InP, is attributed to the increased carrier density.

#### 5.10 Discussion

There is remarkable consistency regarding the energy position of the compensating Cr and Fe levels in the forbidden energy gap of InP. Both Hall and photocurrent data indicate that the Cr level is located at  $\sim 0.40$  eV below the conduction band minimum. The emission activation energy  $\Delta E_{\text{T}} = 0.96 \pm 0.01$  eV, for the same center, confirms the above data and also indicates minimal coupling of the center with the lattice. Thus there is negligible barrier associated with the center and  $\Delta E_{\text{T}}$  reflects the energy position of the level above the valence band. Its capture cross section for holes is  $\sigma_{\infty} = (9.5 \pm 1.0) \times 10^{-13} \text{ cm}^2$ . The above facts are also true for the Fe-level in InP. From analysis of Hall-effect data and the photocurrent spectra, the energy position of the level is determined to be  $\sim 0.66$  eV below the conduction band minimum. This is confirmed by the PICT measurements, from which  $\Delta E_{\text{T}} = 0.69 \pm 0.01$  eV is obtained as the

activation energy for hole emission. This is again indicative of the fact that the Fe level is not coupled to the lattice. Electron emission from the Cr level has not been observed in any of the InP:Cr samples. This is due to the compensation in the samples and the energy position of the deep level relative to the Fermi level.

No other deep levels have been observed in InP:Cr by the PICT measurements. Thus the weak onsets at 0.78 and 1.13 eV observed in the photocurrent spectra are probably due to transitions involving the Cr level or other levels with low concentration levels. These onsets are not very distinctly observed in all samples. The energy positions of Cr and Fe centers in SI InP obtained in this study are consistent with the data obtained in recent investigations by other workers<sup>(5,39,84,86)</sup>.

An outcome of the present study is that no deep levels, other than the Fe- and Cr-related levels are present consistently with significant concentrations, and hence a single deep-acceptor compensation model can be assumed in semi-insulating InP:Cr and InP:Fe. Such a model has been successful in explaining the transport data and a set of consistent parameters have been obtained. It is seen that large fluctuations can occur in the slopes of  $(qR_H)^{-1}(T)$  and  $\sigma(T)$ , which are not due to the presence of other deep levels.

The results obtained from ion-implanted InP:Fe and InP:Cr samples suggest that both Fe and Cr diffuse into the active layer or to the interface during implantation and anneal. The observed p-type conductivity in Si-implanted InP:Fe has not been reported before. Though the van der Pauw devices were made from regions which

showed no apparent decomposition, it is likely that some P vacancies were created during thermal annealing. This, however, has not been confirmed. The defect level with a photoionization energy of 0.56 eV detected in the implanted InP:Fe and InP:Cr samples is probably created during the implant and annealing process.

## CHAPTER VI

CONCLUSIONS

The electrical and optical properties of device-quality, semi-insulating GaAs and InP and changes in these properties due to ion-implantation have been studied in detail. The high resistivity is brought about by compensating single deep acceptor-like levels in Cr- and Fe-doped semi-insulating materials, and by single deep donor-like levels, possibly related to O, in undoped semi-insulating GaAs. The thermal ionization properties of the Cr- and Fe-related levels have been determined from Photo-Induced Current Transient measurements, performed for the first time on semi-insulating InP.  $0.73 \pm 0.01$  and  $0.16 \pm 0.01$  eV hole trap levels detected in SI GaAs by the same measurement technique are ascribed to unknown impurities or defects. An electron trap level with an activation energy of  $0.98 \pm 0.01$  eV in undoped SI GaAs was detected for the first time in this study and is related to unknown impurities. An electron trap with  $\Delta E_T = 0.68 \pm 0.01$  eV observed in SI InP:Fe samples may be related to native defects. Additional deep electron and hole trap levels detected in SI GaAs and InP were not found to be present consistently.

Hall effect data obtained for the semi-insulating materials at high temperatures have been analyzed in detail taking into account the various relevant scattering mechanisms. Neutral impurity scattering is found to play an important role in limiting carrier mobilities at high temperatures. The various transport parameters

and the Fermi energies have been estimated from computer analyses on the basis of charge neutrality conditions.

Comparison of PICT, Hall effect and photocurrent data has enabled the accurate determination of the energy position of the Cr- and Fe-levels in SI materials. The Fe-level in SI InP:Fe is located at  $\sim 0.65$  eV below the conduction band edge. The Cr-levels in SI GaAs:Cr and InP:Cr are located at  $\sim 0.82$  and  $\sim 0.4$  eV, respectively, below the conduction band edge at room temperature. The consistency in the values of the ionization energy for the compensating centers obtained from the different measurements suggests that they have minimal lattice coupling. The deep donor level with an activation energy of 0.73 eV observed in undoped SI GaAs by Hall effect and photocurrent measurements was not detected by PICT measurements. This is probably due to optical quenching effects. From the photocurrent spectra in SI InP it is apparent that optical transitions from the deep acceptor levels to indirect conduction minima are possible.

Transient capacitance measurements on implanted and annealed GaAs show that electron and hole trap levels with activation energies of 0.53 and 0.15 eV, respectively, are consistently present. Both centers were also detected in the channel region of FETs fabricated by ion-implantation technology. A 0.17 eV was consistently detected in implanted and annealed LPE InP, whereas the 0.38 and 0.22 eV electron and hole trap levels, respectively, originally present in the as-grown samples were absent. Implantation and annealing creates an additional defect center in SI InP

with a photoionization energy of 0.56 eV. The greatly reduced electron mobility in the implanted layers, particularly at low temperatures, is attributed to increased ionized impurity scattering.

Some suggestions may be made for future work intended to extend the scope of the present study. Obtaining reproducible transport properties in ion-implanted GaAs and InP still remains a problem and more work is necessary to enable the fabrication of reliable devices. At the same time, the effects of ion implantation in alternate materials such as LPE or organometallic VPE compounds needs to be investigated in detail. A more systematic study is necessary to determine the physico-chemical origin of various traps detected in this study, and to develop processes to eliminate them. Finally, the use of materials with high carrier mobilities, such as  $\text{In}_{1-x}\text{Ga}_x\text{As}$ , for the fabrication of high-speed devices using ion-implantation technology needs to be explored.

REFERENCES

1. M. Castange, J. Bonnafe, J.C. Manificier and J.P. Fillard, J. Appl. Phys., 51, 4894 (1980).
2. P.F. Lindquist, J. Appl. Phys., 48, 1262 (1977).
3. See, for example, the relevant publications in Semi-Insulating III-V Materials, ed. by Rees (Shiva Publications Limited, UK, 1980).
4. G.M. Martin, J.P. Farges, G. Jacob, J.P. Hallais and G. Poibland, J. Appl. Phys., 51, 2840 (1980).
5. G.W. Iseler, Proceedings of the Seventh International Symposium on Gallium Arsenide and Related Compounds, St. Louis, ed. by C.M. Wolfe, (The Institute of Physics, London, 1979), p. 144.
6. J.K. Rhee and P.K. Bhattacharya, J. Appl. Phys., 53 (to be published, June 1982).
7. S.R. McAfee, F. Capasso, D.V. Lang, A. Hutchinson and W.A. Bonner, J. Appl. Phys., 52, 6158 (1981).
8. Ch. Hurtes, M. Boulou, A. Mitonneau and D. Bois, Appl. Phys. Lett., 32, 821 (1978).
9. J. van der Pauw, Philips Res. Rep., 13, 1 (1958).
10. S. Asai, S. Ishioka, H. Kurono, S. Takahashi and H. Koderu, J. Jap. Soc. Appl. Phys. Suppl., 42, 71 (1973).
11. I. Crossley, I.H. Goodridge, M.J. Cardwell and R.S. Butlin, Proceedings of the Sixth International Symposium on Gallium Arsenide and Related Compounds, St. Louis, ed. by L.F. Eastman (The Institute of Physics, London, 1977), p. 289.

12. J.A. Higgins, F. Eisen, B. Welch, G. Robinson and W. Hill, in Ref. 11, p. 236.
13. H. Kanber, M. Feng, D.B. Ruby and G.E. Stillman, Presented at the 23rd Electronic Materials Conference, Santa Barbara, 1981.
14. K.L. Wang and G.P. Li, ibid.
15. J.K. Rhee, P.K. Bhattacharya and R.Y. Koyama, J. Appl. Phys., 53, (to be published, April 1982).
16. J.P. Donnelly and C.E. Hurwitz, Appl. Phys. Lett., 31, 419 (1977).
17. D.E. Davis, J.P. Lorenzo and T.G. Ryan, Solid-State Electron., 21, 981 (1978).
18. T. Nishioka and Y. Ohmachi, J. Appl. Phys., 51, 5789 (1980).
19. N.D. Wilsey, J. Comas and R.N. Shelby, Proceedings of International Conference on Defects and Radiation Effects in Semiconductors, 1978, Nice, ed. by J.H. Albany, (The Institute of Physics, London, 1979), p. 487.
20. T.R. Jervis, D.W. Woodard and L.F. Eastman, Electron. Lett., 15, 619 (1979).
21. P.K. Bhattacharya, J.K. Rhee, S.J.T. Owen, J.G. Yu, K.K. Smith and R.Y. Koyama, J. Appl. Phys., 52, 7224 (1981).
22. M.G. Astles, F.G.H. Smith and E.W. Williams, J. Electrochem. Soc., 120, 1750 (1973).
23. E. Kuphal, J. Crystal Growth, 54, 117 (1981).
24. J.S. Blakmore, Semiconductor Statistics, Pergamon Press, New York (1962).
25. R.N. Hall, Phys. Rev., 83, 228 (1951).
26. W. Shockley and W.T. Read, Phys. Rev., 87, 835 (1952).

27. D.V. Lang and R.A. Logan, *J. Electron. Mater.*, 4, 1053 (1975).
28. Y. Furukawa and Y. Ishibashi, *Japan. J. Appl. Phys.*, 5, 837 (1966).
29. D.V. Lang, *J. Appl. Phys.*, 45, 3023 (1974).
30. A. Mitonneau, G.M. Martin and A. Mircea, Proceedings of the Sixth International Symposium on Gallium Arsenide and Related Compounds, Edinburgh, 1976, ed. by C. Hilsum (The Institute of Physics, London, 1977), p. 73.
31. P.K. Bhattacharya, Ph.D. Thesis, University of Sheffield, UK, 1978.
32. M. Bleicher and E. Lange, *Solid-State Electron.*, 16, 375 (1973).
33. G.M. Martin and D. Bois, Proceedings of the Topical Conference on Characterization Techniques for Semiconductor Materials and Devices, Spring Meeting of the Electrochem. Soc., 78-3, 32 (1978).
34. R.H. Bube, Photoconductivity of Solids, John Wiley and Sons, Inc., New York (1960).
35. D.L. Rode, *Phys. Rev. B*, 2, 1012 (1970).
36. N. Sclar, *Phys. Rev.*, 104, 1559 (1956).
37. C.D. Thurmond, *J. Electrochem. Soc.*, 122, 1133 (1975).
38. Y.P. Varshni, *Physica*, 39, 149 (1967).
39. S. Fung, R.J. Nicholas and R.A. Stradling, *J. Phys. C: Solid State Phys.*, 12, 5145 (1979).
40. K. Hess, N. Stath and K.W. Benz, *J. Electrochem. Soc.*, 121, 1208 (1974).
41. V. Wrick, G.J. Scilla, L.F. Eastman, R.L. Henry and E.M. Swiggard, *Electron. Lett.*, 12, 394 (1976).

42. G.H. Olsen and M. Ettenberg, *J. Appl. Phys.*, 45, 5112 (1974).
43. T. Nishinaga, K. Pak and S. Uchiyama, *J. Crystal Growth*, 42, 315 (1977).
44. S. Guha, A. Majerfeld, N. Moyes and P.N. Robson, *Electron. Lett.*, 11, 303 (1975).
45. K. Pak, T. Nishinaga and S. Uchiyama, *Japan. J. Appl. Phys.*, 16, 949 (1977).
46. W.Y. Lum and A.R. Clawson, *J. Appl. Phys.*, 50, 5296 (1979).
47. D.E. Holmes and G.S. Kamath, *J. Crystal Growth*, 54, 51 (1981).
48. V.L. Wrick, III and L.F. Eastman, in Proceedings of the Fifth International Symposium on Gallium Arsenide and Related Compounds, Deauville, 1974, (The Institute of Physics, London, 1975), p. 31.
49. G.G. Bauman, K.W. Benz and M.H. Pilkuln, *J. Electrochem. Soc.*, 123, 1232 (1976).
50. M.E. Weiner, *J. Electrochem. Soc.*, 119, 496 (1972).
51. S.H. Groves and M.C. Planko, Proceedings of Conference on Gallium Arsenide and Related Compounds, St. Louis, 1978, ed. by C.M. Wolfe, (The Institute of Physics, London, 1979), p. 71.
52. M. Simons and E.E. King, *IEEE Trans. Nuclear Science*, NS-26, 5080 (1979).
53. P.K. Bhattacharya, J.W. Ku, S.J.T. Owen, V. Aebi, C.B. Cooper, III and R.L. Moon, *Appl. Phys. Lett.*, 36, 304 (1980).
54. H. Brooks, Advances in Electronics and Electron Physics, ed. by L. Marton (Academic, New York, 1955), p. 156.
55. A. Fortini, D. Diguët and J. Lugand, *J. Appl. Phys.*, 41, 3121 (1970).

56. J. Bardeen and W. Shockley, *Phys. Rev.*, 80, 72 (1950).
57. D. Zook, *Phys. Rev.*, 136, A869 (1964).
58. L.R. Weisberg, *J. Appl. Phys.*, 33, 1817 (1962).
59. E.M. Conwell and M.O. Vassal, *Phys. Rev.*, 166, 797 (1968).
60. R.H. Bube and H.E. MacDonald, *Phys. Rev.*, 128, 2062 (1962).
61. G.B. Stringfellow and H. Künzel, *J. Appl. Phys.*, 51, 3254 (1981).
62. J.S. Blakemore, in Ref. 3, p. 29.
63. P.K. Vasudev and R.H. Bube, *Solid-State Electron.*, 21, 1095 (1978).
64. A.L. Lin and R.H. Bube, *J. Appl. Phys.*, 47, 1859 (1976).
65. K. Kitahara, K. Nakai, A. Shibatomi and S. Ohkawa, *Appl. Phys. Lett.*, 32, 259 (1978).
66. G.K. Ippolitova, E.M. Omel'yanovskii and L. Ya. Pervova, *Sov. Phys. Semicond.*, 9, 864 (1976).
67. A.L. Lin, E. Omelianovski and R.H. Bube, *J. Appl. Phys.*, 47, 1852 (1976).
68. Y. Tokumaru, *Japan. J. Appl. Phys.*, 9, 95 (1970).
69. E.W. Williams, *Brit. J. Appl. Phys.*, 18, 253 (1967).
70. E. Farbe, *C.R. Acad. Sc.*, (France), B270, 848 (1970).
71. G.M. Martin, in Ref. 3, p. 13.
72. R.D. Fairman and J.R. Oliver, in Ref. 3, p. 83.
73. G.M. Martin, A. Mitonneau and A. Mircea, *Electron. Lett.*, 13, 192 (1977).
74. A. Mitonneau, G.M. Martin and A. Mircea, *Electron. Lett.*, 13, 667 (1977).

75. F. Hasegawa and A. Majerfeld, *Electron. Lett.*, 12, 52 (1976).
76. V. Kaufmann and J. Schneider, *Appl. Phys. Lett.*, 36, 747 (1980).
77. P.M. Asbeck, J. Tandon, B.M. Welch, C.A. Evans and V.R. Deline, *Electron. Dev. Lett.*, EDL-1, 35 (1980).
78. O. Wada and A. Majerfeld, *Electron. Lett.*, 14, 125 (1978).
79. A.M. White, A.J. Grant and B. Day, *Electron. Lett.*, 14, 409 (1978).
80. O. Wada, A. Majerfeld and A.N.M.M. Choudhury, *J. Appl. Phys.*, 51, 423 (1980).
81. D.V. Lang and C.H. Henry, *Phys. Rev. Lett.*, 35, 1525 (1975).
82. H. Nickel and E. Kuphal, *Phys. Stat. Sol. (a)*, 65, 583 (1981).
83. P.B. Klein, P.E.R. Nordquist and P.G. Siebenmann, *J. Appl. Phys.*, 51, 4861 (1980).
84. S.G. Bishop, P.B. Klein, R.L. Henry and B.D. McCombe, in Ref. 3, p. 161.
85. J. Bonnafe, M. Castange, J. Romestan, M. DeMurcia and J.P. Fillard, *Electron. Lett.*, 16, 314 (1980).
86. S. Fung and R.J. Nicholas, in Ref. 3, p. 154.

APPENDICES

## APPENDIX I

The mathematical forms describing the temperature dependence of electron mobility limited by different scattering mechanisms in semiconductors are outlined below.

I.1 Polar Optical Phonon Scattering

The temperature dependence of the electron mobility due to polar optical phonon scattering following the analysis of Fortini et al. (55) is expressed by

$$\mu_{PO} = 25.48 \frac{T^{1/2}}{\theta (m^*/m_o)^{3/2}} \frac{\exp(\frac{\theta}{T}) - 1}{(1/\epsilon_\infty - 1/\epsilon_s)} G(\frac{\theta}{T}) \quad (\text{cm}^2/\text{V.s}) \quad (\text{I-1})$$

where  $\theta = h \omega_1/k$  is the optical phonon temperature, and  $G(\theta/T)$  is a function determined by Fortini et al. (55)

I.2 Ionized Impurity Scattering

The temperature dependence of mobility, in accordance with the Brooks-Herring formulation (54) is given by:

$$\mu_I = \frac{3.28 \times 10^{15} \epsilon_s^2 T^{3/2} (m_o/m^*)^{1/2}}{(N_A + N_D) \{ \ln(b+1) - b/(b+1) \}} \quad (\text{cm}^2/\text{V.s}) \quad (\text{I-2})$$

$$\text{where } b = 1.29 \times 10^{14} \left( \frac{\epsilon_s}{n^*} \right) \left( \frac{m^*}{m_o} \right) T^2 \quad (\text{I-3})$$

$$\text{and } n^* = n_o + \frac{(n_o + N_A)(N_D - N_A - n_o)}{N_D} \quad (\text{cm}^{-3}) \quad (\text{I-4})$$

$n^* = n_o \approx N_D - N_A$  when the donors and acceptors are fully ionized.

### I.3 Piezoelectric Scattering

The electron mobility limited by piezoelectric scattering is given by<sup>(57)</sup>

$$\mu_{PE} = \frac{2.51 \times 10^8 T^{-1/2}}{h_{14}^2 (4/C_t + 3/C_l) (m^*/m_o)^{3/2}} \text{ (cm}^2\text{/V.s)} \quad (\text{I-5})$$

where  $h_{14} = e_{14}/\epsilon_s \epsilon_o$  is the piezoelectric constant in V/cm and

$$C_l = \frac{1}{5} (3C_{11} + 2C_{12} + 4C_{44}) \quad (\text{I-6})$$

$$C_t = \frac{1}{5} (C_{11} - C_{12} + 3C_{44}) \quad (\text{I-7})$$

are the spherically averaged longitudinal and transverse elastic constants.

### I.4 Deformation Potential Scattering

Bardeen and Shockley<sup>(56)</sup> have derived the mobility limited by this mechanism. The temperature dependence can be expressed as:

$$\mu_{DP} = \frac{3.17 \times 10^{-5} C_l T^{-3/2}}{E_1^2 (m^*/m_o)^{5/2}} \text{ (cm}^2\text{/V.s)} \quad (\text{I-8})$$

where  $C_l = \rho_d u_l^2$ .  $E_1$  is the deformation potential in eV and  $\rho_d$ ,  $u_l$  the material density and sound speed, respectively.

### I.5 Space Charge Scattering

From the formulation by Weisberg<sup>(58)</sup> the mobility limited by space charge scattering can be expressed as

$$\mu_{sc} = \frac{3.2 \times 10^9 T^{-1/2}}{(m^*/m_0)^{1/2} (N_s \cdot A_s)} \text{ (cm}^2\text{/V.s)} \quad (\text{I-9})$$

where  $N_s$  and  $A_s$  are, respectively, the density and area of the scattering center.

## APPENDIX II

MATERIAL PARAMETERS USED FOR ANALYSIS OF TRANSPORT DATA

Parameter	Symbol	GaAs	InP
Electron Effective Mass Ratio	$m_e^*/m_o$	0.068	0.078
Hole Effective Mass Ratio	$m_h^*/m_o$	0.5	0.72
Optical Phonon Temperature	$\theta$ (K)	420	501
Piezoelectric Constant	$e_{14}$ (C/m <sup>2</sup> )	0.16	0.035
Low-Frequency Dielectric Constant	$\epsilon_s$	12.9	12.30
High-Frequency Dielectric Constant	$\epsilon_\infty$	10.92	9.56
Density	$\rho_d$ (g/cm <sup>3</sup> )	5.36	4.83
Sound Speed	$u_1$ (km/sec)	5.24	5.16
Acoustic Deformation Potential	$E_1$ (eV)	8.6	9.0-18.0
Elastic Constant	$C_{11}$ (dyne/cm <sup>2</sup> )	$1.188 \times 10^{12}$	$1.022 \times 10^{12}$
Elastic Constant	$C_{12}$ (dyne/cm <sup>2</sup> )	$0.538 \times 10^{12}$	$0.576 \times 10^{12}$
Elastic Constant	$C_{44}$ (dyne/cm <sup>2</sup> )	$0.594 \times 10^{12}$	$0.46 \times 10^{12}$

## APPENDIX III

COMPUTER PROGRAMS FOR ANALYSIS OF TRANSPORT DATA

Solution of Charge Neutrality Equation by Newton's Iterative Method

```

PROGRAM CHANEA (INPUT,OUTPUT,TAPE5=INPUT,TAPE6=OUTPUT)
10 READ(5,30) GND1,GND2,GND3,GNA,DED1,DED2,DED3,DEF
30 FORMAT(4(E8.2,1X),4F6.4)
   WRITE(6,31)GND1,GND2,GND3,GNA,DED1,DED2,DED3
31 FORMAT(/1X,*GND1=*,E9.3/1X,*GND2=*,E9.3/
11X,*GND3=*,E9.3/1X,*GNA=*,E9.3/1X,*DED1=*,F6.4/
11X,*DED2=*,F6.4,/1X,*DED3=*,F6.4)
   WRITE(6,32)
32 FORMAT(/5X,*T*,8X,*GNT*,9X,*DEF*,9X,*EF*)
   Z=GND1+GND2+GND3-GNA
   T=80.
   DO 100 I=1,26
   T=T+20.
   X=8.625E-5*T
   Y=8.36E+13*T**1.5
20 ODEF=DEF
   E=-DEF/X
   F=(-DED1+DEF)/X
   G=(-DED2+DEF)/X
   H=(-DED3+DEF)/X
   A=Y*EXP(E)
   B=GND1/(1.+0.5*EXP(F))
   C=GND2/(1.+0.5*EXP(G))
   D=GND3/(1.+0.5*EXP(H))
   P=A+B+C+D-Z
   AN=-(Y/X)*EXP(E)
   BN=-0.5*GND1*EXP(F)/(X*(1.+0.5*EXP(F))**2)
   CN=-0.5*GND2*EXP(G)/(X*(1.+0.5*EXP(G))**2)
   DN=-0.5*GND3*EXP(H)/(X*(1.+0.5*EXP(H))**2)
   P1=AN+BN+CN+DN
   DEF=DEF-P/P1
   IF(ABS(DEF-ODEF).GT.0.00001) GO TO 20
   EG=1.522-5.8E-4*T**2/(T+300.)
   EF=EG-DEF
100 WRITE(6,33) T,A,DEF,EF
33 FORMAT(2X,F4.0,4X,E9.3,2(6X,F6.4))
   GO TO 10
END

```

Mobility Analysis for Conducting Materials

```

PROGRAM GAASMO(INPUT,OUTPUT,TAPE5=INPUT,TAPE6=OUTPUT)
DIMENSION U(26,9),DT(15),G(15)
DATA DT/0.6,0.7,0.8,0.9,1.0,1.1,1.2,1.4,1.5,2.0,2.5,
1      3.0,3.5,4.0,4.5/
DATA G/0.7008,0.6861,0.6776,0.6748,0.6770,
1      0.6837,0.6943,0.7258,0.7458,0.8752,
2      1.0321,1.1908,1.3484,1.4926,1.6173/
10 READ (5,20) GNA,GND,GNSA,DP,EIO
20 FORMAT(3E10.3,2F5.3)
WRITE(6,21) GNA,GND,GNSA,DP,EIO
21 FORMAT(/1X,*NA=*,E9.3/1X,*ND=*,E9.3/1X,*NS=*,E9.3/
11X,*E1=*,F6.3/1X,*EIO=*,F6.3)
WRITE(6,22)
22 FORMAT(/1X,*T*,6X,*UPD*,6X,*UI1*,8X,*UI2*,6X,*UDP*,9X,*UPE*,
16X,*USC*,6X,*UH1*,6X,*UH2*,6X,*UH3*)
T=80.
DO 100 I=1,26
T=T+20.
TK=416./T
DO 200 K=1,14
200 IF(TK.LT.DT(K+1)) GO TO 30
30 GI=G(K)+(TK-DT(K))*(G(K+1)-G(K))/(DT(K+1)-DT(K))
U(I,1)=240.*T**0.5*(EXP(TK)-1.0)*GI
B=1.12E+14*T**2/(GND-GNA)
DN=(GNA+GND)*(ALOG(B+1.)-B/(B+1.))
U(I,2)=2.096E+18*T**1.5/DN
XK=(8.625E-5*T)**0.5
U(I,3)=3.4E+20*(1.875*XK+EIO/XK)/GNA
U(I,3)=1./U(I,2)+1./U(I,3)
U(I,3)=1./U(I,3)
U(I,4)=3.86E+10*T**(-1.5)/DP**2
U(I,5)=6.97E+6*T**(-0.5)
U(I,6)=1.23E+10*T**(-0.5)/GNSA
U(I,7)=1./U(I,1)+1./U(I,2)+1./U(I,4)+1./U(I,5)+1./U(I,6)
U(I,7)=1./U(I,7)
U(I,8)=1./U(I,1)+1./U(I,3)+1./U(I,4)+1./U(I,5)+1./U(I,6)
U(I,8)=1./U(I,8)
U(I,9)=1./U(I,1)+1./U(I,3)+1./U(I,4)+1./U(I,5)
U(I,9)=1./U(I,9)
100 WRITE(6,23) T,(U(I,J),J=1,9)
23 FORMAT(F4.0,6E10.3,2X,3F9.2)
GO TO 10
END

```

Mobility Analysis for Semi-Insulating Materials

```

PROGRAM GAASSE(INPUT,OUTPUT,TAPE5=INPUT,TAPE6=OUTPUT)
DIMENSION U(26,6),DT(15),G(15)
DATA DT/0.6,0.7,0.8,0.9,1.0,1.1,1.2,1.4,1.5,2.0,2.5,
1      3.0,3.5,4.0,4.5/
DATA G/0.7008,0.6861,0.6776,0.6748,0.6770,
1      0.6837,0.6943,0.7258,0.7458,0.8752,
2      1.0321,1.1908,1.3484,1.4926,1.6173/
10  READ(5,20) GNA,GND,GNI,DP,EM
20  FORMAT(3E13.6,2F6.4)
    WRITE(6,21) GNA,GND,GNI,DP,EM
21  FORMAT(1X,*NA=*,E13.6/1X,*ND=*,E13.6/1X,*NI=*,E13.6/
11X,*E1=*,F5.2/1X,*EM=*,F6.4)
    WRITE(6,22)
22  FORMAT(/1X,*T*,6X,*UPO*,6X,*UI*,8X,*UDP*,6X,*UPE*,
19X,*UNI*,6X,*UH*)
    T=80.
    DO 100 I=1,26
    T=T+20.
    TK=416./T
    DO 200 K=1,14
200  IF(TK.LT.DT(K+1)) GO TO 30
30   GI=G(K)+(TK-DT(K))*(G(K+1)-G(K))/(DT(K+1)-DT(K))
    U(I,1)=4.26*T**0.5*(EXP(TK)-1.)*GI/EM**1.5
    B=1.65E+15*EM*T**2./ABS(GND-GNA)
    DN=(GNA+GND)*(ALOG(B+1.)-B/(B+1.))
    U(I,2)=5.47E+17*T**1.5/(EM**0.5*DN)
    U(I,3)=4.66E+7*T**(-1.5)/(DP**2.*EM**2.5)
    U(I,4)=1.24E+5*T**(-0.5)/EM**1.5
    DEL=12.91*(T/EM)**0.5
    U(I,5)=9.06E+20*EM*(7.34E-3*DEL+30.2/DEL)/GNI
    U(I,6)=1./U(I,1)+1./U(I,2)+1./U(I,3)+1./U(I,4)+1./U(I,5)
    U(I,6)=1./U(I,6)
100  WRITE(6,23)T,(U(I,J),J=1,6)
23  FORMAT(F4.0,5E9.3,F8.2)
    GO TO 10
END

```

Hall Coefficient, Hall Concentration and Conductivity Data Analysis

```

PROGRAM CHANE2(INPUT,OUTPUT,TAPE5=INPUT,TAPE6=OUTPUT)
10 READ(5,20)GNA1,GND1,GNI,DP,EM,DEF,N
20 FORMAT(3E13.6,3F6.4,I1)
   READ(5,21)GNDD,GNA,GNA,GND,EAA,EDD,BR
21 FORMAT(4E13.6,3F5.2)
   WRITE(6,30)GNA,GNA1,GND,GND1,GNA,GND,GNDD,EAA,EDD,BR,
   GNI,DP,EM
30 FORMAT(/1X,*NA=*,E13.6,5X,*NA1=*,E13.6/
1     1X,*ND=*,E13.6,5X,*ND1=*,E13.6/
2     1X,*NAA=*,E13.6,4X,*NDD=*,E13.6/
3     1X,*EAA=*,F7.4,10X,*EDD=*,F7.4/
4     1X,*BR=*,F7.4,11X,*NI=*,E13.6/
5     1X,*DP=*,F7.4,11X,*EM=*,F7.4)
   WRITE(6,31)
31 FORMAT(/1X,*TT*,8X,*EF*,9X,*DEF*,9X,*NH*,9X,*NT*,9X,*PH*)
   WRITE(6,32)
32 FORMAT(/1X,*TT*,8X,*SIG*,9X,*RO*,9X,*RH*,9X,*RHT*)
   Z=GND-GNA
   EPS=10.**(-12)
   T=280.
   DO 100 I=1,16
   T=T+20.
   X=8.625E-5*T
   Y=8.54E+13*T**1.5
   V=1.7E+15*T**1.5
   EG=1.519-5.4E-4*T**2/(T+204.)
40 ODEF=DEF
   E=-DEF/X
   F=(EG-DEF)/X
   G=(-EAA+DEF)/X
   H=(EDD-DEF)/X
   A=Y*EXP(E)
   B=GNA/(1.+2.*EXP(G))
   C=V*EXP(-F)
   D=GNDD/(1.+2.*EXP(H))
   P=A+B-C-D-Z
   AN=-Y*EXP(E)/X
   BN=-2.*GNA*EXP(G)/(X*(1.+2.*EXP(G))**2)
   CN=V*EXP(-F)/X
   DN=GNDD*2.*EXP(H)/(X*(1.+2.*EXP(H))**2)
   P1=AN+BN-CN-DN
   DEF=DEF-P/P1
   IF(ABS(DEF-ODEF).GT.EPS) GO TO 40
   EF=EG-DEF
   IF(N.EQ.1) GO TO 45
   AT=-EAA/X
   CR=GNA/(GND-GNA)
   GNT=2.*Y*EXP(AT)/(CR-1.)
   UN=UH(T,GNA1,GND1,GNI,DP,EM)
   BT=(EAA-EG)/X

```

```

SIG=8.E-20*UN*V*(CR-1.)*(EXP(BT)+4.*Y*BR*EXP(AT)/
1((CR-1.)**2*V))/BR
RO=1./SIG
CT=(2.*EG-3.*EAA)/X
DT=(EG-2.*EAA)/X
RH=1.25E+19*(EXP(-BT)-4.*BR**2.*Y*EXP(CT)/(V*(CR-1.)**2))
1/(V*(CR-1.)*(1.+4.*BR*Y*EXP(DT)/(V*(CR-1.)**2))**2)
GO TO 46
45 AT=EDD/X
BT=(EG-EDD)/X
CT=(2.*EG-3.*EDD)/X
DT=(EG-2.*EDD)/X
CR=GNDD/(GNA-GND)
GNT=0.5*(CR-1.)*Y*EXP(-AT)
UN=UH(T,GNA1,GND1,GNI,DP,EM)
SIG=8.E-20*UN*(CR-1.)*Y*(EXP(-AT)+4.*V*
1EXP(-BT)/(BR*(CR-1.)**2*Y))
RO=1./SIG
RH=3.13E+18*(CR-1.)*(EXP(BT)-0.25*BR**2*(CR-1.)**2
1*Y*EXP(CT)/V)/((1.+0.25*BR*(CR-1.)**2*Y*EXP(DT)/V)**2*V)
46 RHT=RH*T**1.5
TT=1000./T
WRITE(6,33)TT,EF,DEF,A,GNT,C
33 FORMAT(1X,F5.2,2(1X,F6.4),3(1X,E13.6))
100 WRITE(6,34)TT,SIG,RO,RH,RHT
34 FORMAT(1X,F5.2,4(5X,E9.3))
GO TO 10
END
FUNCTION UH(T,GNA1,GND1,GNI,DP,EM)
DIMENSION U(6),DT(15),G(15)
DATA DT/0.6,0.7,0.8,0.9,1.0,1.1,1.2,1.4,1.5,2.0,2.5,
1 3.0,3.5,4.0,4.5/
DATA G/0.7008,0.6861,0.6776,0.6748,0.6770,
1 0.6837,0.6943,0.7258,0.7458,0.8752,
2 1.0321,1.1908,1.3484,1.4926,1.6173/
TK=416./T
DO 200 K=1,14
200 IF(TK.LT.DT(K+1)) GO TO 70
70 GI=G(K)+(TK-DT(K))*(G(K+1)-G(K))/(DT(K+1)-DT(K))
U(1)=4.26*T**0.5*(EXP(TK)-1.)*GI/EM**1.5
B=1.65E+15*EM*T**2/ABS(GND1-GNA1)
DN=(GNA1+GND1)*(ALOG(B+1.)-B/(B+1.))
U(2)=5.47E+17*T**1.5/(EM**0.5*DN)
U(3)=4.66E+7*T**(-1.5)/(DP**2*EM**2.5)
U(4)=1.24E+5*T**(-0.5)/EM**1.5
DEL=12.91*(T/EM)**0.5
U(5)=9.06E+20*EM*(7.34E-3*DEL+30.2/DEL)/GNI
U(6)=1./U(1)+1./U(2)+1./U(3)+1./U(4)+1./U(5)
U(6)=1./U(6)
UH=U(6)
RETURN
END

```